Tunable Narrow-band X-band Bandpass Filters

by

Elmine Meyer

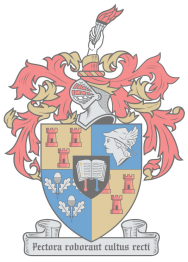

Dissertation submitted in fulfilment of the requirements for the Doctorate of Philosophy degree from the Department of Electrical and Electronic Engineering at the University of Stellenbosch

Supervisor: Prof. P. Meyer

March 2018

Acknowledgements

For very special contributions to the creation process of this dissertation, the following acknowledgements are made:

- Prof. Petrie Meyer for his continued guidance and support, for sharing his knowledgeable and encouraging words throughout these 5 years.
- My Parents and brother for their continuous love, support and encouragement.
- My husband, Bernard Meyer, for his love, patience, support, companionship and for dealing with all those down-in-the-dirt-moments no one else got to see.
- All the fellow students and colleagues in, and around the various offices I have been in these past 5 years, who provided support, wisdom and good company throughout the project.
- The SKA for funding the project and providing me with many opportunities to gain knowledge and experience in the field of microwave filters.
- Grintek Evasion (GEW) Technologies for financial and technical assistance.
- Wessel Croukamp and Wynand van Eeden for the manufacturing of both filter prototypes and great conversation.
- Anneke Bester for her help with the measurements and overall support.
- Hi-Q Electronics and Skyworks Inc. for the varactor samples used in this dissertation.
- Luna and Stella for their love, happiness and companionship.

Declaration

"I, the undersigned, hereby declare that the work contained in this report is my own original work unless indicated otherwise. I also declare that I have not previously submitted the work contained in this dissertation in its entirety or in part at any university for a degree."

Signature: E. Meyer

Date: March 2018

Abstract

This dissertation proposes two narrow-band tunable X-band filters from different classes, one planar and one waveguide. The first is a suspended substrate varactor-tuned doubly end-loaded staircase filter that incorporates a geometrically decoupled biasing structure. The second design consists of a varactor-tuned evanescent mode waveguide filter that incorporates tuning screws and a symmetrical varactor mounting structure inside the guide. The filters are designed for miniaturization with competitive filter performance in terms of centre frequency tunability, insertion loss and bandwidth performance.

A planar staircase filter with electrically decoupled biasing and centre frequency tunability is realised using a suspended substrate and surface mount varactor diodes. Each half-wave resonator is terminated at both ends with identical varactor diodes, controlled by a single biasing line running through the roof of the enclosure. For symmetrically loaded half-wave resonators such as used in the staircase filter, each resonant line is DC decoupled from the next and a zero-voltage point exists in the centre of each line. This point is stationary under changes in centre frequency, which is a significant advantage for tunable filters. The biasing structure is also non-resonant, which allows for good out-of-band performance. The proposed planar structure is illustrated by a fifth order staircase X-band filter. Using varactors at each open end of the resonators together with spatially decoupled bias feeds, a measured centre frequency tunability of 400 MHz is achieved around a nominal frequency of 11.9 GHz.

The tunable evanescent mode waveguide filter is realised with in-waveguide mounted varactors and tuning screws. The mechanical tuning screws enable rough-tuning, while the varactors provide fine-tuning capabilities. The varactors are connected back-to-back on central metal plates which are grounded to the enclosure. The other end of each varactor is connected to a biasing wire which exits the enclosure through a small hole in the side of the waveguide. A centre frequency tunability of 1.3 GHz around a nominal frequency of 10.45 GHz is achieved by the manufactured filter prototype.

Both filters are evaluated through theory and simulation in terms of the thermal resistance of the mounting structure and input power limitations due to the non-linearity and power dissipation of the varactor diodes. Across the full tuning range of the planar filter, the maximum input power limit is 8 dBm. For the waveguide filter, the simulation yielded a maximum input power limit for full range tunability of 2 dBm due to the non-linearity of the hyperabrupt varactor diode, the applied voltage, and the power dissipation in the varactors.

The proposed biasing structure is a novel method for biasing planar filters, and to the knowledge of the author, this is the first application of the specified in-waveguide mounted diode structure in tunable evanescent mode waveguide filters.

Uittreksel

Twee nouband verstelbare X-band filters vanaf verskillende klasse, een planêr en een golfleier, word aangebied in hierdie proefskrif. Die eerste filter is 'n gesuspendeerde substraat varaktor-verstelde dubbelsydig-belaaide trapfilter wat 'n geometries-ontkoppelde voorspanningsnetwerk insluit. Die tweede ontwerp behels 'n varaktor-verstelde onder afknip golfleier filter wat verstelbare skroewe en simmetriese varaktor monteringstrukture behels.

'n Planêre trapfilter met elektries-ontkoppelde voorspanning is gerealiseer met die gebruik van gesuspendeerde substraat en oppervlakgemonteerde varaktor diodes. Elke half-golflengte resoneerder word aan beide kante getermineer met identiese varaktor diodes wat beheer word deur 'n vertikale voorspanningslyn. 'n Punt van nul RF spanning bestaan op simmetries belaaide half-golflengte resoneerders, soos in die geval van 'n trapfilter waar elke resoneerder ook GS ontkoppel is. Hierdie punt is stasionêr met verandering in senter frekwensie, wat 'n groot voordeel vir verstelbare filters bied. Die voorspanningstruktuur is nie resonant nie, wat bydra tot goeie buiteband werkverrigting. Die voorgestelde filter word geïllustreer deur 'n vyfde orde X-band trapfilter. 'n Verstelbare senter frekwensie van 400 MHz is gemeet rondom 'n nominale frekwensie van 11.9 GHz.

Die verstelbare onder afknip golfleier filter is gerealiseer deur van geïntegreerde varaktormonteringstrukture en verstelbare skroewe gebruik te maak. Die meganiese verstelbare skroewe stel die verbruiker in staat om growwe verstelling te doen, terwyl die varaktors fyn-verstelling moontlik maak. Die varaktors word rug-aan-rug konnekteer op 'n sentrale metaalplaat wat gegrond is teen die behuising. Die ander kant van elke varaktor is gekonnekteer aan 'n voorspanningsdraad wat deur 'n klein gaping in die behuising gevoer word. 'n Verstelbare senter frekwensie van 1.3 GHz rondom 'n nominale frekwensie van 10.5 GHz is gemeet.

Beide filters is geëvalueer met teorie en simulasies in terme van die termiese weerstand van die monteringstrukture en die intreedrywingsbeperkings as gevolg van die nie-lineariteit en drywingsverkwisting van die varaktors. Oor die volle bereik van die frekwensie verstelling is die maksimum intreedrywingsbeperking vir die planêre filter 8 dBm terwyl dit 2 dBm vir die golfleier filter is. Die laer beperking van die golfleier filter is as gevolg van die nie-lineariteit van die varaktor tipe, die voorspanningsvlakke, en die drywingverkwissing in die varaktors.

Die voorgestelde voorspanningsstruktuur is 'n nuwe metode vir die voorspanning van planêre filters, en so ver die kennis van die skrywer strek, is hierdie die eerste toepassing van die golfleier monteerde diode struktuur vir onder afknip golfleier filters.

Contents

List of Figures

List of Tables

Chapter 1

Introduction

To make provision for the increasing demands on spectrum usage, increased traffic, and differences in spectrum allocations between geographical areas, future microwave systems will require frequency and bandwidth agility. At the core of this capability lies the need for miniaturised, frequency agile, or tunable, microwave filters. At microwave frequencies, tunability of the filter centre frequency is typically achieved by changing the lengths of the resonators using electronic switches, or by adding a variable capacitive or inductive load to the resonator [1].

The concept of tunable filters originated with mechanically-tuned filters for RADAR in the 1930s [2]. Though these filters offer a very low-loss tuning solution, they are bulky and require mechanical access which is not always practical. Another solution for frequency tuning in those days was to use more than one filter interchangeably.

Up to the 1960s, frequency reconfigurability in systems was mostly achieved through the use of conventionally switched filter banks. These filter banks used switches to alter the arrangements of fixed filters. Though this solved the mechanical access problem, these designs did not address the size issue and often enlarged the system in comparison to that of the mechanically-tuned filters. Though filter banks are still being used today, electrically-tuned filters can now be used instead of fixed filters to realise wide ranges of centre frequencies [3].

Since the early 1960s, frequency reconfigurability and size reduction in tunable filters have been achieved through the use of magnetically and electrically tunable materials. One of the first materials to be used for this purpose was Yittrium-Iron-Garnet (YIG) [4] which has magnetically controllable properties. A current bias creating a magnetic field may therefore be used to tune a YIG component [2]. Though YIG components are still used in some applications their power consumption, tuning speeds and size are not suited for mobile communication systems with strict power consumption requirements.

Therefore, interests have shifted to electrically reconfigurable or tunable filters which offer low-cost, minimised solutions with lower power consumption than that of the conventionally switched filter banks [5], and enable the miniaturization of structures. These filters have the ability to alter certain filter characteristics such as centre frequency, bandwidth and/or roll-off using control signals. As a result, the use of varactors in tunable systems have become increasingly popular due to their small size, low-cost, availability and fast tuning speeds. One of the first varactor-tuned bandpass filters was presented in 1982 and achieved a centre frequency tunability from 3.2 to 4.9 GHz [6].

With the improvement of micro-machining processes and materials in the late 1980s, a new wave of interest arose for miniaturised tunable filters. In 1992, the first implementation of micro-electro-mechanical-systems (MEMS) in a filter was published by Lin *et al.*

[7]. The series resonator filter had a centre frequency of 18.7 kHz and a 1.2 kHz bandwidth. However, it was not until the late 1990s that the MEMS systems were implemented for tuning filters at microwave frequencies [8].

The implementation of frequency agile filters often occur in multiband telecommunication systems, radiometers, and RADAR [9]. It is envisioned that the improvements in size and power capabilities of reconfigurable front-end systems will lead to increased usage in current applications, such as CubeSat and high power transmitters. Although there are many applications for CubeSat systems, all the designs have need for robust, low-cost, and miniaturised structures due to the cost of launch. A single CubeSat typically consists of a 1000 cm^3 volume and weighs no more than 1 kg [10]. For high power transmitters, used in for example some RADAR applications, it is critical to prevent the radiation of the out-of-band spurious signals. A tunable high power narrow band filter can offer frequency agility while still suppressing the spurious signals. Therefore, the future of CubeSat and high power transmitters drives the need for miniaturised high performance narrow band filters in terms of loss, power handling capabilities, and tunability of frequency and bandwidth.

1.1 Requirements, Aims and Objectives

The main focus of this dissertation is to present the full design cycle of two tunable filters with completely different structures, one planar and one waveguide, designed from the same basic principles. No specific application is intended with these designs, rather an investigation into the usability of each implementation. The study is limited to systems with a continuous tuning capability. Each design aims to achieve an X-band tunable narrow-band Chebychev bandpass response with good out-of-band attenuation, centre frequency tunability, a miniaturised structure and good power handling capabilities.

Two very different technologies were chosen to investigate the implementation of varactors as tuning elements in both planar and waveguide structures. Planar topologies offer small size and simple structural implementation at the cost of increased loss, while waveguide topologies potentially offer reduced loss, improved heat dissipation, and post-production tuning. For the purpose of miniaturisation, evanescent mode waveguide is used.

Amongst the many papers which present tunable topologies, few give more than a cursory overview of the biasing circuits required by the tunable circuit elements, yet the biasing of tuning elements are critical to the final filter performance, and often introduces significant additional complexity in the design and especially manufacturing of these filters. In terms of performance, biasing circuitry can also change the stop-band performance even if the influence on the passband is small. Biasing circuits based on resonant decoupling for instance, manifest as either capacitive or inductive parasitic elements at stop-band frequencies, changing the performance of the filter at these frequencies. In the case of tunable filters, requirements on the biasing are even more stringent, as decoupling needs to be achieved over the whole tuning range.

Since the size and weight of systems are becoming increasingly important, it is envisioned to design miniaturised structures without compromising the performance of the filter. Many published solutions implement tunable filters in microstrip structures; however, interests in waveguide filters remain due to the high-Q factor and power capabilities of the structures [11]. Microstrip and stripline structures have the highest loss, but are also the smallest and least expensive [12]. Waveguide structures on the other hand, have the low-

est loss, but are much larger in size and more costly than microstrip/stripline, substrate-integrated-waveguide and dielectric resonator structures. Evanescent mode waveguide filters have the advantage of a reduction in size as well as inherent narrow band performance.

1.2 Proposed Contribution

This dissertation presents two new filter structures for the implementation of tunable filters at X-band:

- a varactor-tuned suspended substrate filter with spatially decoupled vertical biasing pins [13], and
- a waveguide-mounted varactor-tuned evanescent mode waveguide filter

The first design is a suspended substrate filter which incorporates a staircase topology with varactors on both edges of each resonator, as in Fig. 1.1. It is common for tunable microstrip and stripline filters to have biasing lines which are etched on the PCB; however, it is proposed here to use vertical biasing pins that run through the roof of the enclosure straight down onto the centre of each resonant line.

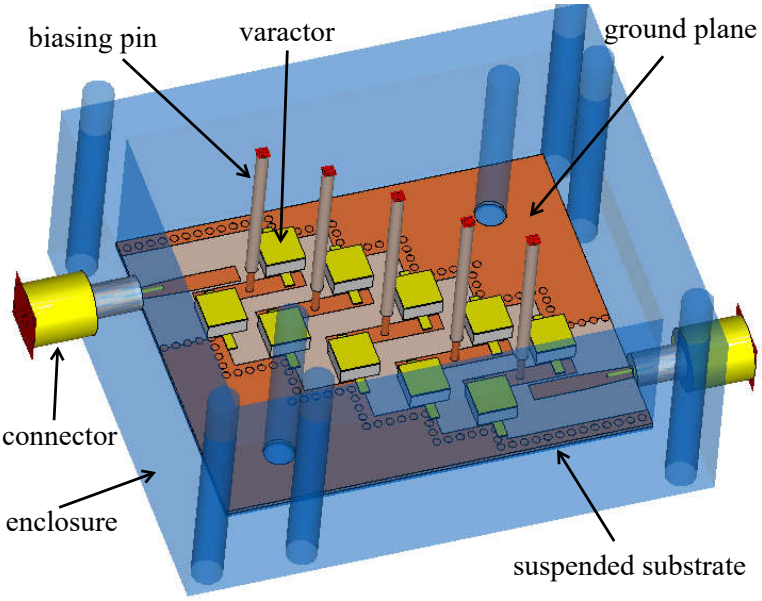

Fig. 1.1: *Tunable Suspended Substrate Planar Staircase Filter*

The discussion in Sec. 4.2 shows that there are a number of advantages when biasing the varactors in this manner. The pins are placed at the centre of each line, which is a point of zero electric field. In addition, no coupling occurs to the magnetic field on the line.

The staircase filter topology has DC decoupled resonators which is advantageous for the placement of biasing circuitry. The symmetry and open ends of each resonator allow for the addition of two identical varactors, controllable by a single vertical biasing pin.

The biasing pins extend through the roof of the enclosure and thus has a length greater than that of the air gap above the substrate. The inductive properties allow the pins to function as RF chokes, preventing any RF from leaking out into the DC biasing

and control circuit. Also, the staircase topology inherently prevents any DC power from reaching the RF ports.

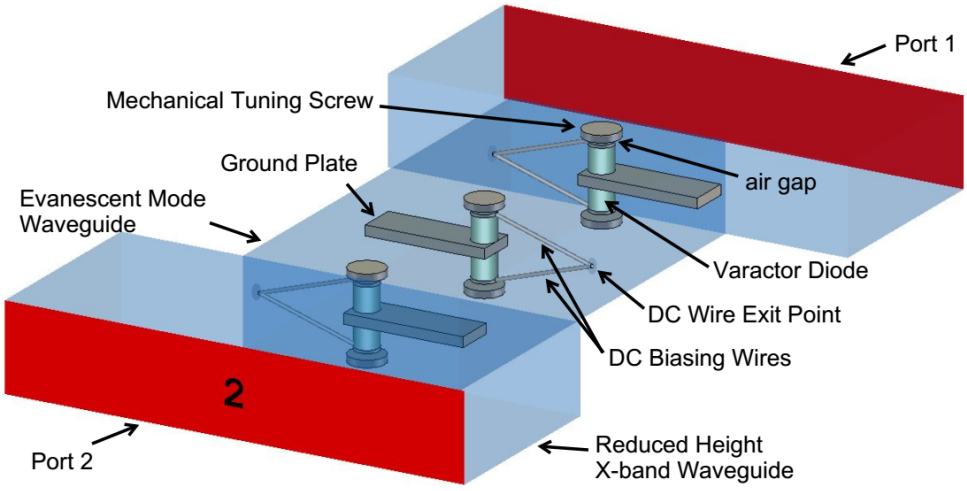

Fig. 1.2: *Tunable Evanescent Mode Waveguide Filter*

The second contribution is a varactor-tuned evanescent mode waveguide filter, shown in Fig. 1.2. Building on the work for a high power evanescent mode waveguide switch presented by Sickel [14], a novel varactor-tuned filter is proposed. The loaded evanescent mode waveguide functions as a filter when the varactor is reverse biased and placed strategically between evanescent mode sections.

Referring to Fig. 1.2, each mounting structure consists of a central ground plane in the form of a metal strip placed horizontally at the vertical centre of the waveguide. The varactor diodes are substituted for the PIN diodes in [14], and are vertically positioned and attached to the central plate by means of soldering. DC biasing lines are attached to the open ends of the varactors in the form of very thin wires which run through a single point in the side wall of the waveguide.

Both tunable filter designs presented in this dissertation have the following objectives:

- Narrow bandwidth of $5 - 10\%$
- Centre frequency tunability at X-band frequencies
- Chebychev filter response for good attenuation
- Minimised biasing structures
- Minimised overall structures
- Use cost-effective, readily available tuning components

1.3 Dissertation Layout

This dissertation commences with a literature study in Chapter 2 which includes a discussion on components commonly-used for tunability and how they have been implemented in recent planar and waveguide filter designs. An overview on the basic concepts of tunable coupled-line filters is presented in Chapter 3, introducing the reader to theoretical concepts required for the dissertation. The first original contribution and its entire design process is presented in Chapter 4. Also in this chapter is a study on the tunability of commonly-used coupled line filter topologies. The second original contribution is presented in Chapter 5, which discusses the design, simulation, manufacturing and measurement of a third order varactor-tuned narrow-band evanescent mode waveguide filter. Chapter 6 presents the power handling capabilities and non-linearity of each filter due to its tuning components. Chapter 7 concludes the dissertation. In Appendix A, a detailed review of the TRL calibration theory used in this dissertation is presented.

Chapter 2

Tuning Components and Tunable Filters

Tunable filters are fast emerging as extremely important components in new-generation microwave devices, and a number of viable topologies using different tuning elements have been proposed over the last decade. PIN diodes, varactor diodes, piezoelectric actuators and Micro–Electro–Mechanical Systems (MEMS) have all been implemented in tunable filter designs [15]. This chapter provides background information on some tuning components commonly-used in tunable filter designs and their implementation in tunable planar and waveguide filters.

2.1 Tuning Components

One of the largest advantages electrically-tuned filters have over mechanically-tuned filters, is that the filter can be incorporated into an enclosed system given that there is no need for mechanical changes to achieve tunability. Amongst others, PIN diodes, varactor diodes, silicon dice, piezoelectric actuators and Micro–Electro–Mechanical Systems (MEMS) can all be used for designing electrically tunable filters due to their varying electrical properties.

Through the use of tuning components, the resonant and/or coupling properties of a transmission line may be altered. For the purpose of this dissertation, only centre frequency tuning is of interest. This is mostly achieved by changing the effective length of resonators which alters the resonant frequency. The effective length is dependent on the physical length of the line, as well as the capacitive or inductive elements of the additional component(s). Therefore, centre frequency tuning may be achieved either by switching line sections in and out of the circuit, or by using a non-binary component with variable properties. Tunable capacitive elements such as tunable capacitors, varactors and MEMS capacitors are often used to achieve continuous tuning, while PIN diodes, MEMS switches and piezoelectric actuators are often used for discrete tuning.

The advantages and disadvantages of each variable reactance element should be taken into consideration when choosing a tuning component for filter design. There exists some common deciding factors which dictate this choice, including the following [15]:

- Insertion loss and return loss
- Bandwidth and selectivity
- RF power handling

- Power consumption
- Linearity
- Tuning Speed
- Control mechanism and circuitry
- Fabrication
- Sensitivity to shock, temperature, and vibration
- Cost and availability

For the purpose of this dissertation the focus is on fabrication, control mechanism and circuitry (include the biasing structure), cost and availability, and power handling capabilities.

PIN Diodes

PIN diodes are useful when considering high power-handling and fast switching times. They function well as tunable resistors and switches when forward biased at high frequencies. Many RF applications implement forward biased PIN diodes, including limiters and high power switches. In the reverse biased state at frequencies below the dielectric relaxation frequency of the intrinsic region (often less than 20 MHz), PIN diodes can be used as tunable capacitors [14]. Unfortunately this property does not hold for RF and microwave frequencies, where a reverse biased PIN diode behaves like a parallel plate capacitor with a separation inversely proportional to the thickness of the intrinsic region.

The forward bias model is shown in Fig. 2.1a, while the reverse bias model for the PIN diode is shown in Fig. 2.1b. Here C_p is the package capacitance, L_{PIN} is the package series inductance, R_p is the dissipative resistance, R_s is the diode forward bias series resistance, and C_j is the diode junction capacitance.

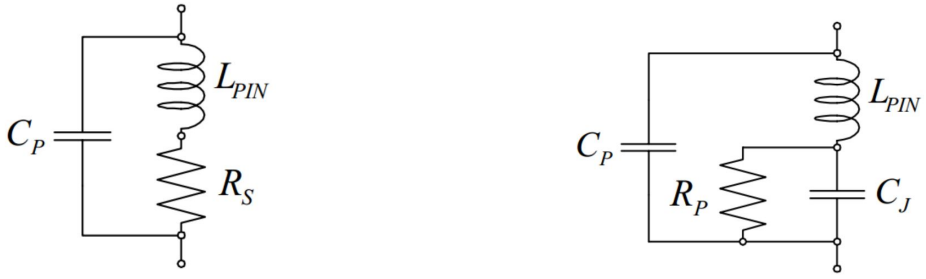

(a) Forward Bias Model *(b)* Reverse Bias Model

Fig. 2.1: *PIN Diode Equivalent Models [14]*

The intrinsic region in PIN diodes consists of undoped silicon which creates a largely resistive section in the diode. Due to this undoped intrinsic region, a high-level injection of charge carriers is required to create current flow. A diode with a larger intrinsic region, is better suited to high power applications due to having a higher breakdown voltage. Contrarily, a thinner intrinsic region results in faster switching speeds.

Varactor Diodes

Varactor diodes are advantageous when considering fast tuning speeds, large tuning ranges with continuous tuning capability, cost, power consumption, availability, and miniaturization, but they are also known for their high losses at higher frequencies.

Varactors, also known as variable reactors or variable capacitors, are a form of p-n diode. A varactor has a positive terminal consisting of a p-type material (donor) and a negative terminal consisting of an n-type material (acceptor). Initial contact between the two doped materials results in a depletion region. The width of the depletion region can be varied by the application of a reverse biasing voltage.

The depletion region creates a capacitance which is inversely proportional to the thickness of the depletion region, and therefore to the applied biasing voltage, as shown in Fig. 2.2a. The series resistance of a varactor also has an inversely proportional relationship to the reverse biasing voltage, though the amount of variation depends on the component, as can be seen in Fig. 2.2b. Given that the resistance and capacitance increase or decrease together, though at different rates, the effect on the filter performance can be quite significant.

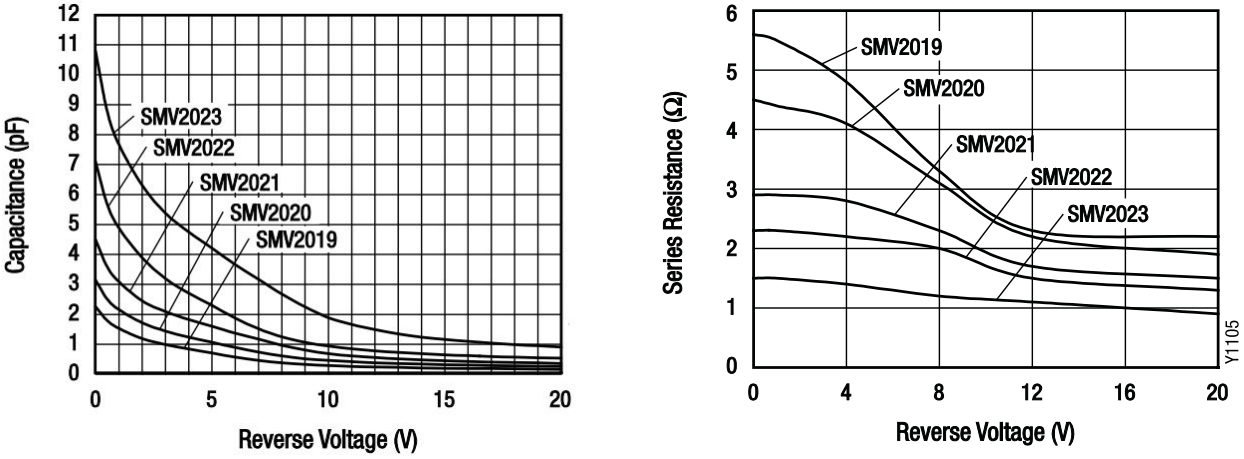

(a) Capacitance vs Voltage

(b) Series Resistance vs Voltage

Fig. 2.2: *Isolink SMV2019 to 2023 Series Varactor Properties [16]*

There are two main types of varactor diodes: abrupt and hyperabrupt. The plots in Fig. 2.2 displays the behaviour for a hyperabrupt varactor. The classification refers to the density of the donor atoms in the depletion region of the diode. Figure 2.3 shows the doping levels for each region of hyperabrupt and abrupt varactors. The density has direct relevance to the capacitance and tunability, since the width of the depletion region depends on the density of donor atoms on each side of the junction.

Figure 2.4 shows that abrupt varactors ($n = 1/2$) have a smaller capacitance range in comparison to hyperabrupt varactors ($n = 1$ and 2), where n is the grading coefficient (sometimes assigned the letter m) from the varactor capacitance equation:

$$C_V = \frac{C_0}{(1 + \frac{V_R}{V_0})^n} \tag{2.1.1}$$

Therefore, abrupt varactors are more suited to sensitive structures where very fine tuning is required. Varactors for X-band applications require reverse bias voltages of up

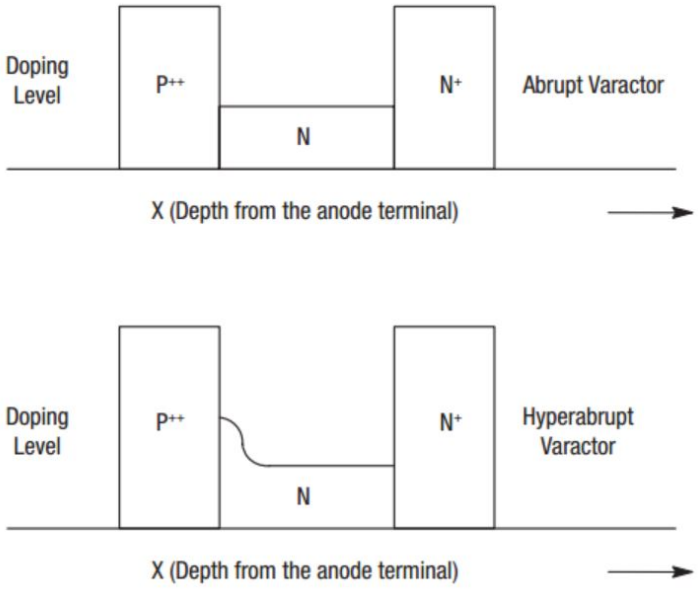

Fig. 2.3: *Doping levels in Hyperabrupt and Abrupt Varactors [17]*

to and sometimes, but rarely, beyond 30 Volts. Varactors typically have a maximum power dissipation rating of around 250 mW and can therefore not handle high power quantities when suspended in air. Some of the largest challenges when designing varactor-tuned filters include correct modelling and implementation of biasing lines. Both of these challenges will be addressed in this dissertation.

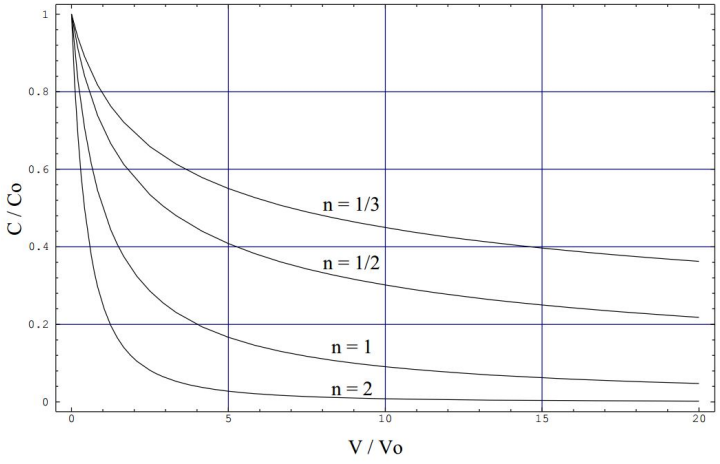

Fig. 2.4: *Capacitance vs Voltage for different varactor junction types [18]*

MEMS

Micro-Electro-Mechanical System (MEMS) technology can be used as variable capacitors (varactors) and capacitive switches. RF MEMS components consist of micro-machined cantilevers or bridges, as shown in Fig. 2.5, which bend in response to applied voltage. MEMS have low losses, low power consumption, and a compact structure, but are fragile, slow-tuning and can in most cases only provide binary to very small tuning ranges [5].

The fragility of the component requires the use of packaging or the need to be designed into a solid structure.

RF MEMS provide integration challenges and in order to achieve a large number of tuning states, it is often required to integrate the switches with a bank of capacitors, resulting in higher losses [11] and leading to complex design problems. Though MEMS have mostly been implemented in low to medium power systems, high-power MEMS switches have also been developed as shown in [19] and [20].

A high power fast tuning capacitive RF MEMS switch with around 0.1 dB insertion loss at X-band is presented in [20]. The capacitive switch has two states: the up-state and the down-state. The up-state yields a capacitance of 40 fF, while the down-state is estimated at 3.1 pF. The switching time between the two states is reported to be below 15 μs.

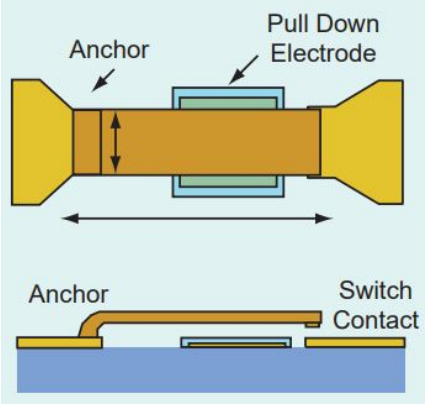

Fig. 2.5: *MEMS Series Switch Configuration [21]*

Other Devices

Optically illuminated silicon dice and piezoelectric-actuators or -motors have been implemented using E-plane resonators. Optically illuminated silicon dice can be used to switch resonators in and out of a circuit [22]. One advantage of this type of switching element is that no biasing lines are needed, simplifying implementation. The dice is capable of handling high power, unlike most MEMS and varactors. The disadvantage of using dice is that external circuitry is required, such as a glass fibre optical cable and an infra-red laser diode, which increases the cost of fabrication.

Apart from the external circuitry required to run piezoelectric-actuators or piezomotors, it is also common to use the piezoelectric-devices with tuning disks when tuning cavity resonators. The actuator or motor can either be used to increase or decrease perturbations into a cavity resonator, or to rotate a circular disk [11]. Though piezomotors are a good alternative to other motors, which are bulky and expensive, they are still more costly and sizeable than MEMS, PIN diodes, dice, and varactors.

Thin film ferroelectric materials, such as barium-strontium-titanate (BST), have a variable dielectric constant when presented with a biasing voltage. Similar to MEMS, ferroelectric components can be fabricated onto the substrate. BST varactors are often fabricated in the form of a parallel plate or interdigital capacitor [23]. Depending on the chosen capacitor topology, the biasing voltage required can range from 5 to 200 V.

BST varactors can offer a low-loss, fast switching solution with a trade-off between size reduction and power handling capabilities.

2.2 Tunable Filters

The next two sections provide information on planar and waveguide filters which have previously been published, and which incorporate some of the discussed tuning components. Since one of the main contributions in this dissertation is a novel biasing structure for planar staircase filters, an emphasis is placed on biasing structures, filter size and performance. The other main contribution proposed is a varactor-tuned evanescent mode waveguide filter, which incorporates varactors by means of a waveguide mounting structure. In literature, there are few evanescent mode waveguide filter designs, therefore Sec. 2.2.2 contains information on the performance and structures of various different types of published waveguide filters.

2.2.1 Tunable Planar Filters

Many published solutions implement tunable filters in microstrip or stripline structures. Although these structures are known for high losses, they are also the smallest and least expensive [12]. The majority of planar tunable filters make use of varactor diodes, micro-electro-mechanical-systems (MEMS), ferroelectric and ferromagnetic components, and PIN diodes.

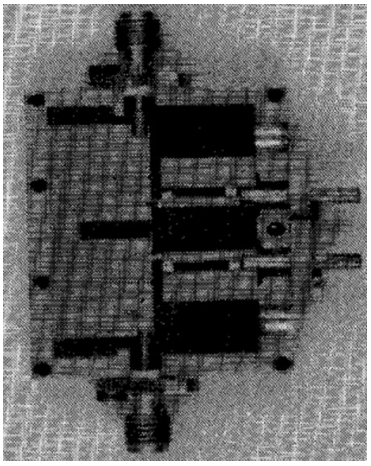

Fig. 2.6: *Varactor-tuned Combline Filter [6]*

Varactor tunable filters have been around for quite some time, but the performance of tuning components have improved in recent years, providing a renewed wave of interest in tunable planar filter design. In 1982, Hunter and Rhodes designed a varactor-tunable 2nd order combline filter [6] which was constructed on suspended substrate stripline. The filter was designed for a centre frequency of 4.5 GHz and a 200 MHz bandwidth. Hunter and Rhodes showed that the varactor loss dominated the insertion loss levels of the designed tunable filter. As the order of a filter increases, the insertion loss also increases due to each varactor adding its own loss [6]. The measured results show a maximum insertion loss of 5.4 dB, a centre frequency tunable from 3.15 GHz to 4.85 GHz, and a 12.3% bandwidth variation across the tuning range. The centre frequency was shifted 340 MHz

lower than the design frequency due to the bond wire inductance of the varactor. In order to have the desired centre frequency, it is required to compensate for the varactor bond wire inductance by shortening the lengths of the resonating lines. The varactor biasing circuitry included an LC filter realised with printed quarter-wave transmission lines and shunt chip capacitors. The manufactured filter is shown in Fig. 2.6 and the area of the substrate is estimated as 30 mm x 30 mm.

A similar design was implemented in 2000 by Brown and Rebeiz, who presented a 4th order varactor-tuned suspended substrate stripline interdigital filter in [9]. The filter was designed for a centre frequency tunable from 660 MHz to 1.6 GHz and a 16 % bandwidth. The measurements yielded a slightly lower tuning range of 700 MHz to 1.33 GHz. Brown and Rebeiz noted that the bandwidth changed as a function of frequency due to the bandwidth of the coupled line impedance inverter at the filter's input and output. The manufactured filter is shown in Fig. 2.7. The size of the filter is estimated as 44 mm x 56 mm including the enclosure. The biasing circuitry included an additional decoupling capacitor of 75 pF.

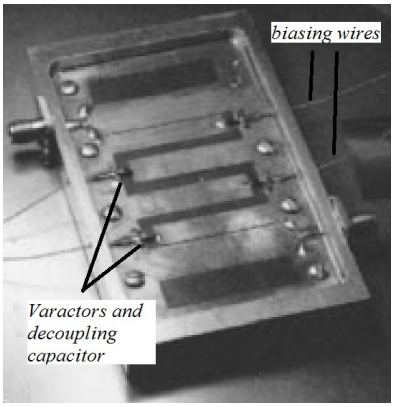

Fig. 2.7: *Varactor-tuned Interdigital Filter [9]*

In 2003 Abbaspour-Tamijani *et al.* presented a miniature MEMS tunable coplanar waveguide filter for K-band frequencies. The filter incorporates MEMS bridge varactors which are tuned with biasing voltages of 0 to 80 V. The measured centre frequency tunability is 18.60 to 21.44 GHz. The bandwidth varies from 7.37 to 7.58 % while the maximum insertion loss across the tuning range is 4.15 dB. The total length of the manufactured filter is 3.26 mm, as shown in Fig. 2.8. Each resonator includes 8 bridge varactors for tuning. Not shown on the figure are the required biasing pads. Abbaspour-Tamijani *et al.* mentioned that the high voltage requirement for tuning may be overcome by using the centre conductor of the coplanar waveguide line, but that this would require an additional decoupling capacitor placed in series with the varactors or coupling inductors.

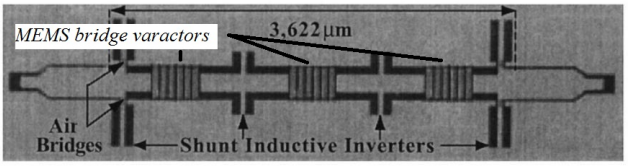

Fig. 2.8: *Miniature MEMS Tunable Filter [24]*

The use of BST varactors in a tunable 3^{rd} order combline filter was presented in 2005 by Nath *et al.* [23]. The filter achieved a centre frequency tunable from 2.44 to 2.88 GHz with a 1 dB bandwidth of 400 MHz when varying the biasing voltage between 0 to 200 V. The insertion loss of the manufactured filter varied from 3.3 to 5.1 dB across the tuning range. The biasing circuitry included additional decoupling capacitors of 1 nF each, which was placed in series with the interdigital BST varactors. The manufactured filter is shown in Fig. 2.9.

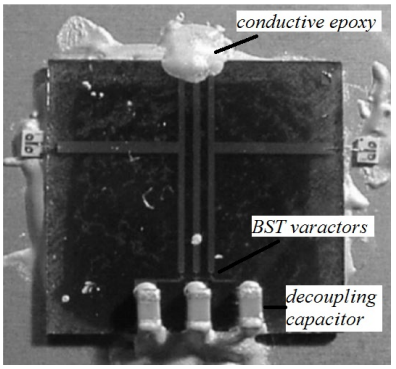

Fig. 2.9: *BST Varactor-tuned Combline Filter [23]*

Another implementation of MEMS varactors in a tunable filter was published in 2010 by El-Tanani and Rebeiz [25]. The second order filter was designed for a constant absolute bandwidth with a centre frequency tunable from 1.5 to 2.5 GHz. The measured insertion loss is less than 2.2 dB across all tuning bands. The manufactured filter is shown in Fig. 2.10. The MEMS varactors are attached to one end of each resonator, while the other end is grounded. Biasing lines are etched onto the substrate and run from the MEMS varactor to the edge of the board. These lines are placed orthogonal to the electric field in the gap between the resonators to minimise coupling to the biasing lines. The biasing lines also have a stepped impedance and are thinner closer to the resonators in order to reduce coupling.

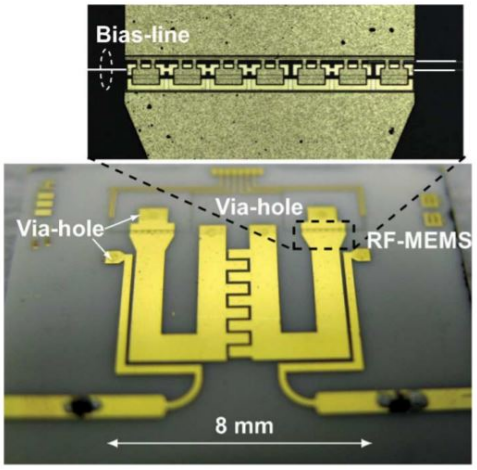

Fig. 2.10: *MEMS-tuned Filter [25]*

In 2012, Guyette demonstrated an intrinsically switched bandpass filter bank [3]. This type of filter bank does not require switches to activate or deactivate the individual filters,

since the on and off switching of each individual filter is done using the same components that provide the centre frequency and/or bandwidth tunability. The filter bank consists of three third order intrinsically switched filters and was fabricated using 60-mil Roger Duroid 4003. The total size of the filter bank is 11.9 cm by 10.1 cm. Each filter design is based on a pseudocombline/combline topology. Varactors are placed at both ends of the pseudocombline resonators. However, for each combline resonator only one varactor can be added since the line is grounded at one end. Biasing lines are included on the printed-circuit-board (PCB), which supplies biasing voltages from the edge of the board, shown in Fig. 2.11. The biasing circuits include 34 nF inductors and 100 pF capacitors for decoupling. There are a total of 15 biasing lines. The filter bank has a centre frequency tuning range of 904 MHz (740 to 1644 MHz) and a constant bandwidth of 50 MHz. The insertion loss was no more than 5 dB for any of the tuning states.

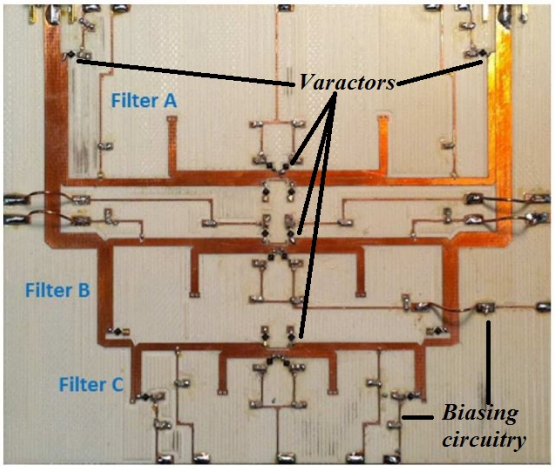

Fig. 2.11: *Intrinsically Switched Filter Bank [3]*

Two years later, Cho and Rebeiz presented an asymmetrically-loaded coupled-line tunable filter that can operate both as a tunable bandpass filter and a tunable bandstop filter using varactors and RF MEMS [26]. The tunable 4^{th} order filter has a centre frequency tunability of 0.78 to 1.08 GHz with a 1 dB bandwidth tunable between 64 and 115 MHz at 0.98 GH. MEMS switches are used to control the coupling coefficients at the source/load, while varactors are used for the tunability of the input/output coupling. The bandpass filter can be transformed into a bandstop filter through the manipulation of the coupling coefficients. When changed to bandstop mode, a rejection level of greater than 40 dB is obtained. The manufactured filter is shown in Fig. 2.12. The varactors are added to the open ends of the resonators for centre frequency tuning, and between resonators for bandwidth tuning. Each biasing circuit includes lines that were etched onto the substrate, two 10 kΩ resistors in series to reduce RF leakage and DC blocking capacitors.

More recently published filters include a varactor-tuned wideband bandpass filter with constant absolute bandwidth presented by Cai *et al.* [27]. The filter consists of asymmetrical half-wavelength resonators which are loaded at one end by varactors and at the other by a fixed capacitance. Other fixed capacitors are added at the input/output coupling, while 51 $k\Omega$ resistors are used as RF chokes for the biasing circuits. The biasing lines are etched onto the substrate, as shown in Fig. 2.13. The filter centre frequency is tunable from 0.43 to 0.72 GHz with a maintained absolute bandwidth of 75 MHz across

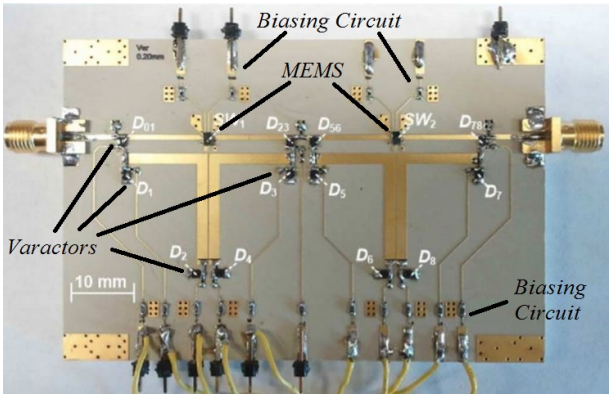

Fig. 2.12: *MEMS-tuned Bandpass-Bandstop Filter [26]*

the tuning range. The insertion loss is less than 3 dB for all tuning bands. This filter has two symmetrical transmission zeros which tune with the centre frequency, resulting in a sharp roll-off in all tuning positions. The transmission zeros are achieved through the implementation of two coupled shunt stubs.

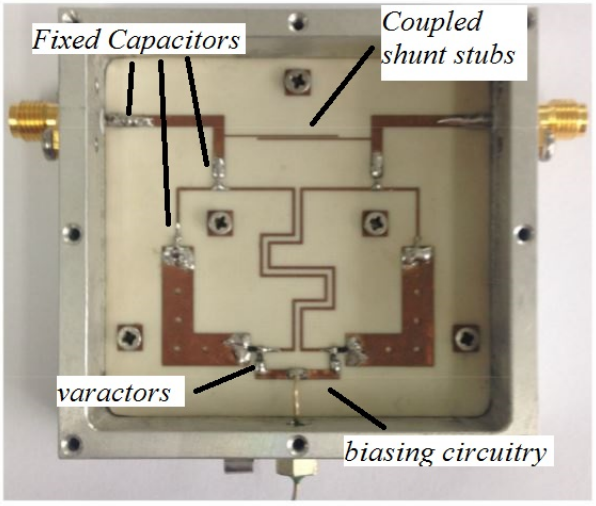

Fig. 2.13: *Varactor-tuned Bandpass Filter with Constant Bandwidth [27]*

In planar microwave filters, the biasing circuitry is normally included on the same layer as the resonators, and is electrically decoupled using capacitors and inductors, resistors, or open- and shunt-circuited lines. At RF and microwave frequencies, resistors are frequently used as RF chokes. For example, [28] and [29] make use of 100 kΩ resistors to decouple their varactor-loaded resonator circuits. An additional decoupling capacitor is often added as shown in the varactor-loaded split-ring resonator circuit in [30], and the varactor-loaded substrate integrated waveguide resonator circuit in [31]. An alternative is to utilize biasing tees [32], or to design an RF choke on the substrate itself. For example, [33] used a quarter-wavelength transformer combined with two parallel capacitive stubs in coplanar waveguide to create an RF choke in the DC path. Many of the standard decoupling circuits are of a resonant nature, which has a detrimental effect when the filter is tuned from its optimum frequency.

2.2.2 Tunable Waveguide Filters

Planar filters with RF MEMS, varactors, or ferroelectric components have many advantages, such as compact size, fast tuning speeds and wide tuning ranges, but the power handling capabilities of the filter can rarely compete with that of filters in waveguide structures. By using evanescent-mode cavities, a higher power tunable filter can potentially be realised at the expense of size and cost.

The cavity-loading technique used for the design of modern day evanescent-mode filters has been incorporated into tunable filters since the 1970s [15]. However, these filters were mechanically-tuned, whereas most modern day designs incorporate electrical tuning. Using the tuning components discussed in Sec. 2.1, various waveguide filters have been realised in the last few years.

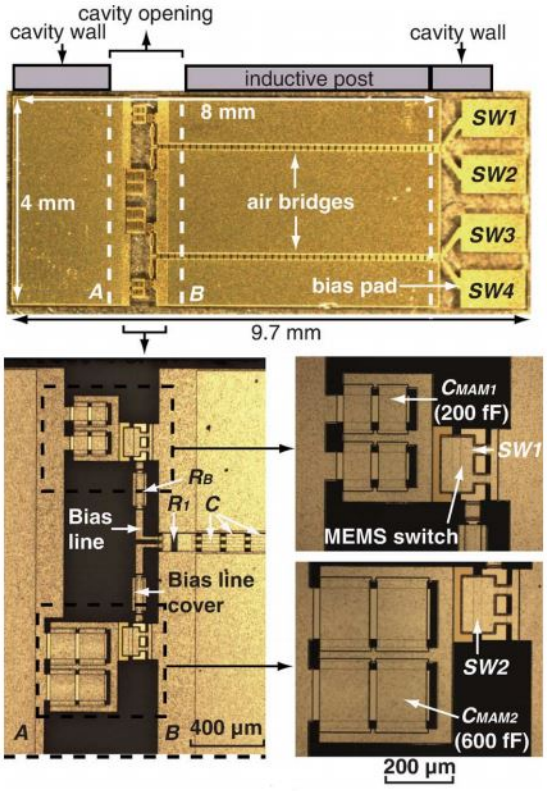

(a) MEMS-tuning chip

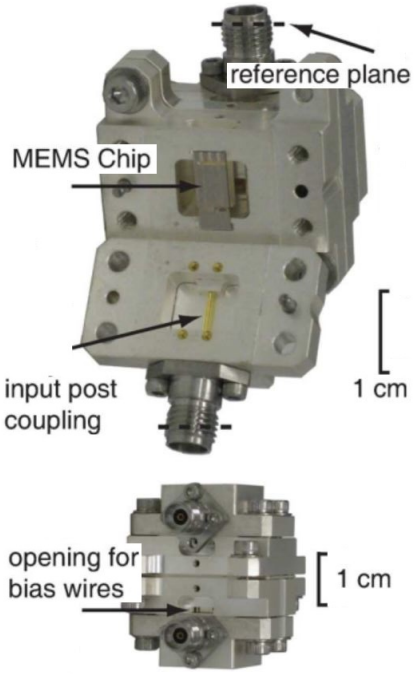

(b) Fabricated Filter

Fig. 2.14: *MEMS-tuned Evanescent Mode Waveguide Filter [34]*

In 2010, a second order MEMS-tuned evanescent mode cavity filter was presented by Park *et al.* [34]. The filter makes use of an inductive coupling pin for input and output coupling. MEMS switches are implemented on a quartz substrate and mounted on a capacitive metal post inside of the waveguide. An additional coupling iris is included in the centre of the two resonators to achieve the desired inter-resonator coupling. Miniature cavity openings are used for the biasing wires, which are placed at a point of zero RF voltage to minimise the effect of the wires on the filter performance. The manufactured filter and the MEMS chip is shown in Fig. 2.14. The measured filter achieved a centre frequency tunability from 4.07 to 5.58 GHz, an insertion loss of less than 5 dB and a bandwidth between 17.8 and 41.1 MHz across the tuning range.

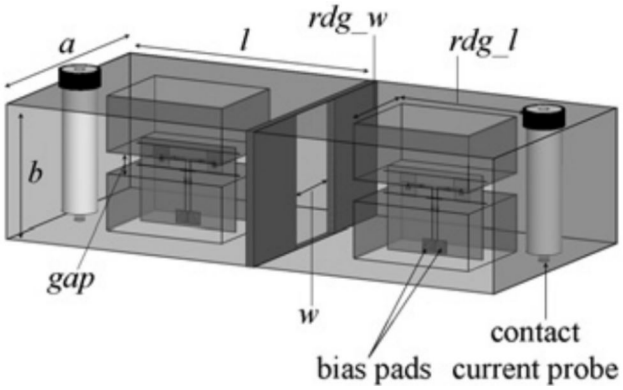

Fig. 2.15: *Digitally-tuned Evanescent Mode Waveguide Narrow Band Filter [35]*

Another second order tunable evanescent mode filter was presented by Amadjikpe *et al.* [35] with two back-to-back ridge inserts in each waveguide section. In between the ridges a MEMS switching structure is implemented. The filter achieved discrete tuning of three states around 3 GHz while the bandwidth varied between 1.2 and 1.5 %. For all tuning states, the insertion loss was better than 2.1 dB. The filter tuning circuit consists of two digitally tuned capacitors, and MEMS switches. The biasing structure consists of etched biasing lines and on-board 1 MΩ decoupling resistors implemented both inside and outside the guide. The filter design is shown in Fig. 2.15, where *rdg* refers to ridge.

Piezomotors offer a cavity resonance tuning solution by means of low-loss tunable perturbations. One example of a motor-based cavity filter is presented by Fouladi *et al.* in [36], where a 6^{th} order filter was designed for WiMAX applications. The filter consists of six resonant cavities each with its own piezomotor tuning system. The piezomotors control the air gaps between circular disks and cylindrical posts inside the waveguide cavities, as shown in Fig. 2.16b. The piezomotor is mounted on top of the waveguide roof and requires a metallic bracket for mounting, as shown in Fig. 2.16a . The motor shafts are connected to circular tuning disks. The filter design is shown in Fig. 2.16. The measured response achieved a 4% tuning range from 2.565 GHz to 2.645 GHz and an insertion loss which varies from 0.9 dB to 2.3 dB.

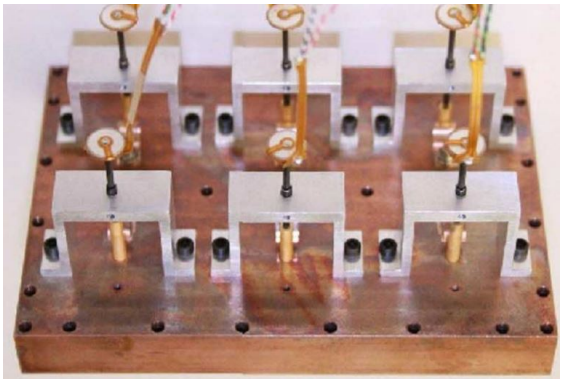

(a) Piezomotor Tuning System

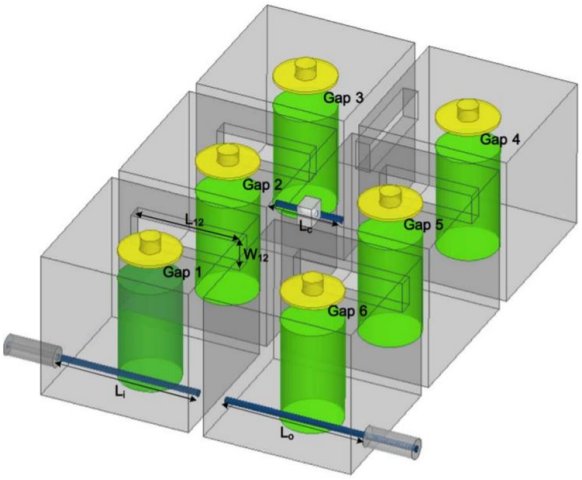

(b) 3-D Filter Model

Fig. 2.16: *Piezomotor-tuned Waveguide Filter [36]*

Fouladi *et al.* also presented a smaller alternative waveguide tuning method to the piezomotors in [36]. This filter uses external MEMS circuits to control the capacitance between metallic posts and disks inside the waveguide. MEMS switches are used in series with ceramic capacitors and tuning screws, as shown in Fig. 2.17b. Each tuning screw is also connected to a circular disk. Though the position of a tuning disk is determined mechanically, the capacitance between a disk and metallic post is altered by loading the disk with MEMS and ceramic capacitors. The biasing circuit for the MEMS switches include biasing lines etched on the PCB, decoupling ceramic capacitors and resistors. The measured filter achieved a 44 MHz centre frequency tuning range (2.590 GHz to 2.634 GHz) with an insertion loss less than 4.25 dB across the tuning range. The filter bandwidth was 28 MHz at 2.606 GHz. The size of each MEMS-tuning chip is 2.5 cm by 2.5 cm and each cavity is 30 mm x 30 mm x 30 mm.

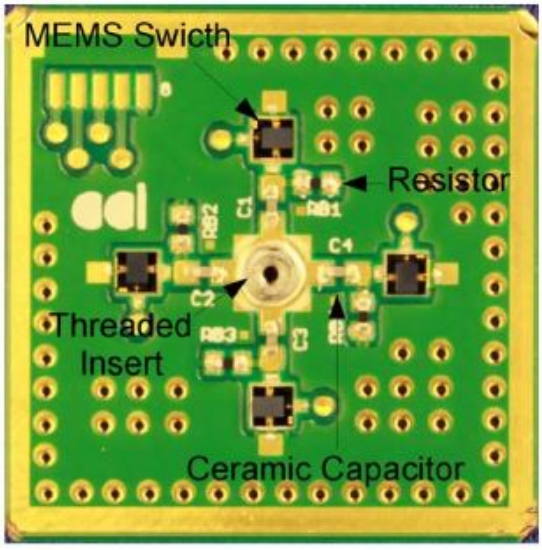

(a) MEMS-tuning chip

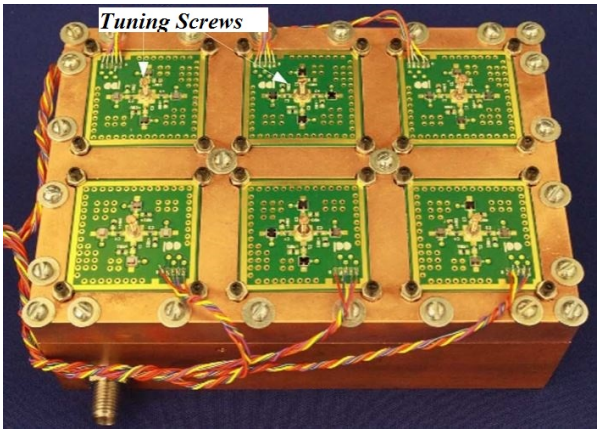

(b) Fabricated Filter

Fig. 2.17: *MEMS- and Piezomotor-tuned Waveguide Filter [36]*

An interesting alternative to tuning with piezomotors and MEMS, is to use optically illuminated silicon dice. Silicon dice have high power handling capabilities and do not requiring any biasing circuitry, which simplifies the design process and eliminates any loss associated with the biasing circuitry. A laser diode is required for the control circuit of silicon dice. The resonator presented by Mohottige *et al.* consists of an E-plane waveguide section with a drilled hole in the side of the waveguide for a laser diode, two metallic septa inside the guide, and a fin hanging from the roof to which the dice is attached [22]. The resonant structure is shown in Fig. 2.18. The dice changes from an insulator to a near conductor when the laser illuminates it, causing the length of the metal fin to increase. The measurements show a centre frequency shift of 550 MHz (9.615 GHz to 10.125 GHz) from the off-state to the on-state, with an insertion loss of 0.7 dB and 2.7 dB respectively. The bandwidth is estimated as 2.5 % at 10.125 GHz.

Using tunable components is not the only option for tunability. Some designs incorporate magnetically tunable materials, such as ferromagnetic materials, and other liquid metals which are tuned hydraulically. A tunable X-band substrate integrated waveguide filter with liquid metal posts is presented in [37]. The posts are activated or deactivated

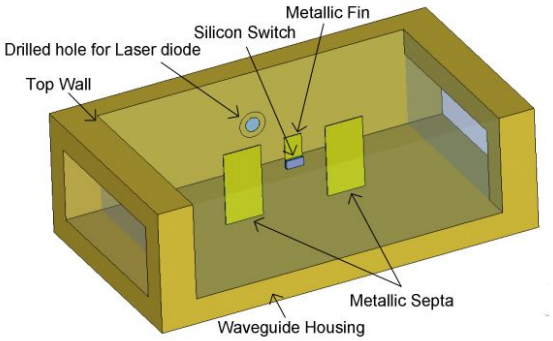

Fig. 2.18: *Optically-tuned Waveguide Filter [22]*

by means of a hydraulic control system. Though the need for biasing circuitry is eliminated, an external pump is required. The pump creates a more sizeable control element for the filter, but the advantage is the elimination of parasitics associated with biasing circuitry and tuning components. The single cavity filter with four tuning posts is capable of centre frequency tuning in five states from 10.13 GHz to 11.31 GHz. The fractional bandwidth varies between 0.6% and 1%, but the insertion loss remains low and peaks at 1.35 dB. The filter design and cross-section is shown in Fig. 2.19.

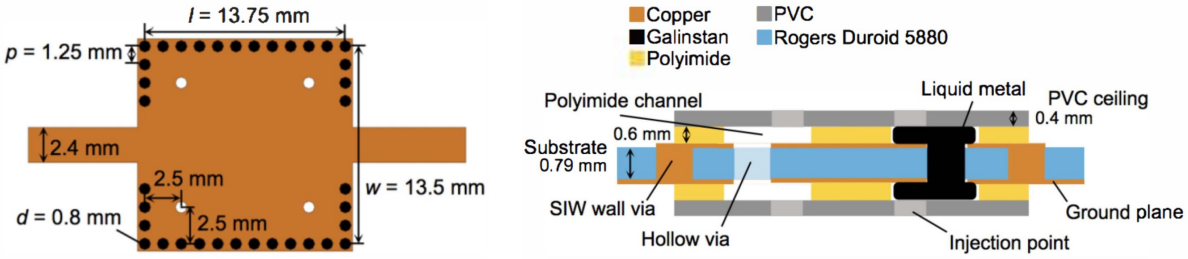

(a) SIW Filter Design

(b) SIW Filter Cross Section

Fig. 2.19: *Liguid-metal-tuned SIW Filter [37]*

An example of a magnetically tunable filter is presented by Belayev *et al.* in [38]. A 2^{nd} order filter is manufactured using polycrystalline ferrite slabs, which are held in place by truncated metal pyramids. The pyramids enable wide tuning ranges to be achieve by focusing the high frequency magnetic field in the area of the ferrite slabs. The permeability of the ferrite slabs are altered by means of biasing magnetic fields. This change in permeability results in centre frequency tuning. To achieve the desired biasing magnetic field, Helmholtz coils are used. The biasing magnetic field propagates along the filter axis perpendicular to the TE_{10} mode, which is the mode of operation. The manufactured filter is shown in Fig. 2.20. A centre frequency tunable from 8.74 to 9.63 GHz, with a bandwidth varying between 80 and 76 MHz, and an insertion loss of less than 4.1 dB for all tuning states, is achieved.

In waveguide filters, external control systems are often used in order to obtain high quality factors and good power handling capabilities. However, the need for external circuitry increases the size of a filter structure and may complicate the incorporation of that filter into a systems.

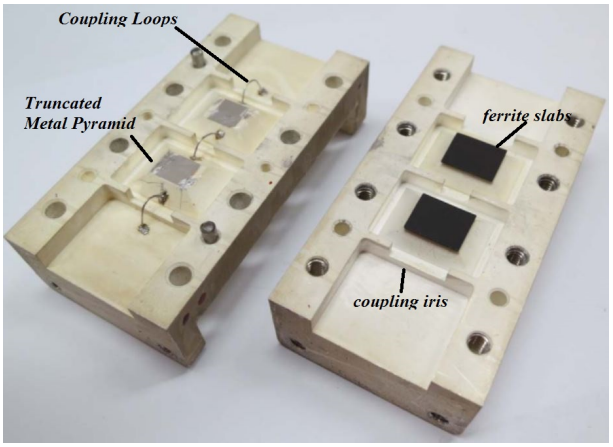

Fig. 2.20: *Magnetically-tuned Waveguide Filter [38]*

2.3 Conclusion

There are always trade-offs to consider when choosing a tuning component, as is shown by the filter examples discussed in this chapter. MEMS switches and silicon dice function well at X-band frequencies; however, these components are expensive and difficult to obtain. Many tunable filters require external circuitry to achieve tunability. One of the aims for this project is to produce filter prototypes which minimise the amount of external components and circuitry required to achieve tunability.

Many of the planar and waveguide filters presented in this chapter require additional decoupling circuits when biasing the tuning components. In both the proposed planar and waveguide filter designs in this dissertation, the only biasing component necessary is a thin wire, which is placed strategically to minimise any field leakage and coupling.

Although varactor diodes are arguably the most lossy of all the components mentioned in this chapter, and have low maximum power dissipation ratings, these components are cost-effective, readily available, have low power consumption and are easily implemented due to the packaging options. Varactors come in various tuning ranges, abrupt or hyper-abrupt, and require minimal additional circuitry for biasing which greatly simplifies the filter design.

The SMV1405-240 and SMV2019-203 varactors from Skyworks Inc. are chosen for the planar and waveguide filter designs presented in this dissertation, respectively. Each diode is chosen for its usability at X-band, low series resistance, tuning capability, and ease of incorporation into the structure. In the following chapter, the SMV1405-240 is characterized and a model generated for accurate simulation purposes.

Chapter 3

Basic Tunable Filter Concepts

The key circuit components of both filter classes presented in this dissertation are coupled resonator filters, and equivalent circuits for tuning elements. This chapter reviews the fundamental method for designing a coupled resonator filter and includes a basic first order filter design, the design equations for an n^{th} order coupled resonator filter, and a discussion on the effects of centre frequency tunability on the filter response. Further in this chapter, a model extraction method is presented in which a circuit model for the SMV1405 varactor used for the planar filter is created. The model enables the simulation of the entire tunable filter, and is incorporated into both 2-D and 3-D simulations. The model includes the effects of parasitics, which can be detrimental to the filter response if not considered in the design stage. The theory, design principles and model extraction methods are of use in both proposed contributions, but can be extended to other tunable coupled resonator filters as well.

3.1 Coupled Resonator Filter Theory

The most commonly-used synthesis method for filter design is the insertion loss method, which involves designing for a specified analytical frequency response [39]. A low-pass filter prototype, normalized in both frequency and impedance, is the typical starting point for this method. There are many books, including [39] and [1], that provide element value tables for low-pass filter prototypes with well-known filter responses such as maximally-flat, Chebychev, and elliptical. In order to develop a bandpass filter from the low-pass prototype, a series of impedance and frequency transformations are performed. For communication system applications, narrow-band filters with a bandwidth of less than 10 % are often required. Narrow band coupled-resonator designs are very suitable for these bandwidths.

In order to design a coupled-line coupled-resonator bandpass filter, two methods may be considered: designing from a low-pass prototype, or from the coupling matrix and loaded quality factors. The main advantage for designing with the coupling matrix is that all inter-resonator coupling can be taken into account. Since the filters considered in this dissertation have negligible coupling between non-adjacent resonators, both methods will yield similar results. The more traditional method is therefore chosen to give insight into the progression from low-pass to tunable bandpass filters. The traditional method begins with a low-pass ladder network prototype and performs a series of transformations. The true power of the coupled-resonator theory lies in that the equations hold approximately for any type of resonator, be it lumped element, transmission line, planar, or waveguide

resonators.

3.1.1 First Order Lumped Element Coupled Resonator Bandpass Filter Design

An odd order low-pass prototype network can take two forms, as shown in Fig. 3.1. The first circuit is terminated in a resistance, while the second is terminated in a conductance. The element values, labelled as g_i for $i = 0, 1, ...n + 1$ for an n_{th} order filter, are specific to the desired response. The equations to calculate the prototype values can be found in [1].

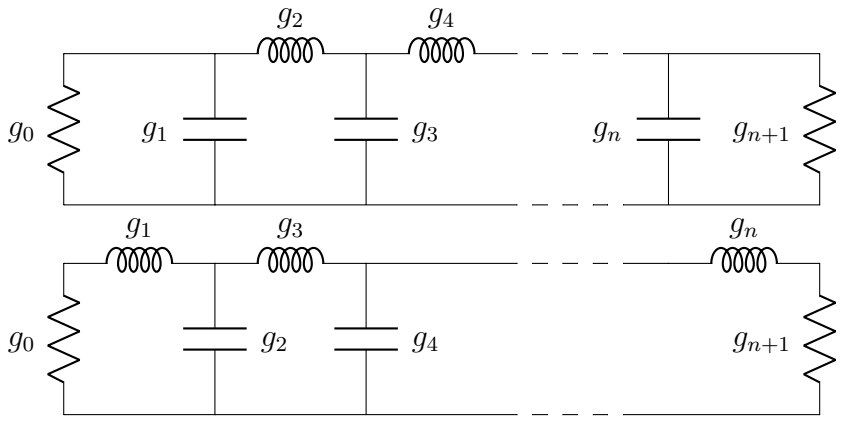

Fig. 3.1: *Low-Pass Prototype Circuits*

For a Chebychev response, the element values for a doubly terminated circuit, having an equi-ripple cut-off radial frequency of $\omega_l' = 1$ and a termination of $g_0 = 1$, are calculated using the following equations [1]:

$$\begin{aligned} \beta &= \ln\left[\coth\left(\frac{L_{Ar}}{17.37}\right)\right] \\ \gamma &= \sinh\left(\frac{\beta}{2n}\right) \\ a_k &= \sin\left[\frac{(2k-1)\pi}{2n}\right] \\ b_k &= \gamma^2 + \sin^2\left(\frac{k\pi}{n}\right) \end{aligned} \tag{3.1.1}$$

$$\begin{aligned} g_1 &= \frac{2a_1}{\gamma} \\ g_j &= \frac{4a_{j-1}a_j}{b_{j-1}g_{j-1}} \\ g_{n+1} &= 1, \text{ for } n \text{ odd} \end{aligned} \tag{3.1.2}$$

for $k = 1, 2, ..., n$ and $j = 2, 3, ..., n$, where L_{Ar} is the desired passband ripple in dB, and n is the order of the filter.

Both circuits in Fig. 3.1 are suitable starting points for the design; however, for easy reference to the designs presented in this dissertation, the second circuit in Fig. 3.1 is chosen as the starting point for the first order design.

To illustrate the transformation process required in designing a coupled resonator filter from a low-pass prototype, a first order filter suffices. Such a prototype is shown in Fig. 3.2.

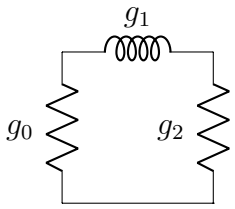

Fig. 3.2: *First Order Low-Pass Prototype Circuit*

Admittance and impedance inverters are the key elements required for designing a coupled resonator filter. Though admittance and impedance inverters are equivalent structures, the designs described in this dissertation make use of only admittance inverters.

An admittance inverter, or J-type inverter as shown in Fig. 3.3, relates the input and load admittance through the following equation,

$$Y_{in} = \frac{J^2}{Y_L} \tag{3.1.3}$$

Since the load is inverted, these types of inverters can be used to change series elements to shunt elements and vice versa. An additional property of the admittance and impedance inverters is that they also change the phase by $\pm 90^o$.

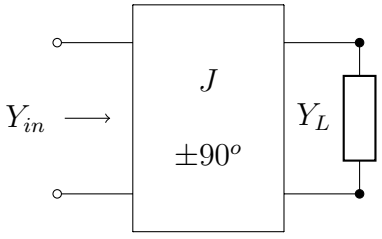

Fig. 3.3: *Admittance Inverter*

The admittance inverter can easily be realised by using a quarter wave transformer with a characteristic admittance $Y_0 = J$, or a Π-network of either capacitors or inductors as shown in Fig. 3.4. For the capacitive network, $J = \omega C$, while for the inductive network, $J = -1/(\omega L)$. The insertion of admittance inverters into the first order low-pass network in Fig. 3.2 converts the series inductor to a shunt capacitor as shown in Fig. 3.5. Since tunable filters mostly utilize tunable capacitive elements, this conversion is desired.

Fig. 3.4: *Admittance Inverter Equivalent Models*

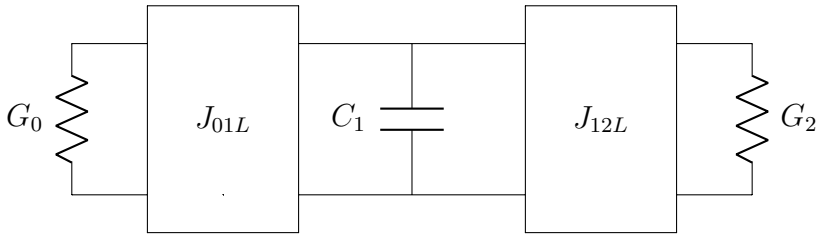

Fig. 3.5: *First Order Low-Pass Prototype Circuit with J-inverters*

The admittance inverters in Fig. 3.5 are defined by the following equations, where the subscript L indicates the low-pass prototype.

$$J_{01L} = \sqrt{\frac{G_0 C_1}{g_0 g_1}}$$
$$J_{12L} = \sqrt{\frac{G_2 C_1}{g_2 g_1}} \tag{3.1.4}$$

For bandpass filters, the low-pass circuit is transformed using the standard low-pass to bandpass transformation method described in both [1] and [39]. This method consists of replacing the radian frequency with the following equation,

$$\omega \rightarrow \frac{-1}{\Delta}\left(\frac{\omega}{\omega_0} - \frac{\omega_0}{\omega}\right) \tag{3.1.5}$$

The fractional bandwidth (Δ) is given by

$$\Delta = \frac{\omega_2 - \omega_1}{\omega_0} \tag{3.1.6}$$

where ω_1 and ω_2 correspond to the lower and upper frequency limits of the equi-ripple band, respectively.

This method transforms the parallel capacitor into a parallel LC resonator. Figure 3.6 shows the converted circuit where the subscripts B and b refer to the bandpass nature of the circuit. The element values are calculated as follows:

$$J_{01B} = J_{01L}$$
$$J_{12B} = J_{12L}$$
$$C_{b1} = \frac{C_1}{\omega_0 \Delta}$$
$$L_{b1} = \frac{\Delta}{\omega_0 C_1} \tag{3.1.7}$$

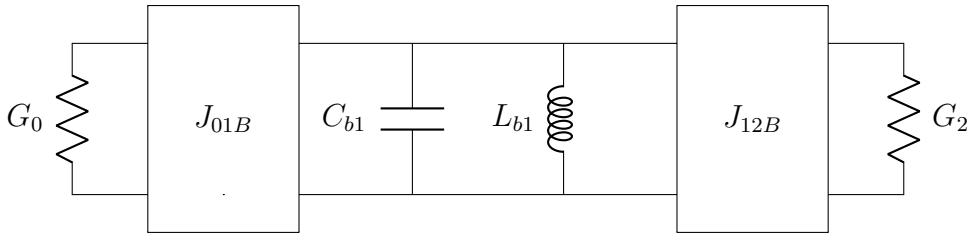

Fig. 3.6: *First Order Band-Pass Prototype Circuit with J-inverters*

It is important to remember that the low-pass prototype consists of a circuit with a normalised terminating impedance. Since the admittance of the system in which the filter is to be incorporated is not equal to one, an admittance scaling should be performed to scale the terminations to an admittance of Y_A, as shown in Fig. 3.7.

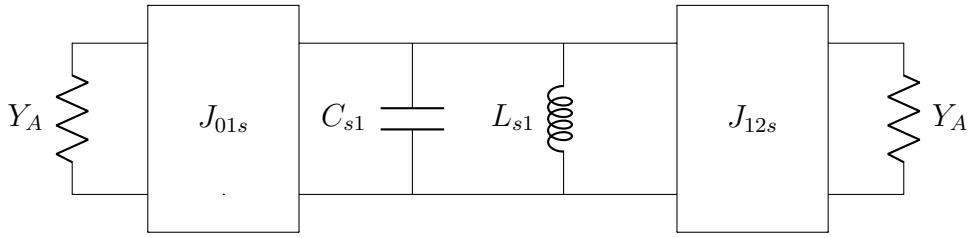

Fig. 3.7: *Scaled First Order Band-Pass Prototype Circuit*

The element values for the circuit in Fig. 3.7 is given by,

$$\begin{aligned} J_{01s} &= Y_A J_{01B} = Y_A\sqrt{\frac{G_0 C_1}{g_0 g_1}} \\ J_{12s} &= Y_A J_{12B} = Y_A\sqrt{\frac{G_2 C_1}{g_2 g_1}} \\ C_{s1} &= Y_A\frac{C_1}{\omega_0\Delta} \\ L_{s1} &= \frac{\Delta}{Y_A\omega_0 C_1} \end{aligned} \tag{3.1.8}$$

where the subscript s indicates an impedance scaled circuit element. Since $g_0 = g_{n+1}$ for n odd, $J_{01s} = J_{12s}$, the circuit is symmetrical about the resonator.

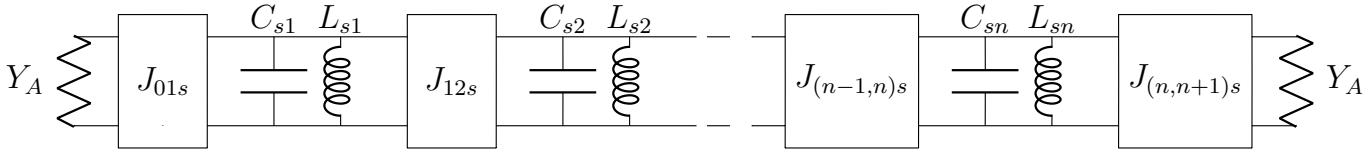

Fig. 3.8: *n^{th} Order Lumped Element Band-Pass Filter Model*

A similar approach can be used to synthesize a filter of a higher order. For an n_{th} order filter circuit, as given in Fig. 3.8, the element values are calculated using the following equations:

$$\begin{aligned}
J_{01s} &= Y_A J_{01} = Y_A \sqrt{\frac{G_0 C_1}{g_0 g_1}} \\
L_n &= \frac{\Delta}{Y_A \omega_0 C_n} \\
J_{(n,n+1)s} &= Y_A \sqrt{\frac{G_{n+1} C_n}{g_{n+1} g_n}} \\
L_{si} &= \frac{\Delta}{Y_A \omega_0 C_i} \\
L_{s(i+1)} &= \frac{\Delta}{Y_A \omega_0 C_{i+1}} \\
J_{(i,i+1)s} &= Y_A \sqrt{\frac{C_{i+1} C_i}{g_{i+1} g_i}} \text{ , for } i = 1 \text{ to } n-1
\end{aligned} \tag{3.1.9}$$

It is clear that the designer is free to choose either the admittance inverter or the resonator characteristics.

The admittance inverters in a coupled resonator filter circuit are directly related to the electric and magnetic coupling at the input and output, or between resonators. For identical resonators, $(L_{s1} = L_{s2} ... = L_{sn} = L_0)$, the coupling factors between the resonators are directly proportional to the inverter values, expressed as:

$$k_{ij} = \frac{J_{ij}}{b_0} \text{ , for } i = 1 \text{ to } n-1 \text{ and } j = 2 \text{ to } n \tag{3.1.10}$$

where b_0 is the susceptance slope parameter of the resonators and k_{ij} is the coupling coefficient between the i^{th} and j^{th} resonator. The i^{th} resonator's susceptance slope parameter (b_i) can be related to its susceptance (B_{ri}) as follows:

$$b_i = \frac{\omega_0}{2} \frac{\delta B_{ri}}{\delta \omega}|_{w_0} \tag{3.1.11}$$

The input and output coupling is described by the loaded quality factors q_S and q_L for the source and load side respectively.

$$q_S = \frac{g_0 g_1}{\Delta} = q_L \tag{3.1.12}$$

The equations above show that the coupling, bandwidth, and input and output loaded quality factors are all interdependent. The bandwidth of the filter is directly proportional to the coupling between the resonators and indirectly proportional to the input and output loaded q's.

For centre frequency tunability, the most convenient implementation is to choose all the resonators identical to one another, since the same tuning element can then be used for all resonators.

3.1.1.1 Adding Tunability to the Design

The first order coupled resonator bandpass filter can be made tunable by adding a variable capacitor, as shown in Fig. 3.9. Since the resonant frequency is given by

$$\omega_0 = \sqrt{\frac{1}{L_0(C_0 + C_v)}} \tag{3.1.13}$$

the frequency decreases as the capacitance increases if the inductance remains constant.

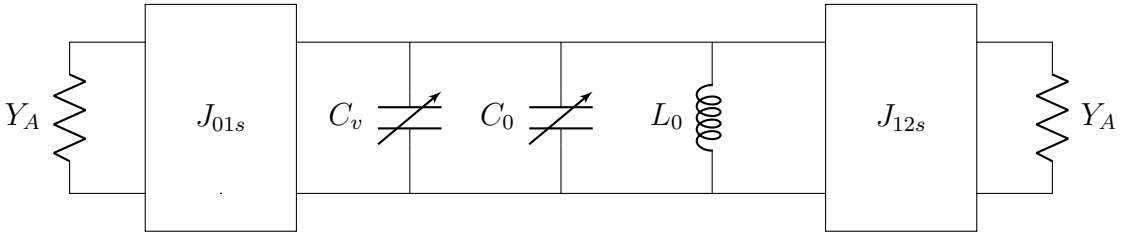

Fig. 3.9: *First Order Lumped Element Ideally Tunable Band-Pass Filter*

If we assume a constant inductance of $L_0 = 1$ μH, the resonant frequency changes at a rate of $\sqrt{\frac{1}{(C_0+C_v)}}$, as depicted in Fig. 3.10 where the total capacitance is changed from 0.1 pF to 10 pF.

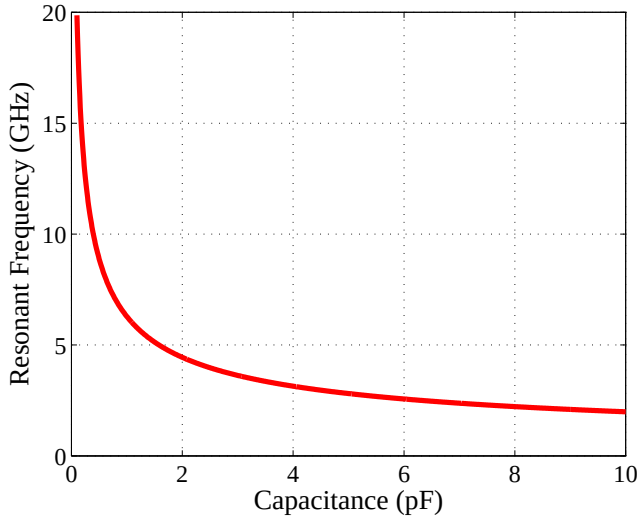

Fig. 3.10: *Resonant Frequency as a Function of Capacitance*

The ratio of the maximum to minimum centre frequency for this circuit is then:

$$\frac{f_{0_{max}}}{f_{0_{min}}} = \frac{\sqrt{L_0 C_0}}{\sqrt{L_0(C_0 + C_v)}} = \sqrt{\frac{C_0}{C_0 + C_v}} \tag{3.1.14}$$

Other factors that are affected when tuning the filter centre frequency include the coupling factor, the bandwidth and the loaded q.

3.1.2 Regarding the Coupling, Loaded Q and Bandwidth in Tunable Coupled-Resonator Circuits

The ideal coupling circuit for a coupled resonator filter is one that maintains a constant coupling coefficient regardless of the frequency. This would result in a constant relative bandwidth while the centre frequency is tuned.

The normalized coupling, K, relates the absolute bandwidth ($\Delta\omega$) and the coupling coefficient (k) as follows:

$$k = K\Delta = K\frac{\Delta\omega}{\omega_0} \tag{3.1.15}$$

For constant absolute bandwidth, $k\omega_0$ must be constant. For constant relative bandwidth ($\frac{\Delta\omega}{\omega_0}$ constant), k must be constant.

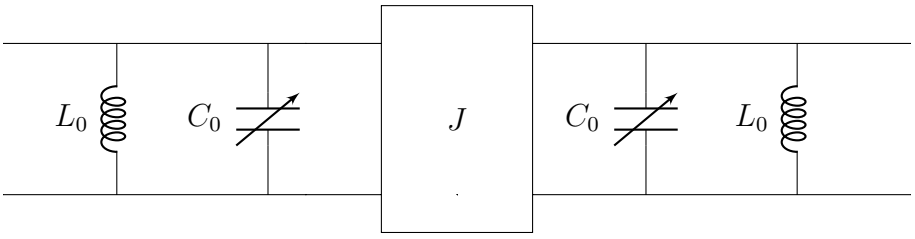

Fig. 3.11: *Two Coupled Lumped Element Resonators*

Consider the coupled resonators as presented in Fig. 3.11. The coupling factor is related to the admittance inverter as,

$$k = \frac{|J|}{b_0} \tag{3.1.16}$$

where b_0 is the susceptance slope parameter of both resonators, and is given by the following equations:

$$b_0 = 1/(\omega_0 L_0) = \omega_0 C_0 \tag{3.1.17}$$

Hence, the coupling coefficient is equal to

$$k = \frac{B_i}{\omega_0 C_0} = \omega_0 L_0 B_i \tag{3.1.18}$$

If the capacitive Π- network in Fig. 3.4 is used as the inverter, $B_i = \omega C$ and the resulting coupling factor is

$$k_C = \frac{\omega C}{\omega C_0} = \frac{C}{C_0} \tag{3.1.19}$$

Since the coupling changes if the resonator's capacitance is varied (i.e. with a change in resonant frequency), a constant relative bandwidth during tuning is not possible for capacitively coupled resonators. This can be related back to the general coupling equation (eq. 3.1.10) for equal resonators ($C_1 = C_2 = C_0$) to give

$$\Delta = \frac{C\sqrt{g_1 g_2}}{C_0} \tag{3.1.20}$$

Therefore, the bandwidth is inversely proportional to the resonator's capacitance.

Another option is to create a filter by utilizing an inductive Π- network admittance inverter, as shown in Fig. 3.4, where $B_i = \frac{1}{\omega L}$. In this case, the resulting coupling coefficient is given by

$$k_L = \frac{1}{\omega_0^2 L C_0} \tag{3.1.21}$$

For the case where L_0 is kept constant,

$$C_0 = \frac{1}{\omega_0^2 L_0} \tag{3.1.22}$$

in which case, the inductive coupling coefficient becomes,

$$k_L = \frac{L_0}{L} \tag{3.1.23}$$

If the resonator and admittance inverter inductances remain constant, it is possible to have a frequency invariable coupling factor and a constant relative bandwidth.

In general, microwave filters never display either of the circuit behaviours of the above. Typically, coupling between resonators is a combination of both capacitive and inductive coupling, where domination depends on the exact structure. In addition, the coupling rarely has the same frequency dependency as the resonant frequency, as the former is often a lumped reactive effect, while the latter depends fully on the resonator implementation. However, the general trend that inductively coupled filters display more constant relative bandwidth behaviour than that of capacitively coupled ones, remains valid. For instance, an inductively coupled combline structure has one of the most constant relative bandwidth properties of all microwave filters.

Concerning the two proposed filter designs in this dissertation, the planar coupled-line filter has both inductive and capacitive coupling, which means that neither of the inverter model options is a perfect model for the coupling. Frequency independent coupling is not possible for the proposed planar filter. The evanescent mode waveguide section itself is modelled as an inductive Π-network with the element values depending on hyperbolic functions. According to the calculations shown above, one would expect frequency independent coupling to be possible in an evanescent mode waveguide filter, but eq. 3.1.23 is only independent of frequency if the values of L_1, L_2 and L are constant, which unfortunately, in the case of the evanescent mode waveguide filter is not the case. On the contrary, the values of the inductors in the evanescent mode filter model are hyperbolic functions dependent on frequency. This results in a complex relationship which is explained in Ch. 5.

3.2 Non-Ideal Tuning Elements

The circuit given in Fig. 3.7 represents an ideal model for a tunable filter, and does not take tuning component parasitics into account. For realistic simulation results at X-band, it is necessary to include the parasitic effects of the chosen tuning component and its packaging. For this, an accurate circuit model is required.

Many manufacturers provide S-parameter files and Spice models for some of their components, but few components are measured and characterised at X-band, and only some packaging options are used for characterisation. Therefore, one of the best options for accurate component modelling when designing for tunability at X-band, is to perform a circuit model extraction specifically for the component under consideration. This section

provides a brief overview of varactor theory, presents the measured and calibrated data, and gives a detailed description of the model extraction procedure.

3.2.1 Extraction of a Varactor Model

For the proposed tunable planar filter, the Skyworks SMV1405-240 varactor is considered due to the specified suitability for application up to 18 GHz, high Q, low series resistance, availability, cost and hermetic packaging. To demonstrate the extraction of a varactor model, a circuit model for the SMV1405-240 varactor is created by means of S-parameter measurements and a post-measurement through-reflect-line (TRL) calibration, presented in Appendix A. Existing varactor models and the extracted model are all compared to the TRL calibrated measurements. For the initial starting point of the circuit, it is important to consider the material and packaging characteristics of the component.

At microwave frequencies, such as X-band, the performance of a varactor is significantly influenced by the packaging and the manner of incorporation into the circuit. For planar structures, surface-mount components are widely used due to easy incorporation. Often, the packaging effects of the varactor are not included in the specifications of the component's data sheet, making it advisable to measure a sample.

3.2.1.1 Measured Varactor Samples

The two port S-parameters of the chosen varactor, Skyworks SMV1405-240, are measured from 7 GHz to 11 GHz using a network analyser calibrated with SOTL (short-open-thru-line). Four circuits are measured, namely a through, line, reflect, and varactor circuit biased from 0 to 30 V in 10 V increments. Using the TRL standards, a post-measurement TRL calibration is performed. The varactor measured response pre- and post TRL calibration for various biasing voltages are shown in Fig. 3.12.

The varactor S-parameters are de-embedded from the varactor circuit using the through, line, and reflect measurements together with TRL calibration calculations in MATLAB, as described in Appendix A. The post-calibration measurements are presented on a Smith Chart in Fig. 3.13. For ease of reference, the post-calibration measured results are from now on referred to as the calibrated measurements of the varactor. The shift in S_{11} frequency from pre- to post-calibration is due to the additional length added by the mounting circuit from which the varactor is measured.

From the datasheet, a $1:1.22$ range in capacitance is expected when biasing between 20 and 30 V. Extracting the equivalent C from the measurements at 7.15 and 7.9 GHz by means of the relationship $\omega_0 = 1/\sqrt{LC}$ results in a $1.1:1$ range. Therefore, the calibrated measurements yield a slightly smaller tuning range than expected.

From Fig. 3.13 it is clear that the varactor has both inductive and capacitive properties which are shifted to mostly capacitive as the biasing voltage changes from 30 V to 0 V. The measurements also show a resonance and resistance which shift as the biasing voltage is changed. Therefore, from the measurements it is plausible to suggest that a lossy resonant circuit (RLC resonator) may be a good model for this varactor measurement.

It is possible to use the calibrated S-parameters directly for the simulation of the filter, but this limits the simulation to specific combinations of biasing voltages. To determine the correct combination of biasing voltages for the proposed 5^{th} order planar filter will also be tedious, since the calibrated S-parameters for the different biasing voltages would constantly need to be interchanged and re-simulated. This is costly both in time and simulation resources.

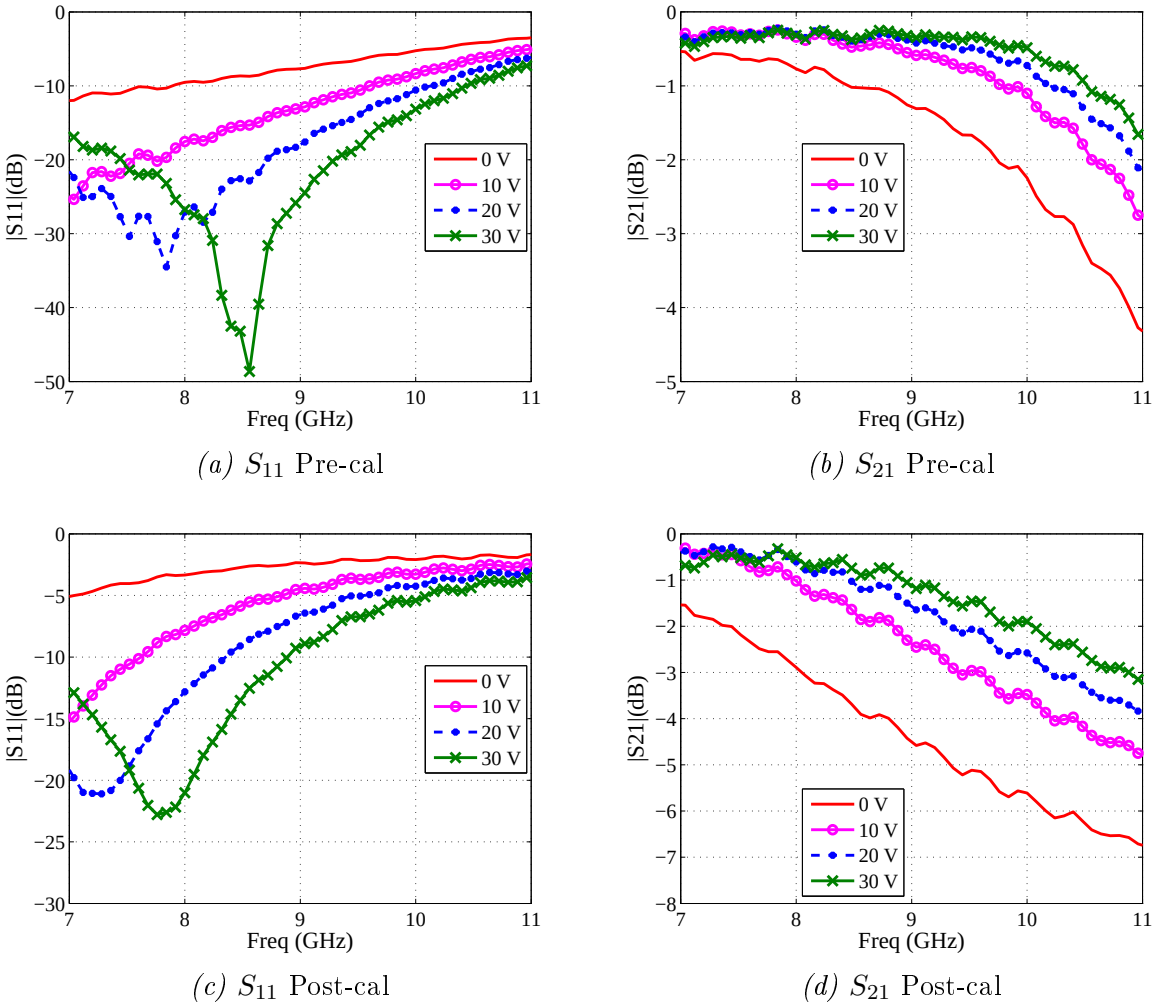

(a) S_{11} Pre-cal *(b)* S_{21} Pre-cal

(c) S_{11} Post-cal *(d)* S_{21} Post-cal

Fig. 3.12: *Varactor S-parameters: Pre- and Post TRL Calibration*

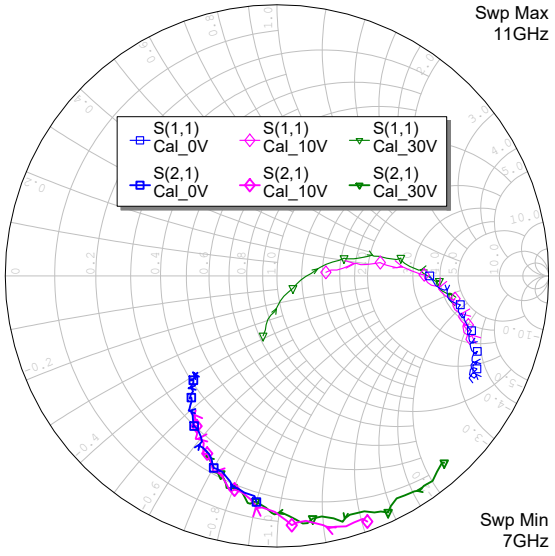

Fig. 3.13: *SMV1405-240 Calibrated S-Parameter Measurements*

Therefore, in order to simulate the tunability of the filter with a fine-tuning capability

for each resonator, the use of an adaptable varactor model is necessary. Since model extraction of a single component is typically valid for either one specific frequency, or a small range of frequencies, there exist many different models for varactors. A study is done on the validity of two existing varactor models for X-band frequencies in comparison to the measured data of the SMV1405-240 varactor.

3.2.1.2 Existing Varactor Models

According to S. and R. Hollos [18], there are two different models for varactors, a low and high frequency model. The interest of the project steers the focus to the high frequency model, shown in Fig. 3.14, where L_s and C_p represent the parasitic effects of the packaging, R_s the series resistance due to the semiconducting material as well as any contact or lead resistance, R_p the leakage resistance and C_d the capacitance of the depleted region.

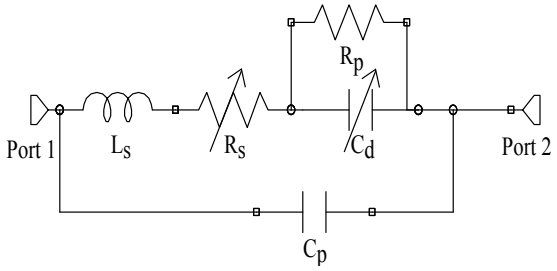

Fig. 3.14: *High-Frequency Varactor Model*

Skyworks Solutions presents a different model in [17], though the model also consists of combining an inductor, two capacitors and a resistor. The Skyworks model is shown in Fig. 3.15, where L_p and C_p represent the parasitic effects of the packaging, and R_s the variable series resistance due to the semiconducting material. Notice that there is no leakage resistor as in the previous model. In this case the packaging capacitance C_p is in parallel with R_s and C_d, but not with the package inductance L_p.

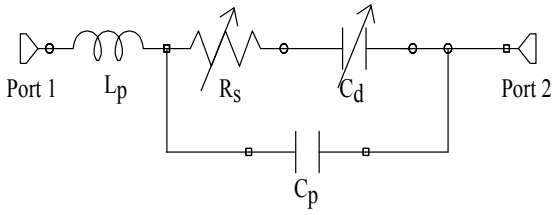

Fig. 3.15: *Skyworks Varactor Model*

The models from Fig. 3.14 and 3.15 are optimised to best fit the measurements, and compared to the calibrated measured S-paramenters in Fig. 3.17. The combination of element values that result in the best fit for all three the biasing stages (0 V, 10 V and 30 V) is presented in each case. Therefore, the total deviation from the measurement for all three biasing stages is minimised. In order to fit the models to the measurements, additional shunt capacitors were required at each port to take into account the effects of soldering.

The component values for the Hollos and Hollos circuit are: $L_s = 0.92$ nH, $C_p = 0.12$ pF, $R_p = 100\ \Omega$, the shunt capacitors are 0.205 pF each, the series resistance is tuned from 2 to 0 Ω and the diode capacitance C_d from 8 to 1.17 pF as the voltage increased.

The values for the Skyworks model are: $L_p = 1.92$ nH, $C_p = 1$ aF, the shunt capacitors are 0.205 pF each, the series resistance is tuned from 3.17 to 1.25 Ω and the diode capacitance C_d from 4 to 0.46 pF as the voltage increased.

Though both models have good correlation with the calibrated measurements, the Skyworks model is slightly better in this case. To see if the correlation can be improved and a relationship between the capacitance and biasing voltage can be established, a new model is proposed.

3.2.1.3 Proposed Varactor Model

The proposed varactor model is presented in Fig. 3.16. The proposed model also includes the additional shunt capacitors (C_p) that model the effects of soldering which cannot be cancelled in the TRL calibration process. Soldering is also necessary in the planar filter and so including the effects ensures more accurate modelling. In comparison to the Skyworks model, the proposed model excludes the parallel capacitor for the package capacitance due to its small value. From the calibrated measured results it is known that the tunable diode capacitance, C_d, is such that it forms a resonator with the inductance. The inductance from the Skyworks model is used as a starting point.

Once again the model was altered until the best fit was obtained across all three biasing voltages. The values for the proposed circuit are: $L_p = 2.28$ nH, $C_p = 0.205$ pF. The resistance is changed from 2.2 Ω to 1 Ω and the diode capacitance from 3.04 pF to 0.33 pF as the voltage is increased.

A relationship between the voltage and the capacitance is desired so that a single diode model can be incorporated into the simulation, and the biasing voltages readily tuned from 0 to 30 V. Since, the diode capacitance is related to the inductance as follows,

$$C_d = \frac{1}{\omega_0^2 L_p} \tag{3.2.1}$$

where ω_0 is the self-resonance frequency of the varactor, and the inductance remains the same across the tuning range, the biasing voltage can be related to the resonant frequency. This relationship is extracted by mapping a best-fit line to the calibrated measured results using MATLAB, resulting in eq. 3.2.2.

$$f_0(GHz) = \ln(1.5V_b) + 2 \tag{3.2.2}$$

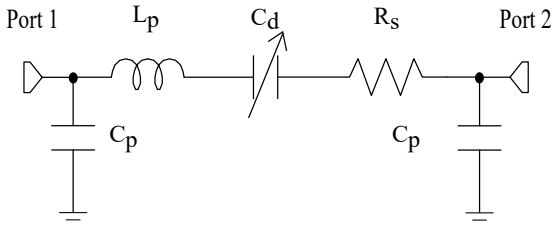

Fig. 3.16: *Varactor Model*

A comparison between the varactor calibrated measurements, the model by Hollos and Hollos, the proposed varactor model, and the Skyworks model is shown in Fig. 3.17. It is clear that for the various biasing voltages, the proposed model has a better continuous agreement with the calibrated measurements. It is important to note that two capacitors, similar to the C_p capacitors in the extracted model, were added to the Hollos and Skyworks

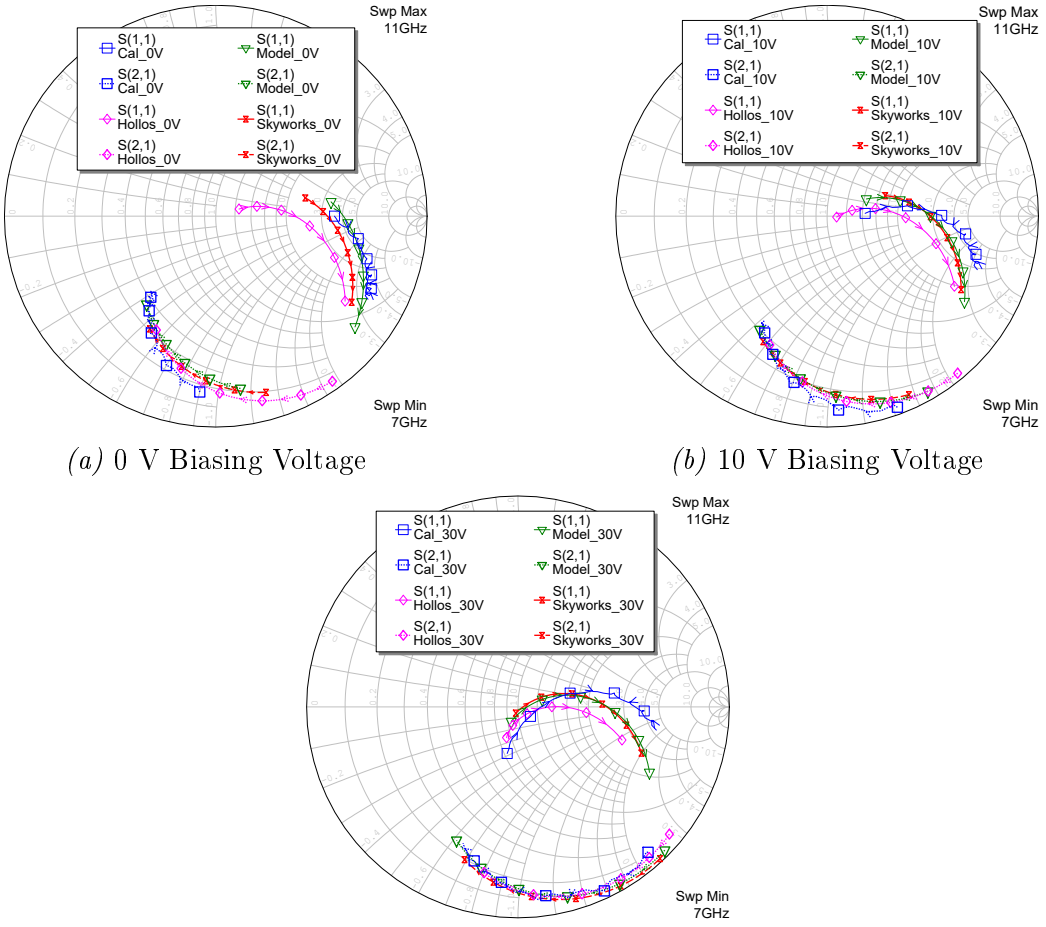

(a) 0 V Biasing Voltage

(b) 10 V Biasing Voltage

(c) 30 V Biasing Voltage

Fig. 3.17: *Correlation between the Calibrated SMV1405 Measurements and Three Possible Models*

models to improve the correlation with the measurements. The proposed model also allows easy incorporation and tuning since the same model can be used for all tuning stages by adjusting the biasing voltage. Thus, the extracted varactor model, as shown in Fig. 3.16, is used in the simulation of the planar prototype filter.

3.2.2 Conclusion

This chapter discusses basic coupled resonator filter theory, the effects of centre frequency tunability on the filter response, and a modelling technique for improved simulation accuracy. The key aspects in this chapter are all required to successfully design both the planar and waveguide filters proposed in this dissertation. Coupled resonator theory is a powerful design tool as the equations are valid for any type of resonator, which allows two entirely different types of filters to be designed from the same prototype. From the discussion on the effects that tunability has on the filter response, several conclusions can be drawn for the behaviour of both the planar and waveguide filter. For example, in both filters the bandwidth is expected to decrease as the frequency is tuned down, and vice versa. The model extraction method proposed in this chapter can be applied to any surface-mount component. Some of the main advantages of modelling a tuning component in this way include the reduction of simulation time, the option of continuous tuning in simulation, and the ease of incorporation in 3-D full-wave electromagnetic simulations.

Chapter 4

Tunable Planar Filter Design

Miniaturisation, low cost and manufacturability are three of the most important requirements for mobile communication systems and CubeSat applications. Planar structures are advantageous when considering cost, size and ease of incorporation for tuning components. Though planar structures have more power dissipation associated with the structure itself in comparison to waveguide for example, the effect thereof on the filter response may be minimised in the design process. In this chapter a varactor-tuned planar filter is presented, where the incorporation of the varactors is simplified by using a microstrip structure and surface-mount components. To minimise the dielectric loss associated with the microstrip structure, the substrate is suspended.

Many state-of-the-art tunable filters are of low order and difficult to expand to higher orders. Section 4.1 presents a study in which classical planar topologies are evaluated for centre frequency tunability and manufacturability while having useful orders. The study focuses on narrow-band filters for use in X-band, therefore coupled-line topologies are investigated. Two methods for the comparison of the tunability of coupled-line topologies are included in the study. The four most popular coupled-line filter topologies, which are presented and studied here, are the staircase, hairpin, interdigital, and combline topologies. Section 4.1 presents the design of each of these coupled-line filter topologies, and a description of the study methods and their results.

The outcome of the tunability study is used as the starting point for the design of a planar tunable filter prototype. Section 4.2 presents a novel biasing structure for planar staircase filters, with electrical decoupling achieved through spatial placement and orientation of the biasing lines as shown in Fig. 4.16. Each half-wave resonator is terminated at both ends with identical varactor diodes (shown in Fig. 4.20), which can then be controlled with a single bias line. As the symmetry of the electric field magnitude is not disturbed by such a placement of the tuning elements, a point of zero voltage exists on the line. At this point, the vertically directed electric field is also zero, and a vertically orientated biasing line can be introduced without influencing the filter characteristics. For symmetrically loaded half-wave resonators such as used in for instance staircase filters, the zero-voltage point on each resonator is stationary under changes in centre frequency, which is a significant advantage for tunable filters. The biasing structure is also non-resonant, which allows for good out-of-band performance. The proposed structure is illustrated by a 5^{th} order X-band suspended substrate staircase filter. Using a varactor at each open end of each resonator, and the spatially decoupled bias feed, a measured centre frequency tunability of 400 MHz is achieved around a nominal frequency of 11.9 GHz. This work has been reported in [13].

4.1 Tunable Classical Coupled-Line Bandpass Filter Topologies

This section builds on the work presented in [40] and presents a more accurate study on the tunability of popular coupled-line filter topologies. The study considers a Chebychev prototype designed using the theory in Ch. 3 and transforms it into circuit models for commonly-used coupled-line planar filter topologies, namely the staircase, interdigital, hairpin, and combline topologies. The filters are designed for X-band frequencies centred at 10 GHz, with a 5 % 3-dB bandwidth, and are modelled using ideally coupled transmission lines in AWR Microwave Office. The study is focused on centre frequency tunability, changes in bandwidth and out-of-band attenuation, and the practical implementation of tuning components. It is shown that in comparison with others, the classical staircase topology offers the best balance between good centre frequency tunability and out-of-band attenuation while utilizing realisable tuning component values.

4.1.1 Capacitively-Loaded Transmission Line Resonators

Since all four of the topologies under investigation are based on the same fundamental transmission line theory, a simplified example for the effect of a tunable capacitive element on the above mentioned topologies is presented in this section.

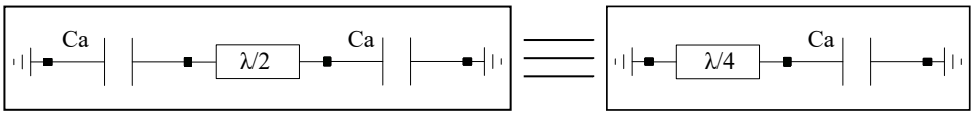

Fig. 4.1: *Loaded Open-Circuited Resonator Equivalent Circuits*

Though the staircase and hairpin topologies are based on open-circuited transmission lines, and the interdigital and combline topologies use short-circuited transmission lines, the lengths of the staircase and hairpin transmission lines are such that a point of zero electric field exists in the centre of the half-wavelength line. Therefore, a doubly end-loaded half-wavelength line may be modelled as a singly end-loaded shorted quarter-wavelength line, as shown in Fig. 4.1.

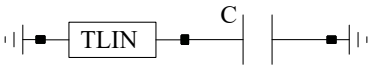

Fig. 4.2: *Capacitively-Loaded Short-Circuited Resonator*

From transmission line theory, a short-circuited line's input admittance (Y_{sc}) is given by,

$$Y_{sc} = \frac{-jY_0}{\tan(\frac{2\pi\ell}{\lambda})} \tag{4.1.1}$$

Terminating the short-circuited line in a single capacitor (C), as shown in Fig. 4.2, results in an input admittance (Y_{in}) of,

$$Y_{in} = Y_{sc} + j\omega C \tag{4.1.2}$$

At resonance the susceptance is zero, therefore the resonant frequency for given transmission line lengths (ℓ) and capacitances (C) can be calculated using the following equation,

$$f_0 = \frac{Y_0}{2\pi C \tan(\frac{2\pi\ell}{\lambda})} \tag{4.1.3}$$

For a given line length of $\ell = \lambda/n$, where n is a real positive number, the resonant frequency becomes,

$$f_0 = \frac{Y_0}{2\pi C \tan(\frac{2\pi}{n})} \tag{4.1.4}$$

Adding a capacitive tuning element (C_a) in parallel with the load capacitor (C), as shown in Fig. 4.3, changes the resonant frequency.

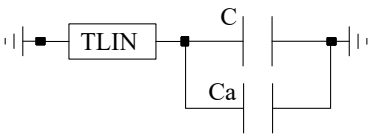

Fig. 4.3: *A Tuning Capacitor added to the Capacitively-Loaded Short-Circuited Resonator*

The new resonant frequency is given by

$$f_0 = \frac{Y_0}{2\pi(C + C_a) \tan(\frac{2\pi}{n})} \tag{4.1.5}$$

for a given line length of $\ell = \lambda/n$, where n is a real positive number. For the short-circuited loaded line to be inductive, the value of n should be less than $\lambda/4$. The resonant frequency as a function of the capacitances C and C_a, is shown in Fig. 4.4.

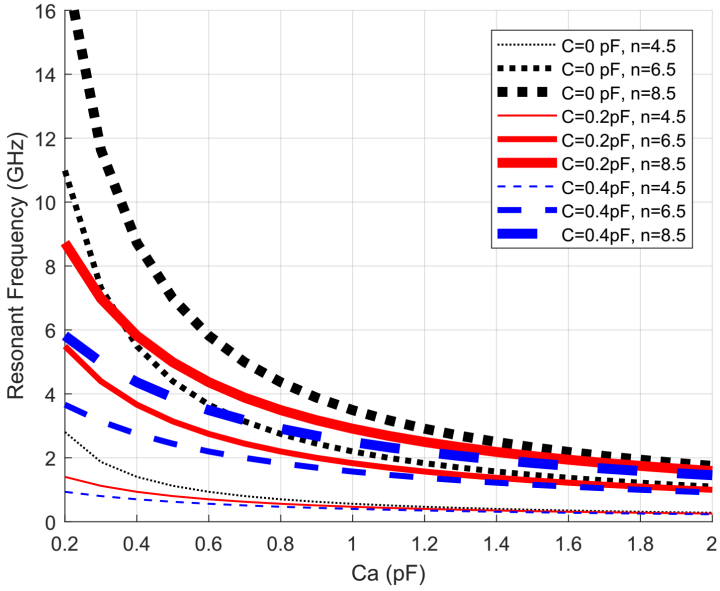

Fig. 4.4: *Short-Circuited Capacitively Loaded Resonator*

Where the load capacitance C is zero, the resonant frequency for a loaded open-circuited resonator is shown. The short-circuited line length varies from $\lambda/4.5$ to $\lambda/8.5$ where n has a step size of 2. For a resonant frequency of 1 GHz, the $n = 4.5$ line requires a $C = 0.2$ pF and $C_a = 0.4$ pF. If C_a is decreased by 0.2 pF, the resonant frequency changes to 1.5 GHz. For a $n = 6.5$ line, with $C = 0.4$ pF and $C_a = 2$ pF, $f_0 = 1$ GHz is obtained. Changing C_a for this line by 0.2 pF results in a frequency change of only 0.1 GHz. The plot shows that the smaller the load capacitance (C), the more sensitive the resonator is to changes in the tuning capacitance (C_a), for the same line lengths. The plot also shows that the resonant frequency is the most sensitive for small values of C_a for all cases.

4.1.2 Theory and Design-Approach for Each Filter Topology

In order to compare the different topologies it is essential that all are designed for the same specifications and originate from the same low-pass prototype. The element values for a ladder-type low-pass 5^{th} order Chebychev prototype filter with a normalized 3-dB cut-off frequency at $\Omega_c = 1$, are calculated using eq. 3.1.2 and yields

$$\begin{aligned} g_0 &= 1 = g_6 \\ g_1 &= 1.15 = g_5 \\ g_2 &= 1.37 = g_4 \\ g_3 &= 1.98 \end{aligned} \tag{4.1.6}$$

The prototype values are used in the design equations for each filter topology, as shown in [1] and [41]. All four topologies are designed and evaluated in AWR Design Environment using lossless transmission lines with specified even- and odd-mode impedances, electrical lengths, and resonant frequencies. The design equations and element values for each topology follows. The values are calculated by hand using the design equations below, and tuned in AWR to provide a 5 % 3-dB fractional bandwidth instead of an equi-ripple bandwidth of 5 %. This choice of bandwidth is based on the original design specifications for the planar filter. Both designed and tuned values are given.

Staircase Filter

The following design equations presented in [41] are used to calculate the inverter parameters for the staircase topology:

$$\begin{aligned} J_{(0,1)} &= Y_0\sqrt{\frac{\Delta\pi}{2g_1g_0}} \\ J_{(j,j+1)} &= \frac{Y_0\Delta\pi}{2\sqrt{g_jg_{j+1}}} \\ J_{(N,N+1)} &= Y_0\sqrt{\frac{\Delta\pi}{2g_Ng_{N+1}}} \end{aligned} \tag{4.1.7}$$

where $j = 1$ to $N - 1$ and

- N is the order of the filter

- $\Delta = \frac{\omega_2 - \omega_1}{\omega_0}$
- Y_0 is the source and load admittance (0.02 mhos).

Table 4.1 presents the calculated and tuned coupled-line input values for the even- and odd-mode impedances for the staircase filter. The calculated values result from the following equations [41]:

$$\begin{aligned} Z_{0e_{i,i+1}} &= \frac{1}{Y_0} + \frac{J_{i,i+1}}{Y_0^2} + \frac{J_{i,i+1}^2}{Y_0^3} \\ Z_{0o_{i,i+1}} &= \frac{1}{Y_0} - \frac{J_{i,i+1}}{Y_0^2} + \frac{J_{i,i+1}^2}{Y_0^3} \end{aligned} \tag{4.1.8}$$

for $i = 0, .., N$.

Table 4.1 Staircase Tunability Study Element Values

Parameter	Designed	Tuned
$Z_{0e_{0,1}}$	66.48	66.48
$Z_{0o_{0,1}}$	40.35	40.47
$Z_{0e_{1,2}}$	53.32	53.00
$Z_{0o_{1,2}}$	40.35	47.28
$Z_{0e_{2,3}}$	52.50	52.33
$Z_{0o_{2,3}}$	47.73	48.10

Hairpin Filter

For the hairpin filter, the staircase filter design values calculated above are used as a starting point. Transmission line bends are inserted and tuned to a length of 30^o to prevent coupling between sections on the same line. The electrical lengths of the straight line sections are tuned to 75^o each, forming a 180^o, or $\lambda/2$ line length with the bended section. The length of the bends are chosen for spacious separation and good coupling between resonators. The tuned parameters together with the staircase design parameters are presented in Table 4.2

Table 4.2 Hairpin Tunability Study Element Values

Parameter	Designed	Tuned
$Z_{0e_{0,1}}$	66.48	67.00
$Z_{0o_{0,1}}$	40.35	40.66
$Z_{0e_{1,2}}$	53.32	53.12
$Z_{0o_{1,2}}$	40.35	47.28
$Z_{0e_{2,3}}$	52.50	52.47
$Z_{0o_{2,3}}$	47.73	48.09

Combline Filter

The design equations for a tapped-line combline filter presented in [42] are used as a starting point for the coupled-input combline design.

$$\begin{aligned} b &= \frac{Y_{a1}}{2}\left[\frac{\theta_0}{\sin^2(\theta_0)} + \cot(\theta_0)\right] \\ J_{(j,j+1)} &= \frac{\Delta b}{\sqrt{g_j g_{j+1}}} \\ Y_{(j,j+1)} &= J_{(j,j+1)}\tan(\theta_0) \\ \Phi_0 &= \sin^{-1}\sqrt{\frac{Y_{a1}\Delta(\cos(\theta_0)\sin(\theta_0)+\theta_0)}{2g_0 g_1 Y_A}} \\ C_{1^s} &= Y_{a1}\cot(\theta_0)/\omega_0 = C_{N^s} = C_{j^s} \end{aligned} \tag{4.1.9}$$

where $j = 1$ to $N-1$, and

- N is the order of the filter
- $\Delta = \frac{\omega_2 - \omega_1}{\omega_0}$
- Y_A is the source and load admittance (0.02 mhos)
- Y_{a1} is the resonator admittance (0.013 mhos for all)
- b is the resonator susceptance slope parameter
- θ_0 is the electrical length at resonance
- Φ_0 is the tap position
- C_{1^s} is the load capacitance.

Table 4.3 presents the calculated tapped-line input (TI) and the tuned coupled-line input (CL) values for the even- and odd-mode impedances of the combline filter, calculated using eq. 4.1.10.

$$\begin{aligned} Z_{0e_{1,2}} &= \frac{1}{Y_{a1} - Y_{1,2}} \\ Z_{0o_{1,2}} &= \frac{1}{Y_{a1} + Y_{1,2}} \\ Z_{0e_{i,i+1}} &= \frac{1}{2Y_{a1} - Y_{0e_{i-1,i}} - Y_{i,i+1} - Y_{i-1,i}} \\ Z_{0o_{i,i+1}} &= \frac{1}{2Y_{i,i+1} - Y_{0e_{i,i+1}}} \end{aligned} \tag{4.1.10}$$

for $i = 2, .., N-2$, where Y_{a1} is the line admittance for the input resonator.

Table 4.3 Combline Tunability Study Element Values

Parameter	Designed TI	Tuned CL
$Z_{0e_{0,1}}$	N/A	56.60
$Z_{0o_{0,1}}$	N/A	102.6
$Z_{0e_{1,2}}$	69.99	69.69
$Z_{0o_{1,2}}$	85.38	85.58
$Z_{0e_{2,3}}$	72.52	71.32
$Z_{0o_{2,3}}$	83.20	84.00

Interdigital filter

The design equations for a tapped-line interdigital filter presented in [42], are shown in eq. 4.1.11. Since a coupled input is required for DC decoupled resonators, the equations below are used as a starting point and tuned for the coupled-input design.

$$\begin{aligned}
\theta_1 &= \frac{\pi}{2}\left(1 - \frac{\Delta}{2}\right) \\
h &= \frac{Y_r}{\tan(\theta_1)} \\
J_{(j,j+1)} &= \frac{h}{\sqrt{g_j g_{j+1}}} \\
Y_{(j,j+1)} &= J_{(j,j+1)} \sin(\theta_1) \\
\Phi_0 &= \frac{\sin^{-1}\left(\sqrt{\frac{h\sin^2(\theta_1)}{g_0 g_1 Y_A}}\right)}{(1 - \frac{\Delta}{2})}
\end{aligned} \tag{4.1.11}$$

- N is the order of the filter
- $\Delta = \frac{\omega_2 - \omega_1}{\omega_0}$
- Y_A is the source and load admittance
- Y_r is the resonator admittance
- θ_1 is the scaling factor and electrical length at the lower edge of the passband
- θ_0 is the electrical length at resonance
- h is the prototype's internal impedance level
- Φ_0 is the tap position

For a narrow bandwidth, the following approximations are valid:

$$\begin{aligned}
\tan\left(\frac{\pi}{4}\Delta\right) &\approx \frac{\pi}{4}\Delta \\
\sin(\theta_1) &\approx \sin(\theta_0) = 1
\end{aligned} \tag{4.1.12}$$

Table 4.4 presents the calculated tapped-line input (designed TI), and the tuned coupled-line input (tuned CL) values for the even and odd mode impedances, which are calculated using eq. 4.1.10.

Table 4.4 Interdigital Tunability Study Element Values

Parameter	Designed TI	Tuned CL
$Z_{0e_{0,1}}$	N/A	72.5
$Z_{0o_{0,1}}$	N/A	44.6
$Z_{0e_{1,2}}$	78.1	87.0
$Z_{0o_{1,2}}$	72.5	76.6
$Z_{0e_{2,3}}$	77.6	80.4
$Z_{0o_{2,3}}$	72.9	74.0

A Tunable Model for Each Filter Topology

As it is typical to add capacitive tuning elements to achieve centre frequency tunability in filters, lossless capacitors are added to the open-ends of each topology's resonators in order to evaluate its tunability.

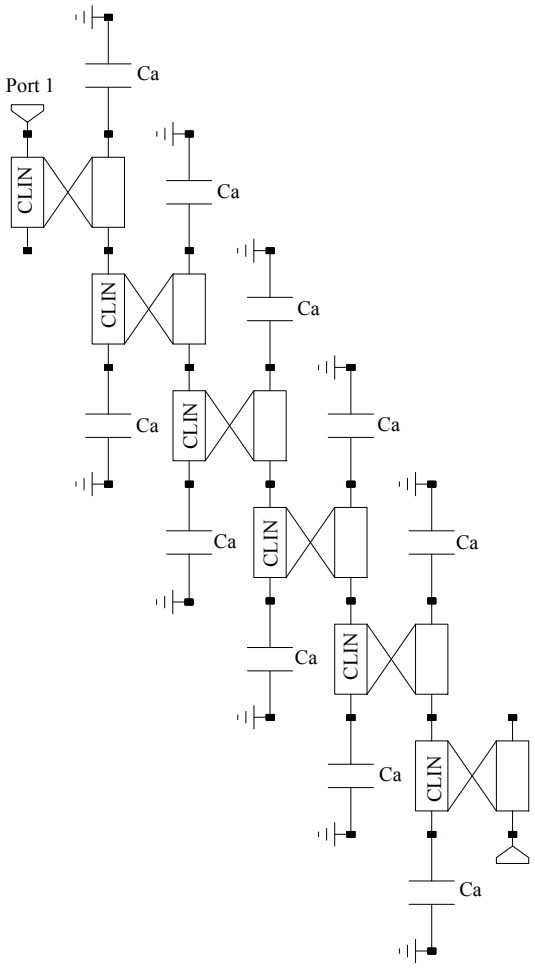

Fig. 4.5: *Tunable Staircase Topology*

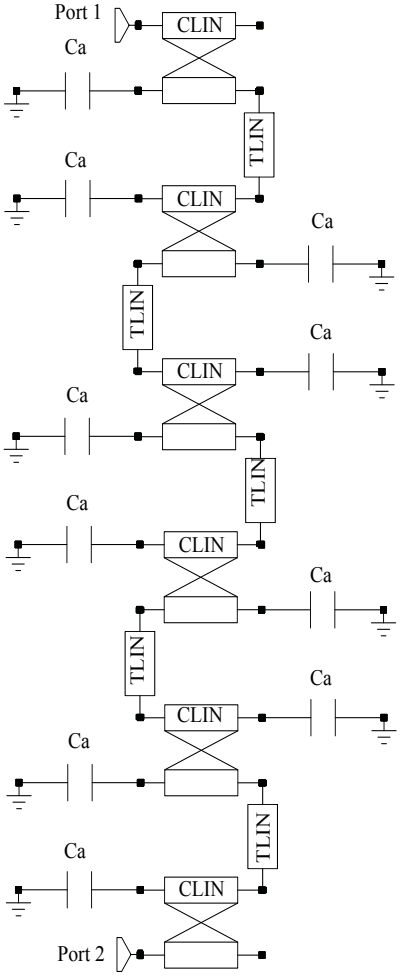

Fig. 4.6: *Tunable Hairpin Topology*

Figure 4.5 shows the staircase topology design with added variable capacitors labelled as C_a. Similarly, the hairpin, interdigital, and combline topologies are presented in Figs. 4.6 to 4.8. The combline topology requires a capacitance C for resonance and so the variable capacitor is placed in parallel with this capacitance to give a total capacitive value of $C + C_a$. The electrical length of the lines at 10 GHz for the combline topology

is recommended between 45 and 90 degrees. A length of 55 degrees is chosen to ensure that the capacitance value is realistic for a surface mount component. The value of C is thus 0.227 pF, which is the loaded capacitance necessary to form the combline filter.

Though it is possible to use open-circuited feed-lines for the interdigital filter, the short-circuited lines are mostly used as they result in better spacing between the input/output coupled sections. With open-circuited feed lines, a sharper roll-off can be realised due to the addition of transmission zeros.

It is important to note that the interdigital and combline filter structures permit only a single capacitor to be added per resonator due to only one open line end. In contrast, it is possible to add two capacitors per resonator to the staircase and hairpin filter topologies, since the resonators are doubly open-ended.

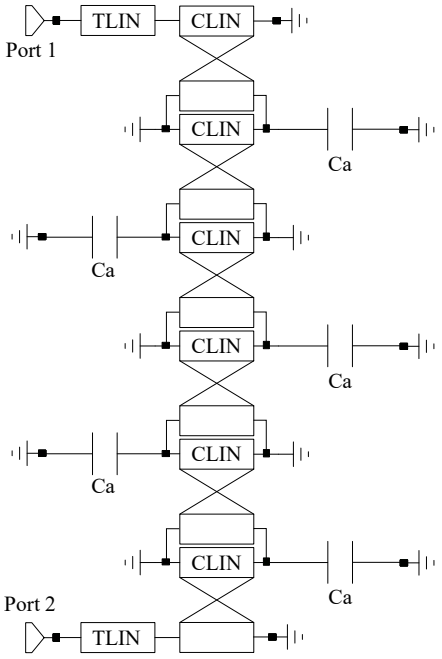

Fig. 4.7: *Tunable Interdigital Topology*

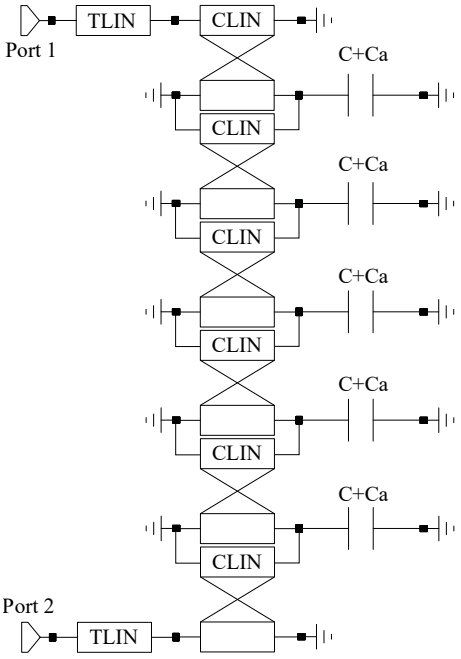

Fig. 4.8: *Tunable Combline Topology*

4.1.3 Topological Comparison

The four topologies are compared with one another using the following methods:

- Method I: Adding capacitance and determining the change in the filter response
- Method II: Determining the capacitance that is required to tune the filter response from 10 GHz to 9 GHz

Method I:

A 0.02 pF lossless capacitor is added to the open end(s) of each resonator. This is done for all of the topologies while centre frequency shift and change in 3-dB absolute bandwidth is observed. The insertion loss before and after the addition of the capacitance is plotted for each topology, as shown in Figs. 4.9 to 4.12. Table 4.5 summarises the observations from Method I and specifies the centre frequency tunability for each topology after a set

component with a capacitance of 0.02 pF is added where possible.

Table 4.5 A Summary of Method I

Topology	Initial f_0 (GHz)	Tuned f_0 (GHz)	Shift (MHz)	Δ 3-dB BW (%)	Attenuation at 1.05 f_0 (dB)
Staircase	9.997	9.611	386	4.24	40.08
Hairpin	9.997	9.610	387	5.22	40.59
Interdigital	9.997	9.695	302	3.3	38.28
Combline	9.997	9.777	220	0.54	43.51

Table 4.5 displays the initial centre frequency, the centre frequency after the addition of the tuning capacitance, the centre frequency shift, the change in 3-dB bandwidth from 0.05, and the attenuation at 1.05 times the centre frequency.

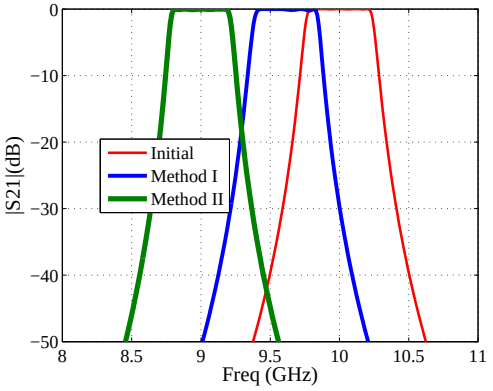

Fig. 4.9: *Staircase Filter Response*

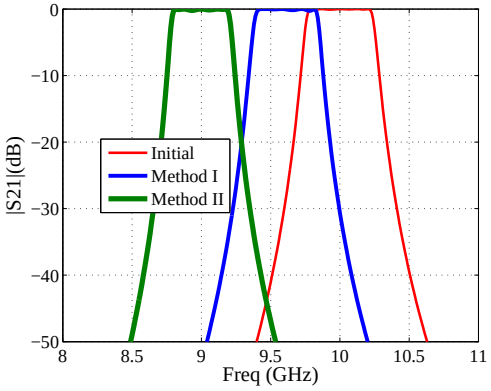

Fig. 4.10: *Hairpin Filter Response*

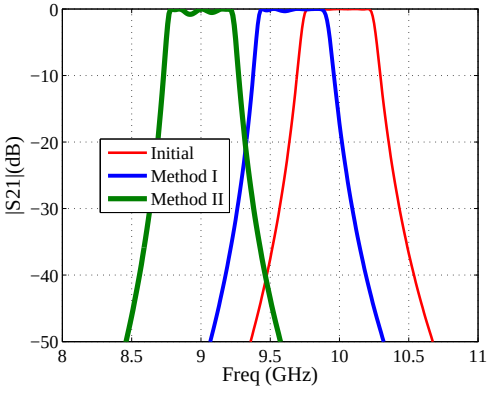

Fig. 4.11: *Interdigital Filter Response*

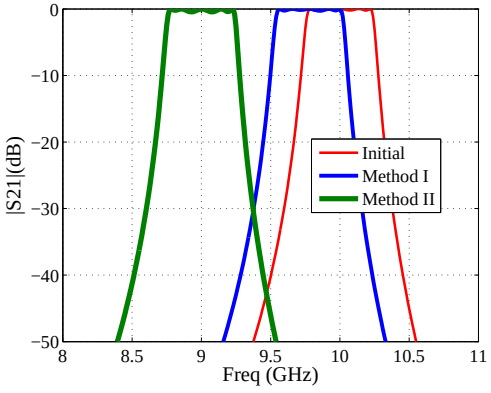

Fig. 4.12: *Combline Filter Response*

The hairpin topology, with two 0.02 pF capacitors added to each resonator, has the same centre frequency shift and attenuation at $1.05f_0$ as that of the staircase topology. The combline filter displays the largest attenuation but the lowest shift. Though the interdigital filter has a similar shift of 302 MHz and its bandwidth stability is the second

best, its out-of-band attenuation is the least. This can be attributed to the shorted input/output lines and the change in bandwidth when tuning.

The staircase filter runs on par with the hairpin in terms of shift and attenuation, which is not at all strange since these two filters follow similar design equations and procedures, and both have open-circuited doubly loaded resonators. However, the bandwidth is maintained slightly better in the staircase design. This is due to 90^o coupling sections between resonators in the case of the staircase filter in comparison to the 75^o sections of the hairpin filter.

In terms of absolute bandwidth, the combline filter maintains its relative bandwidth the best, while the hairpin and staircase filters have the largest change in absolute bandwidth. The large change in absolute bandwidth is due to the coupling mechanisms in these topologies. The combline's coupling is accurately modelled as an inductive Π-network, resulting in almost completely frequency invariable coupling factors. The staircase, hairpin and interdigital filters all have electric and magnetic coupling, resulting in frequency dependent coupling factors.

The interdigital filter shifts further than that of the combline filter but less than the hairpin and staircase filters. Given the theory presented for the capacitively-loaded short-circuited line in Sec. 4.1.1, it was expected that a larger sensitivity to changes in tuning capacitances (C_a) occurs when smaller loaded capacitances (C) are required. The difference in shift is thus attributed to the interdigital filter having no loaded capacitances in parallel with the tuning capacitances, while the combline has $C = 0.227$ pF.

Method II:

For this method, the capacitance C_a is optimized in AWR to provide a filter response centred at 9 GHz while the bandwidth and roll-off are kept as constant as possible. The comparison between the original and shifted response is shown in Figs. 4.9 to 4.12. The capacitance values required to tune each filter response down to 9 GHz is presented in Table 4.6. It is important to remember that coupling does not tune linearly with centre frequency and the best possible response is often obtained by tuning the capacitance values for each resonator separately. The capacitance value given in the table is the maximum required capacitance for any of the single elements, but it is not necessarily the value for all the capacitive tuning elements in the circuit.

Table 4.6 A Summary of Method II

Topology	Initial f_0 (GHz)	Tuned f_0 (GHz)	Δ BW (%)	Max Required C_a (pF)
Staircase	10	9	10.65	0.056
Hairpin	10	9	13.13	0.056
Interdigital	10	9	10.54	0.082
Combline	10	9	0.82	0.103

As expected, a larger capacitance value is required to tune the combline and interdigital filters down to 9 GHz than what is necessary for the staircase and hairpin filters, as shown in Table 4.6. Once again the combline filter maintains its relative bandwidth the best out of all the topologies. It is important to note that the coupling in a combline filter can be very accurately modelled using an inverter consisting of inductors. Referring back to Eq. 3.1.23, frequency independent coupling is probable for the combline filter topology.

Though the staircase and hairpin filters are similar in terms of performance, the staircase filter's bandwidth performance is slightly better in this case.

4.1.4 Biasing Methods for Classical Planar Topologies

Two of the most important requirements to ensure stable filter performance, are to limit the RF signal leakage towards the DC control circuit and to minimise the impact of the biasing structure on the filter response. The biasing for classical planar filter topologies often include etched or milled biasing lines with decoupling circuit components as seen in Sec. 2.2.1.

Figure 4.13 shows a biasing method for a combline structure presented in [43], where the biasing components include a capacitor at the open-end of the resonator and an inductor to the DC input. The inductor functions as an RF choke, while the capacitor decouples the DC input from the microstrip line to ensure that the varactor is not shorted.

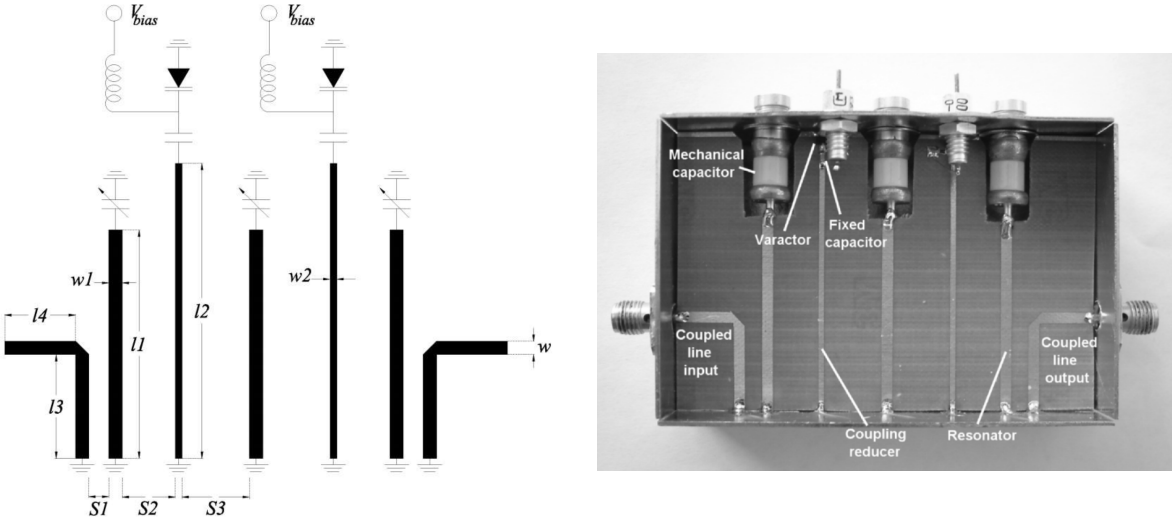

Fig. 4.13: *Biasing Method for a Tunable Combline Filter*

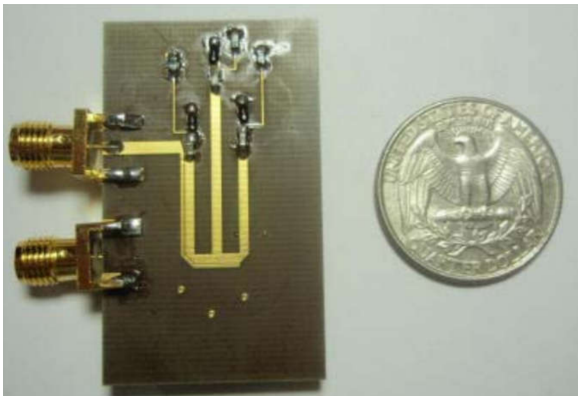

Fig. 4.14: *Biasing Method for a Tunable Hairpin Filter*

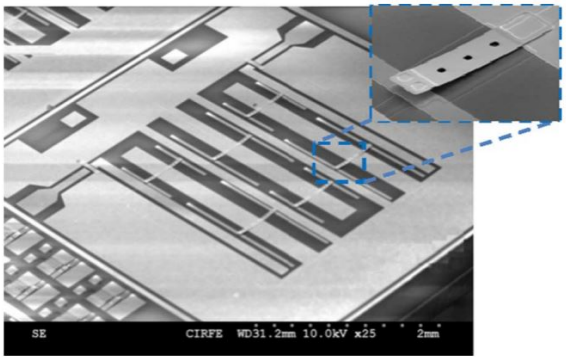

Fig. 4.15: *Biasing Method for a Tunable Interdigital Filter*

A similar biasing setup is seen in Fig. 4.14 for a hairpin structure presented in [44], where the biasing components also include a capacitor at the open-end of the resonator

and an inductor to the DC input. This hairpin filter incorporates two tuning elements for the resonator centre frequency and one for the open stub. The advantage of the stub is to improve the selectivity by adding a transmission zero. The advantage of incorporating the DC bias through etched lines, decoupling capacitors, and RF choke inductors, is that each varactor can be tuned separately. The biasing method might be simplified by utilizing the hairpin resonant line, but individual tuning of each element will be sacrificed.

Figure 4.15 shows a biasing method for a coplanar waveguide interdigital filter presented in [45], where DC biasing pads are added between the resonators and the ground sections. Though unclear, it is assumed that the only additional biasing circuitry included a wire to the DC pads.

4.1.5 Conclusion

A study on the tunability of classical coupled-line filter topologies was presented in this section. A staircase, hairpin, interdigital, and combline filter was designed using a 5^{th} order Chebychev filter prototype and the design equations in Sec. 4.1.2. The study consisted of two methods. Method I assumed that a given component with a capacitance value of 0.02 pF was available for tuning, which was added to the open ends of the resonating lines. Method II used loss-less capacitors to tune the centre frequency down by 1 GHz, and compare the maximum capacitance required for each topology to achieve this goal. Both methods were performed in AWR Design Environment using ideal transmission lines and loss-less capacitors. The study revealed that the staircase and hairpin topologies have the largest shift in centre frequency and require the smallest capacitance per component for a shift of 1 GHz, while the interdigital and combline topologies maintain their original bandwidth the best. In the case of the combline structure, frequency invariable coupling is almost achieved. The staircase topology performs slightly better than the hairpin topology when considering bandwidth change. Therefore, for a well-balanced design in terms of centre frequency tunability, out-of-band attenuation, change in relative bandwidth and manufacturability, the staircase filter is a good choice and is thus chosen as the topology for the tunable planar filter design.

4.2 Spatially Decoupled Varactor Biasing for a Tunable Staircase Filter

Even though combline filters are currently the most widely used topology for tunable planar filters, the study above shows that, if relative bandwidth is not of prime importance, the half-wave staircase has very useful tunability characteristics. In this section, it is furthermore shown that the E- and H-field distributions on half-wave resonators can be exploited very effectively to implement geometrically (i.e. not frequency dependent) decoupled biasing networks needing no additional biasing components. To illustrate this, a 5th order X-band prototype filter is designed with a tunable centre frequency at 11.75 − 12.15 GHz. To minimise loss, a suspended substrate staircase topology is used. The complete filter with housing, feed lines, and biasing networks is shown in Fig. 4.16.

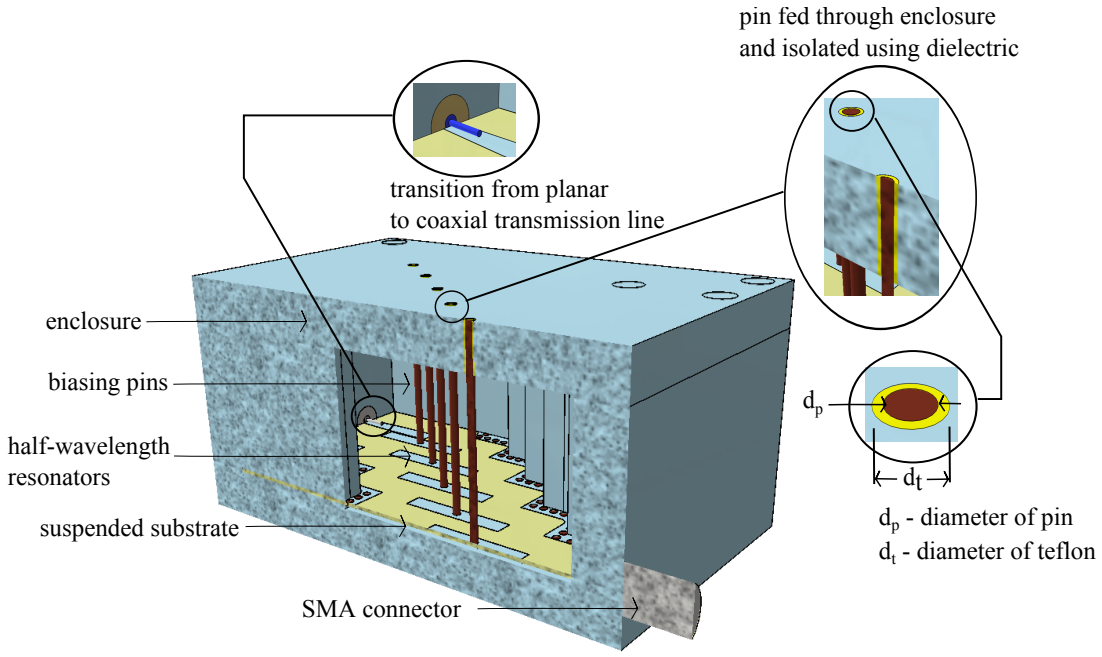

Fig. 4.16: *Cut-Plane View of the Biasing Structure for Planar Staircase Filters*

4.2.1 Spatially Decoupled Biasing of a Half-Wave Planar Resonator

The most important requirements for a tunable filter's biasing network are that the filter performance is not influenced, and that no RF energy leakage is caused by the biasing circuit. Any proposed network should therefore be evaluated in terms of these parameters.

From transmission line theory, the ideal electrical field distribution for a single, open-circuited, half-wavelength resonator on suspended substrate is depicted in Figs. 4.17a and 4.17c. Note that, for clarity, the top air layer is not shown. In the regions above and below the resonator, a null occurs in the electric field distribution on the longitudinal axis, at the exact centre of the resonator. This null extends vertically up and down from the centre of the resonator. A conducting bias pin of zero diameter, placed on this line from the roof of the enclosure to the surface of the resonator, as shown in the figure, will therefore not have any influence on the electric field.

The ideal magnetic field distribution on the structure is depicted in Figs. 4.17b and 4.17c. The magnetic field on the resonator shows an even longitudinal symmetry, and is transverse to the longitudinal direction. As the magnetic field of a vertical current-carrying pin will have an odd symmetry in the longitudinal resonator direction, equal amounts of positive and negative coupling will cancel out if the pin is placed vertically at the symmetry point at the centre of the resonator, resulting in zero net magnetic coupling. Placing a vertical pin at the centre of the structure therefore creates a bias pin which is *spatially decoupled* from the resonator electric and magnetic fields.

If a half-wave resonator is now symmetrically loaded with identical varactors at both ends (shown in Fig. 4.20), its resonant frequency can be controlled with a single bias line. As the symmetry of the electric field is not disturbed by such a placement of the tuning elements, a point of zero voltage exists on the line. At this plane, the electric field is also zero, and a vertically orientated biasing line can be introduced without influencing the filter characteristics. For symmetrically-loaded half-wave resonators, such as used in for instance staircase filters, the zero-voltage point on each resonator is stationary under

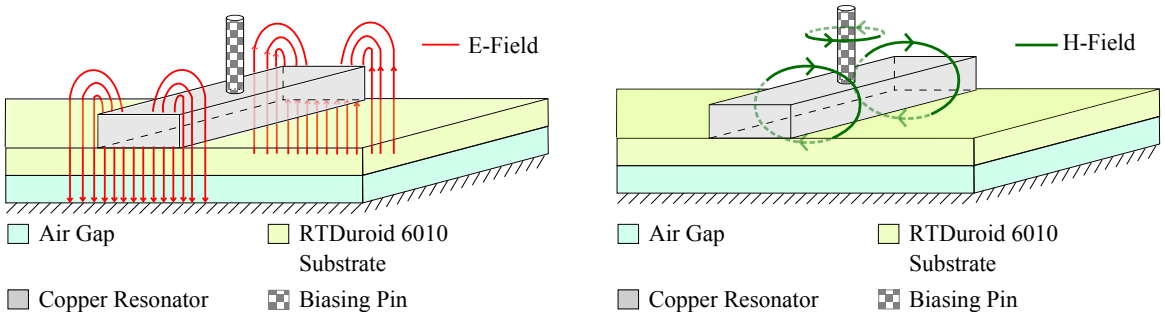

(a) Electric Field Distribution

(b) Magnetic Field Distribution

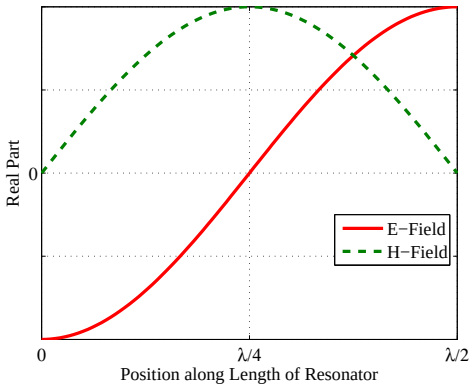

(c) Real Part of Electric and Magnetic Fields along the Length of an Ideal $\lambda/2$ Transmission Line Resonator

Fig. 4.17: *Electric and Magnetic Fields for an Ideal Open-Circuited Half-Wave Transmission Line Resonator on Suspended Substrate (ignoring field diffraction when moving between mediums of different permittivity)*

changes in centre frequency, which is a significant advantage for tunable filters. The biasing structure is also non-resonant, which allows for good out-of-band performance.

To investigate a practical implementation of such a biasing network, a suspended substrate structure is used. According to [41], dielectric loss may be reduced by utilising a very thin substrate with a low dielectric constant. The suspension of a substrate increases the quality factor of the resonators [41] and decreases the effective dielectric constant [46]. This means that a wider line is required for the same characteristic impedance in comparison to microstrip. A wider line enables easier incorporation of tuning elements and lowers conductor loss, but increases the total size of the structure. Therefore, a 0.25 mm thick Rogers RT/duroid 6010LM substrate, with 18μm copper cladding on both sides, is suspended 0.25 mm above the ground plane. The substrate has a low dissipation factor ($\tan\delta = 0.0023$) and a high dielectric constant ($\epsilon_r = 10.2$), making it ideal for miniaturisation and low-loss operation at X-band frequencies. The substrate thickness, suspension, loss tangent and permittivity was empirically determined for the best balance between size and loss reduction. The structure used here is the same as that used in the final planar filter design.

For practical bias pins of non-zero diameter, the pin volume must displace electric field even when positioned perfectly at the centre of the resonator, and will therefore have a measurable influence on the resonant frequency. As the magnetic decoupling is based on symmetry, pin thickness will not have a significant effect on performance as long as the pin is orientated perfectly vertical on the symmetry axis. To quantify the effects of a

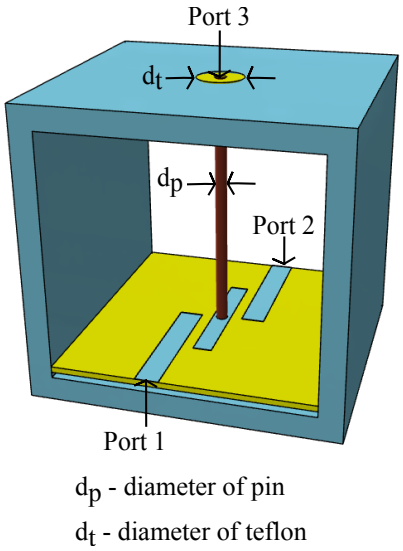

(a) Model for Simulating the Effects of the Biasing Pin Thickness (vertically upwards biasing pin)

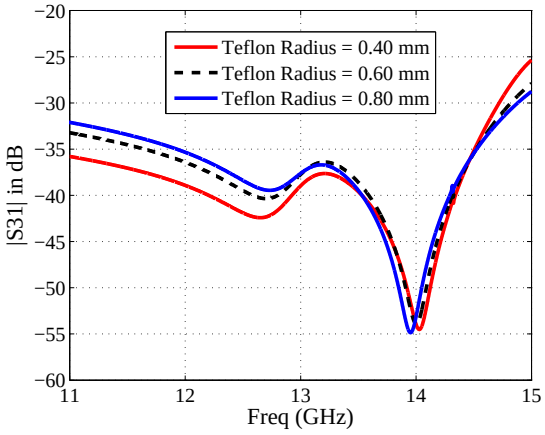

(b) Influence of Port 3 Dielectric Radius on Isolation for Pin to Roof

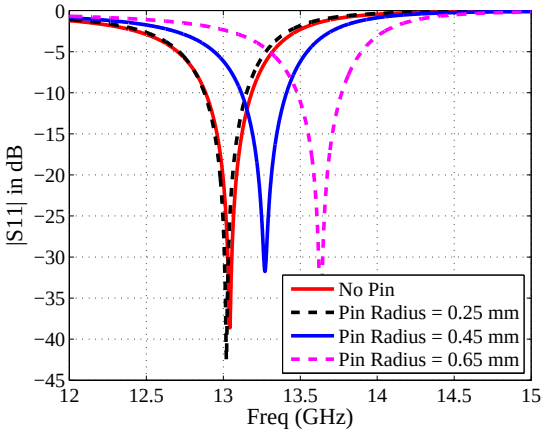

(c) Influence on Resonant Frequency for Pin to Roof

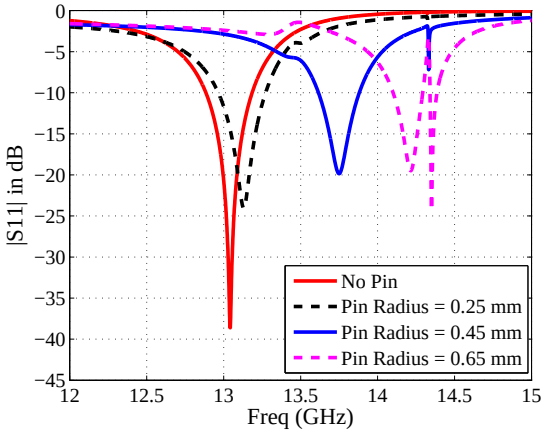

(d) Influence on Resonant Frequency for Pin to Floor

Fig. 4.18: *Simulated Effects of the Biasing Pin's Radius on the Reflection Coefficient for Two Biasing Configurations*

finite pin diameter, a resonator with a bias pin was coupled to input and output lines as shown in Fig. 4.18a, and the structure simulated in CST Microwave Studio.

For small couplings, such a simulation should show a resonant point in the reflection coefficient at the resonant frequency of the resonator. Figs. 4.18c and 4.18d respectively show the simulated reflection coefficient for different pin diameters for the case where the pin is placed between the roof of the enclosure and the resonator, and between the bottom of the enclosure and the resonator. It is clear that for a resonator with line length 7.2 mm and line width 1.2 mm, a pin radius of 0.25 mm or less has no measurable influence on the resonant frequency of the resonator when fed from the top. Feeding from the bottom clearly creates a much larger sensitivity to the pin diameter, and is also more difficult to implement in suspended substrate than in microstrip structures, where a via can be used.

In terms of leakage, for any energy which may couple to a finite biasing pin, the pin itself provides inductive properties and functions like an RF choke to reduce RF leakage

to the DC biasing and control circuitry. This effect is further enhanced by ensuring a high capacitance between the biasing pin and the roof of the enclosure at the pin exit point, in effect creating a low-pass LC-filter. To achieve this, the pin is fed through an aperture in the roof with a thin dielectric cylinder separating the pin and the enclosure, as shown in Fig. 4.18a.

Fig. 4.18b shows the effects of the pin-enclosure capacitance using a simulation of the same structure as before, but now with an extra coaxial port where the pin exits the enclosure. The pin therefore forms the centre conductor, and the enclosure the outer conductor of the coaxial port. The figure shows the transmission coefficient from the excitation port to this port, where any transmission indicates energy which leaks out of the enclosure due to the biasing pin. By varying the radius of the dielectric (teflon) cylinder between the pin and the enclosure, and keeping the pin radius constant at 0.25 mm, a set of curves representing leakage can be obtained, as shown in the figure. It is clear that even for fairly large exit holes, the leakage is still small.

Finally, the influence of the biasing on resonator Q is investigated using CST and the transmission-type Q-calculation [47]. A pin diameter of 0.5 mm is used in the same structure as before, and the metal is modelled as copper with a surface resistivity of 50% that of the ideal to allow for surface roughness [48]. Table 4.7 shows that the addition of the biasing pin has a negligible effect on the unloaded Q-factor of a single resonator, for a pin diameter of less than the width of the resonator, when placed at a point of zero RF voltage.

Table 4.7 Single Resonator Simulated Results

Structure	Resonator Unloaded Q factor
Resonator only	276.4
Resonator with Biasing Pin from Top	274.0
Resonator with Biasing Pin from Bottom	261.2

To validate the theory, a tunable single half-wave resonator circuit is manufactured and measured. For centre frequency tunability, two Skyworks SMV1405-240 varactors are soldered onto the resonator at right angles, one at each open-end. These varactors are specified by the manufacturer for applications up to 18 GHz, due to their low series resistance [49]. The reverse bias voltage limit for the SMV1405-240 varactor is 0 - 30 V, which provides a specified capacitance variation from 0.63 - 2.67 pF, inversely proportional to the biasing voltage. An insulated wire is used as the spatially decoupled vertical biasing pin which runs through a 0.7 mm diameter hole in the roof of the enclosure, straight down onto the centre of the resonator. The manufactured tunable single resonator circuit is shown in Fig. 4.19.

Table 4.8 summarises the measured results for the different cases of the single resonator structure. The table provides the resonator unloaded Q-factor as calculated from transmission measurements of the lightly coupled structure. From these results it is evident that the addition of the biasing pin has a negligible effect on the resonator's unloaded Q-factor. A significant decrease in the unloaded Q-factor is however observed after the addition of the varactors. This is due to the varactor series resistance which adds loss. It should be clear that this loss is by far the most important loss mechanism in tunable filters at these frequencies. For this resonator it is also clear that the total Q goes down as the varactor capacitance increases.

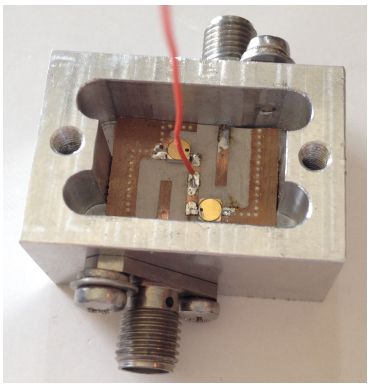

Fig. 4.19: *Manufactured Single Resonator Circuit with Vertical Biasing Pin and Varactors*

Table 4.8 Single Resonator Measured Results

Structure	Resonator Unloaded Q factor
Resonator only at f_0	230.15
Resonator with Biasing Pin at $1.03f_0$	231.48
Resonator with Two Varactors Biased at 0 V at $0.96f_0$	60.86
Resonator with Two Varactors Biased at 30 V at $1.01f_0$	80.51

It is clear that a biasing pin of small diameter, placed vertically from the centre of a half-wave planar resonator to the roof of an enclosure surrounding the resonator, with a large capacitance to the enclosure at the exit point, provides a decoupled biasing structure for a single resonator without the need for any other decoupling circuitry. It should also be clear that, when varactor diodes are added symmetrically to both ends of such a resonator the field symmetry of the magnetic field and the null in the electric field will be maintained at the same position of the line, enabling the use of the proposed biasing structure. Finally, if the varactors are used to change the centre frequency of the resonator, neither of these characteristics will change as they are both linked to the symmetry of the structure. This independence of frequency due to spatial considerations is a significant advantage of the proposed structure.

4.2.2 5th Order Tunable Planar Filter Prototype

Planar staircase filters have for many years been one of the more popular classical filter topologies. As they can be designed from a coupled resonator perspective using half-wave resonators, they are eminently suited to the biasing structure proposed here. To illustrate the biasing technique, a fifth order staircase filter with a 3-dB bandwidth of 500 MHz at a nominal centre frequency of 12 GHz, tunable from 11.75-12.25 GHz, is designed using a Chebychev low-pass prototype. To reduce loss, suspended substrate technology is used.

At these frequencies and for such a narrow bandwidth, stringent requirements hold for the tuning elements, especially low series resistance and inductance. In addition, the capacitance range must allow for the required tuning range. For the purposes of this prototype, the Skyworks SMV1405-240 varactor is again used as the tuning component. Because of the sensitivity of the filter to parasitics at high frequencies, accurate varactor models, as presented in Fig. 3.16, are used in the design cycle and line lengths are

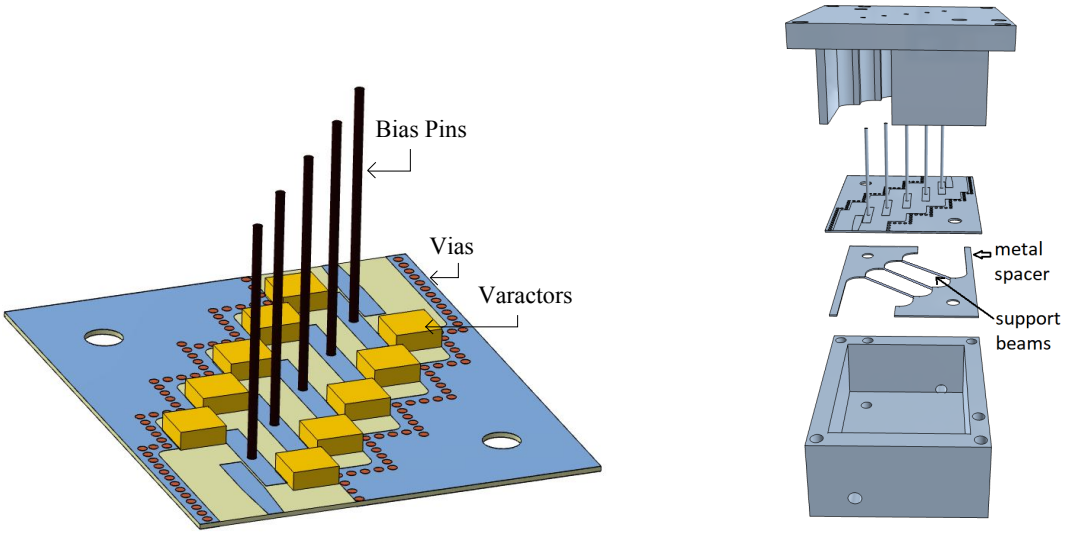

(a) 3D View of Designed Tunable Filter *(b)* Breakdown of Tunable Filter Structure

Fig. 4.20: *Tunable Filter Structure*

compensated to include the parasitic inductance and capacitance.

4.2.2.1 Design and Simulation of the Prototype

The planar staircase filter used in the tunability study serves as the starting point for this design. However, each capacitor is replaced with the extracted varactor model from Sec. 3.2.1 (Fig. 3.16) and the centre frequency is tuned to 12 GHz. The line lengths have to be altered further to compensate for the effects of the varactor model and to achieve the desired centre frequency. For the design process, simulations are performed using Agilent's Advanced Design System (ADS) and CST Microwave Studio. The ADS setup for the ideal coupled-lines with the varactor models, is depicted in Fig. 4.21. Through experimental results the shunt capacitance of the varactor model was determined to be 0.1 pF rather than 0.205 pF, due to changes in solder quantities. Table 4.9 shows the varactor model parameters as used in the ADS simulations.

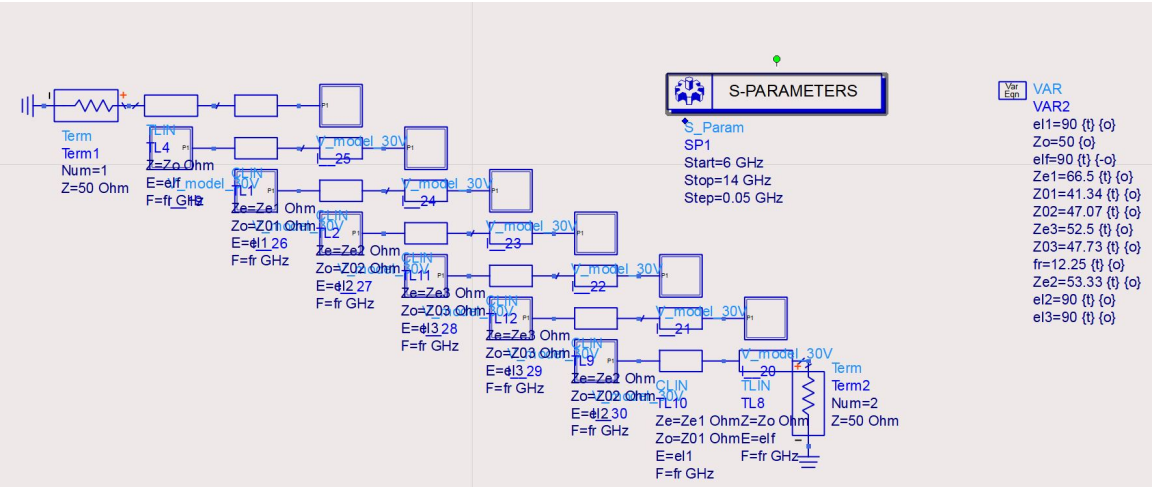

Fig. 4.21: *Ideal Coupled-Line Filter with Lossy Varactor Model*

Table 4.9 Varactor Model Parameters for Planar Filter Simulation

Parameter	Value
L_p	2.28 H
C_p	0.1 pF
C_d	0.33-3 pF
R_s	1-2.2 Ω

The simulated filter response for the ideal coupled-line circuit with lossy varactor models is shown in Fig. 4.22. The desired centre frequency tuning range of 500 MHz from 11.75 GHz to 12.25 GHz is displayed.

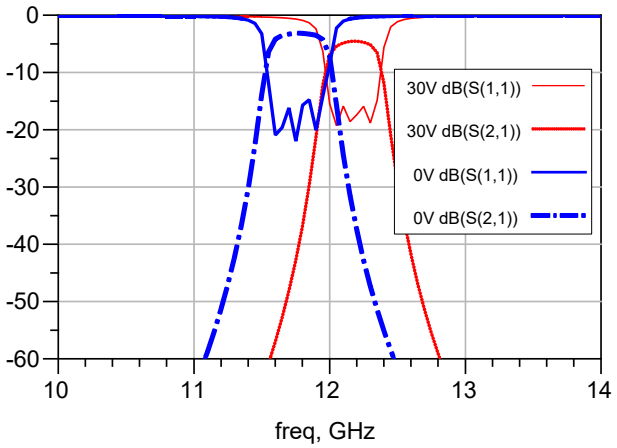

Fig. 4.22: *Circuit Simulation of the Ideal Coupled-Line Filter with Lossy Varactor Model*

From the ideal coupled-line circuit, a suspended substrate full wave EM model is created in both CST and ADS using the group delay method as described in [50]. The ADS and CST simulation setups are shown in Figs. 4.23 and 4.24, respectively.

The ADS and CST simulations consist of both full-wave electromagnetic and circuit simulations. These simulations include the effects of lossy dielectric substrates, conductive metals, the biasing wires, and the effects of transitioning from an SMA connector to a suspended substrate feed-line. The full wave simulation is used to create an EM model of the 3-D structure which excludes varactor models. Additional discrete ports are added at the open ends of the resonators in the 3-D layout, creating a multi-port EM simulation and model. Once the EM model is generated, it is added to a 2-D circuit simulator. The additional ports are used to connect the varactor models to the EM model. In addition to the varactor models, a negative inductance is also added to each port in order to compensate for the port inductance added by ADS and CST when a discrete port does not fall in a single mesh cell.

The ADS full-wave EM structure dimensions are given in Table 4.10 and correspond with the CST parameters. $Wres$ and $Wfeed$ are the widths of the resonators and feed lines, respectively. $Len1$, $Len2$ and $Len3$ correspond to the lengths of the first, second and third resonators. $Lfeed$ is the total length of the feed line, including a 3.3 mm tapered section. The parameters $Sep1$, $Sep2$ and $Sep3$ are the respective separations between the feed and the first resonator, resonator 1 and 2, and resonator 2 and 3. The filter is symmetrical about the third resonator.

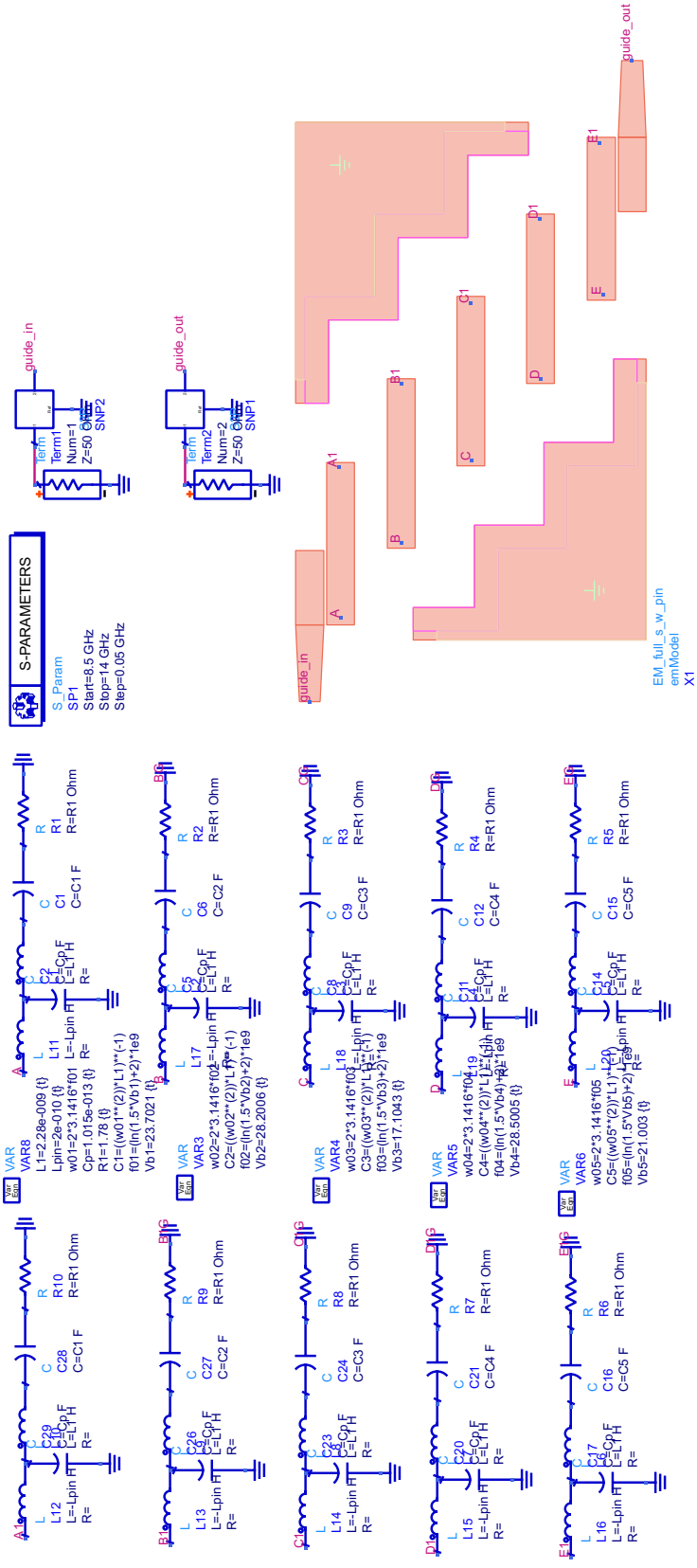

Fig. 4.23: *ADS Simulation Setup with Varactor Models*

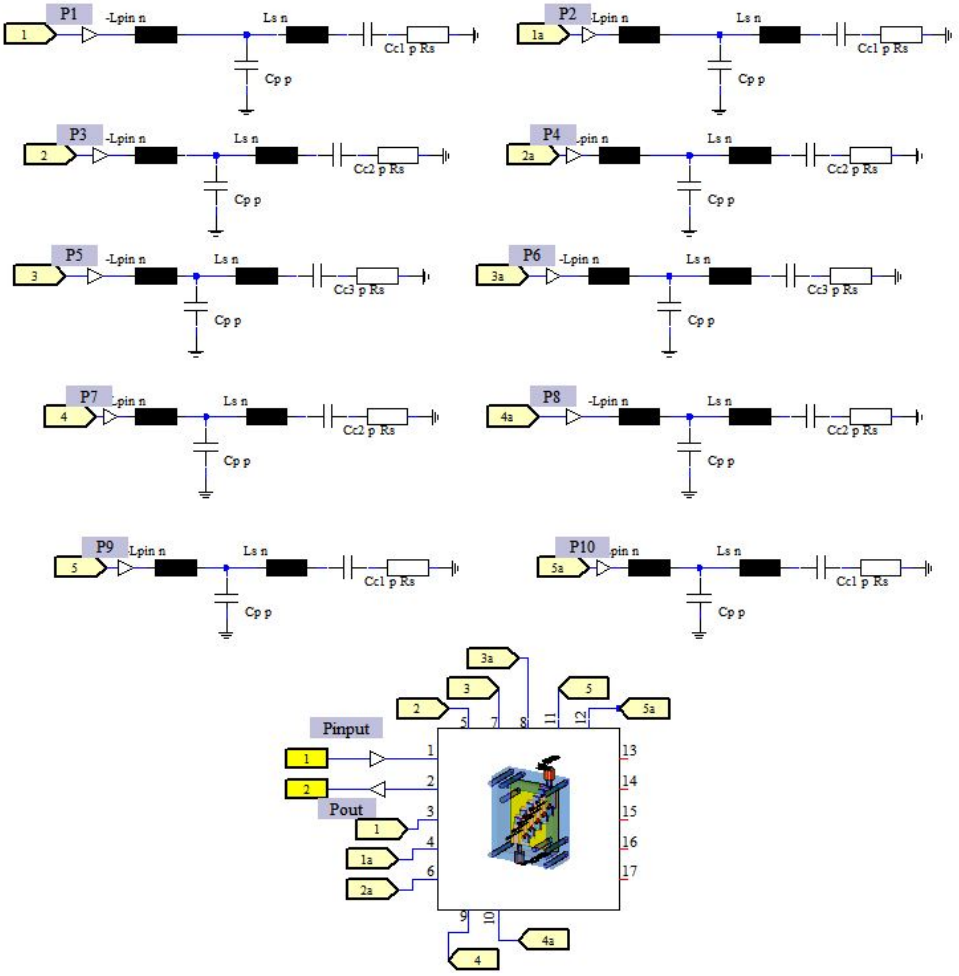

Fig. 4.24: *CST Simulation Setup with Varactor Models*

Table 4.10 ADS EM Simulated Parameters for Planar Filter

Parameter	Value
$Wres$	1.2 mm
$Wfeed$	0.9 mm
$Lfeed$	6.6 mm
$Len1$	6.9 mm
$Len2$	7.12 mm
$Len3$	7.12 mm
$Sep1$	0.125 mm
$Sep2$	1.42 mm
$Sep3$	1.80 mm

The filter structure, with the enclosure removed, is shown in Fig. 4.20a, and the exploded view of the full filter, with its enclosure, shown in Fig. 4.20b. The spatially decoupled vertical biasing pins run through the roof of the enclosure, through 0.7 mm diameter holes, straight down onto the centre of each resonator. To evaluate the effects of non-ideal pin diameters and leakage, coaxial ports are added to the biasing pins in the CST full wave simulation.

The exit point of each pin is numbered 3-7, with ports 1 and 2 the actual filter input

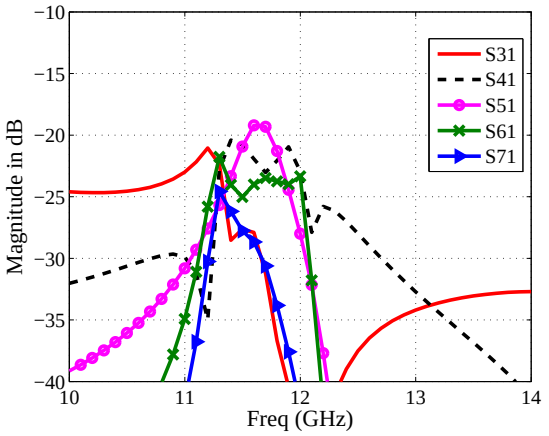

Fig. 4.25: *Simulated Isolation between Input Port and Biasing Pins (no varactors)*

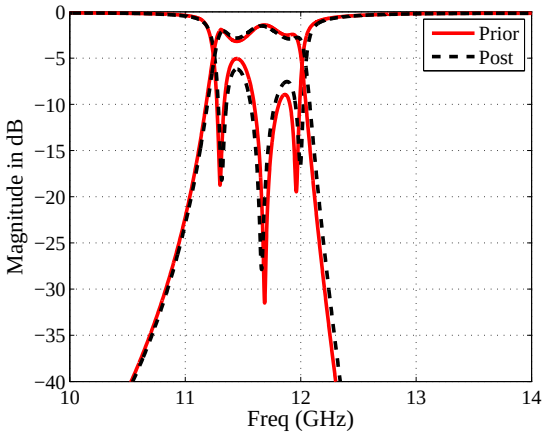

Fig. 4.26: *Simulated Effects of the Biasing Pins on the Filter Response (no varactors)*

and output ports. The simulated transmission coefficients from port 1 to ports 3-7 (i.e. the leakage) are shown in Fig. 4.25. It is seen that the isolation is greater than 18 dB for all biasing pins from 10 to 14 GHz. Note that this can be reduced even further by reducing the exit hole aperture, increasing the roof-pin capacitance. Fig. 4.26 shows the filter input reflection and transmission coefficients with and without biasing pins. It is clear that the influence of the biasing pins are minimal. Note that both these graphs exclude the varactor diodes.

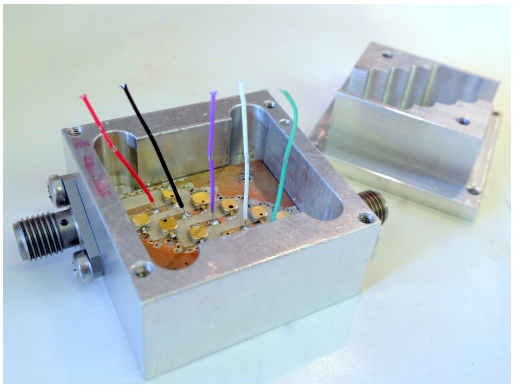

Fig. 4.27: *Manufactured Filter (biasing lines become vertical when fed through the roof of the enclosure)*

4.2.2.2 Measurements and Results

The filter is manufactured using the same substrate and suspension as described in the single resonator circuit. However, to improve manufacturing tolerances, the substrate is etched instead of milled. The varactors are placed at right angles to the resonator, at both open-ends of each resonator, as illustrated in Fig. 4.20a. To suppress higher order modes from resonating in the rectangular structure, stepped side walls are added as seen in Fig. 4.20b. Both varactors on a single resonator are controlled by the same biasing pin and voltage, with each resonator controlled by its own tuning voltage. Note the absence of any other biasing circuitry.

The manufactured filter, shown in Fig. 4.27, is measured using a PNA-X from Keysight Technologies. Each resonator is biased individually to tune the filter to a specific centre frequency. The input reflection and transmission coefficient measurements are shown in Fig. 4.28 and 4.29, respectively. For a clear stop-band visual, a wide frequency range is shown in conjunction with a detailed measurement over a smaller frequency range.

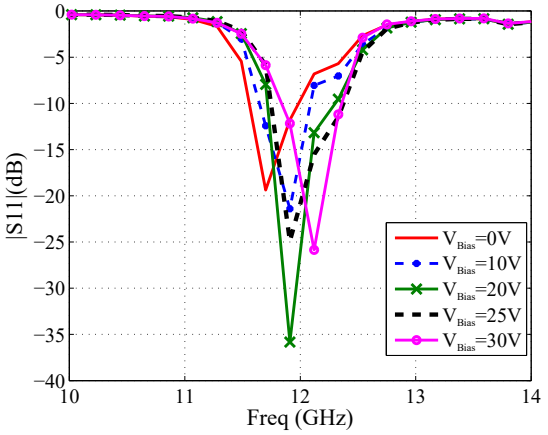

(a) Input Reflection Coefficient from 10-14 GHz

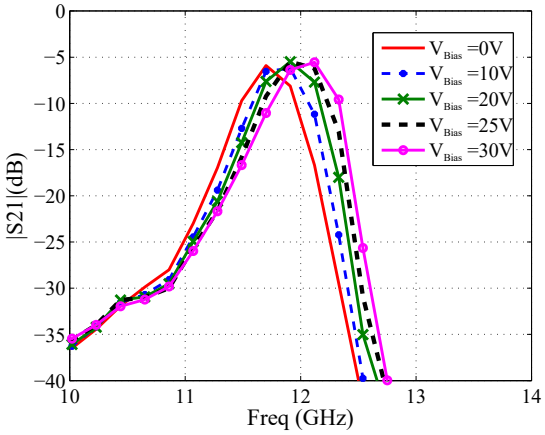

(a) Transmission Coefficient from 10-14 GHz

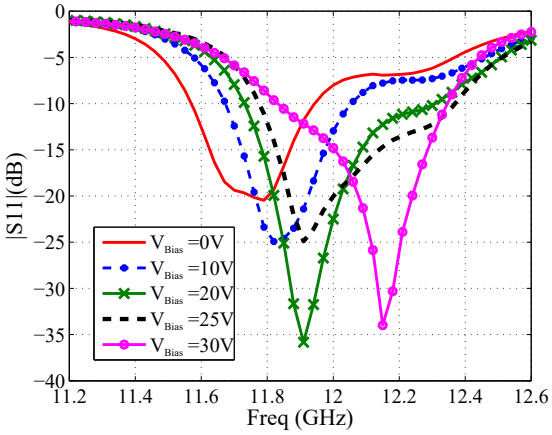

(b) Input Reflection Coefficient from 11.2-12.6 GHz

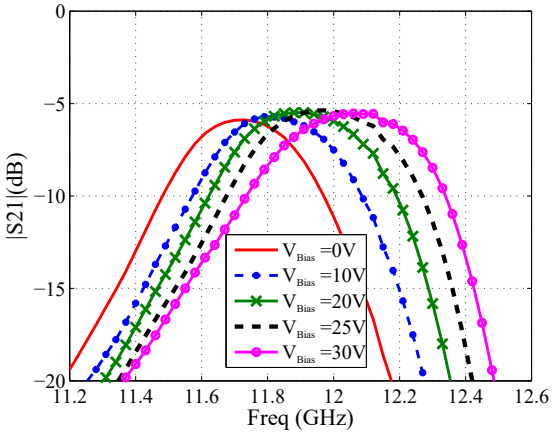

(b) Transmission Coefficient from 11.2-12.6 GHz

Fig. 4.28: *Input Reflection Coefficient Measurements*

Fig. 4.29: *Transmission Coefficient Measurements*

Fig. 4.30 shows a comparison between the simulated response, using a suspended substrate circuit model in ADS, and measured results. The original simulation parameters were tuned to compensate for manufacturing tolerances. Simulations performed on the filter suggest an expected tuning range of 500 MHz, from 11.75 GHz to 12.25 GHz. Measurements show a slightly reduced range of 11.75-12.15 GHz which can be attributed to differences in the capacitive values of the varactors. The significant difference between the out-of-band simulated and measured response for frequencies below the passband can be attributed to the waveguide cavity created by the enclosure. The approximated cut-off frequency for the TE_{10} mode in such a guide is around 9.0 GHz, which is visible in Fig. 4.30. Though the enclosure is included in the simulation, the physical parameters of the varactor diodes and the metal spacer support beams (see Fig. 4.20b) are not included,

which may cause additional energy to propagate through the guide in the lower passband. The asymmetry of the measured out-of-band response can be attributed to the stepped side walls of the enclosure, the support beams of the brass metal spacer, and the biasing pins. The pins and stepped side walls are equivalent to inductive posts in the guide, whereas the metal spacer support beams are capacitive posts. The combination of the walls, pins and beams create a bandpass filter within the guide. The spacing of these resonators are such that a passband is formed from 9 to 11 GHz with a transmission coefficient of between -30 and -40 dB.

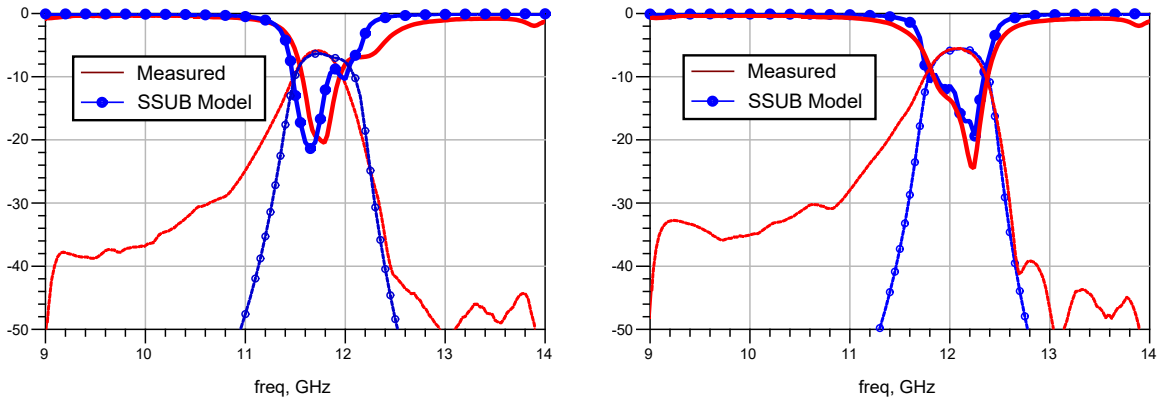

(a) 0 V Bias *(b)* 30 V Bias

Fig. 4.30: *Tunable Filter Simulated vs Measured Results*

The measurements show that the filter has an insertion loss of less than 6 dB and a return loss of greater than 20 dB at the centre frequency of each band. The return loss ranges from 6.2 - 14.4 dB at the edges of the 3-dB transmission band for the various tunings. It is important to note that the filter response is very sensitive to small increments in biasing voltage. Thus, it is possible to tune the filter more finely and improve the filter response shape at each frequency using sensitive biasing voltage control. As seen in Sec. 4.2.1, the varactors have a significant effect on the unloaded Q-factor of each resonator which also affects the 3-dB bandwidth. A better indication of the bandwidth change is therefore the 15-dB return loss bandwidth. This bandwidth varies from 2.04 - 2.60 % over the tuning range, compared to a 3.58 - 4.23 % variation for the 3-dB transmission bandwidth. Measurements of the filter without any varactors indicate that almost 4 dB loss in transmission can be attributed to the varactors. The 3-dB bandwidth reduces from the nominal 4.23 % at 12.15 GHz to 3.58 % at the low end.

Table 4.11 A Summary of the Measured Results

V_{bias} (V)	f_0 (GHz)	3-dB RBW (%)	3-dB ABW (MHz)	-15 dB RL RBW (%)	-15 dB RL ABW (MHz)
0	11.75	3.58	420	2.04	240
10	11.84	3.55	420	2.11	250
20	11.92	4.03	480	2.60	310
25	11.95	4.01	480	2.59	310
30	12.15	4.23	510	2.39	290

Table 4.11 summarises the measured results presented in Fig. 4.28 and 4.29, where f_0 is the centre frequency, ABW is the absolute bandwidth, RBW is the relative bandwidth, and RL is used as the abbreviation of return loss. Note that the point of minimum input reflection coefficient is used as the centre frequency and the 3-dB bandwidths are calculated from the transmission coefficient plot. The table shows that the 3-dB relative bandwidth increases by 18 % when the centre frequency is tuned from 11.75 to 12.15 GHz. To stabilize the bandwidth, compensation for changes in the coupling between resonators is necessary.

In comparison to the tunable planar resonator filters in [28, 12, 51, 52], the tunable filter presented here has the advantage of using the least amount of components per tuning element for the biasing structure. In comparison with the data presented in [53] on the performance of reported tunable filters, the filter presented here has a larger insertion loss and a wider bandwidth, but is similar in tuning range. It is important to note that the filters compared in [53] operate at a much lower frequency and thus the difference in insertion loss is to be expected. In comparison to [52], a very similar tuning range is achieved while the insertion loss differs slightly. It is evident that, while the proposed filter operates at a much higher frequency than the filters in [28, 51, 12], and is of a higher order than all of the filters compared in Table 4.12, the tuning range and insertion loss are competitive with these published works.

Table 4.12 Comparison with Recently Published Works

Filter	Tuning Frequencies (GHz)	Tuning Range (MHz)	Insertion Loss (dB)
[28]	0.766-1.228	400	5 - 7.3
[12]	1-1.4	400	3.5 - 3.8
[51]	4.25-4.4 and 6.25-6.4	150 for both bands	3.0 - 3.6
[52]	10.50-10.92	420	approx. 3
Presented	11.75-12.15	400	5.4-6.0

4.3 Conclusion

A novel biasing structure for planar staircase filters, with electrical decoupling achieved through spatial placement and orientation of the biasing lines, is presented in this chapter. The structure obviates the need for any decoupling circuit elements, by placing the biasing line at a point of zero RF voltage, on a line of minimum E-field, and symmetrically with respect to the magnetic field. For half-wave resonators, this point is stationary under changes in centre frequency, which is a significant advantage for tunable filters. The proposed structure is illustrated by a 5^{th} order planar staircase X-band filter with varactors at each open end of each resonator, each pair controlled by a single DC bias voltage applied through the spatially decoupled bias feed. The individual tuning capability of each resonator enables compensation for minor manufacturing errors and tolerances, as well as the ability to fine-tune the filter to a specific centre frequency. The biasing structure provides a good alternative for spatially constrained designs where it might not be possible to incorporate lumped components. The spatially decoupled placement and length of the biasing pins provide good isolation and minimal interference, thus eliminating the need for additional decoupling circuitry and minimizing the total size of the structure. The manufactured filter achieved a centre frequency tunability of 400 MHz

around a nominal frequency of 11.9 GHz. A maximum insertion loss of less than 6 dB and an input reflection coefficient of -15 dB or less across the tuning range was measured. The centre frequency tunability and the insertion loss is comparable to other planar filters as presented in Sec. 2.2.1.

In addition, a study on the centre frequency tunability of commonly-used coupled-line filter topologies was performed in Sec. 2.1. Staircase, hairpin, interdigital, and combline filters were designed using a 5^{th} order Chebychev filter prototype and the design equations in [1] and [41]. The study consists of two methods. Method I assumes that a given component with a capacitance value of 0-0.02 pF is available for tuning, which is added to the open ends of the resonating lines. Method II uses loss-less capacitance to tune the centre frequency down by 1 GHz and compare the amount of capacitance required for each topology to achieve this goal. Both methods were performed in AWR Design Environment using ideal transmission lines and loss-less capacitors of variable value C_a. From the four topologies that were investigated, the staircase and hairpin topology showed the largest shift in centre frequency in Method I and the least required capacitance in Method II. Compared to the hairpin filter, the staircase topology had better out-of-band attenuation and bandwidth maintenance. Thus, for a well-balanced design in terms of centre frequency tunability, bandwidth maintenance and out-of-band attenuation, the staircase filter is the better choice and so was used in the 5^{th} order planar filter design.

Chapter 5

Tunable Evanescent Mode Waveguide Filter Design

According to [54], the first published work on evanescent mode resonators was by Lebedev and Guttsait in 1956, but it was only 5 years later that this type of structure was suggested for use in microwave filters by W. A. Edison. In 1971, a design theory for evanescent mode waveguide bandpass filters was proposed by Craven and Mok [54]. The theory offered a viable solution to design evanescent mode waveguide filters with a specific filter response. The evanescent mode waveguide filters offer a compromise between the large size and excellent electrical properties of a standard waveguide, and the smaller but more lossy coaxial topologies. These filters utilize waveguide in a frequency range below the cut-off frequency of the fundamental mode, and are therefore significantly smaller than standard waveguides.

The inspiration for this chapter originated from the evanescent mode waveguide switch presented in [14]. In his dissertation Sickel shows that the evanescent mode waveguide switch, which incorporates in-waveguide mounted PIN diodes, operates as a filter in the off-state. Since PIN diodes are not suited to be used as variable capacitors at microwave frequencies, the filter proposed in this chapter investigates the expandability of Sickel's switch topology to a tunable evanescent mode filter using varactors.

Some of the main advantages of evanescent mode filters include their out of band performance, low loss structures, heat dissipation, and sensitivity to tuning components. Due to the below cut-off operation, good stop band characteristics can be achieved. In terms of tunability, evanescent mode filters offer interesting possibilities for construction, and excellent heat-dissipating properties. However, the passband performance is expected to deteriorate slightly faster in comparison to non-evanescent tunable filters since the coupling between resonators depend strongly on the characteristic reactance, the propagation constant and the physical length of the guide, which are all severely non-linear functions of frequency. This chapter encapsulates a broad overview of evanescent mode waveguide filter theory, a first and third order tunable filter design, of which both include the entire design process from synthesis to measurements.

5.0.1 Basic Evanescent Mode Waveguide Theory

Rectangular evanescent mode waveguides are used at frequencies below the cut-off frequency of the TE_{10} mode of the waveguide. For a rectangular waveguide, the modal cut-off frequencies can be calculated by using the following equation [55]:

$$(f_c)_{mn} = \frac{1}{2\pi\sqrt{\mu\epsilon}}\sqrt{\left(\frac{m\pi}{a}\right)^2 + \left(\frac{n\pi}{b}\right)^2} \tag{5.0.1}$$

where $m = 0, 1, 2, 3, ...$ and $n = 0, 1, 2, 3, ...$ Note that m and n cannot be zero simultaneously, and a and b are the width and height of the waveguide, respectively.

The transverse electric (TE) modes travelling in the positive z-direction are given in [55], and are shown to have an exponential component of $e^{-j\beta_z z}$, where β_z is the wave number. For modes at frequencies below cut-off, $f < f_c$, the wave number is given by,

$$(\beta_z)_{mn} = -j\omega\sqrt{\mu\epsilon} \times \sqrt{\left(\frac{(f_c)_{mn}}{f}\right)^2 - 1} = -j\gamma \tag{5.0.2}$$

for $m = 0, 1, 2, 3, ...$ and $n = 0, 1, 2, 3, ...,$ where m and n are not zero simultaneously [55]. This results in exponentially decaying fields. As the propagation is $e^{-j\beta_z z}$, attenuation increases as the mode number increases. It is clear that any higher order modes excited by a below cut-off TE_{10} mode would attenuate quickly. This gives rise to the fundamental postulate for filter design using an evanescent mode waveguide, which is that only the TE_{10} mode exists in the guide [54].

An evanescent mode waveguide can be modelled as a transmission line, as in Fig. 5.1. Applying the postulate and assuming the line is lossless, the characteristic impedance can be calculated as,

$$Z_0 = jX_0 = j\frac{120\pi b}{a\sqrt{\left(\frac{\lambda}{\lambda_c}\right)^2 - 1}} \tag{5.0.3}$$

for $\lambda = c/f$, the free space wavelength, and $\lambda_c = c/f_c$, the cut-off wavelength. It is clear that operating below the cut-off frequency results in an imaginary impedance, while operating above it results in a real impedance.

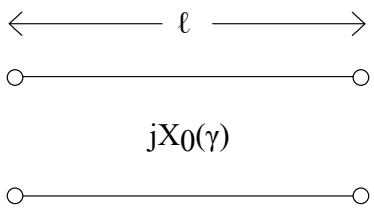

Fig. 5.1: *Evanescent Mode Waveguide Transmission Line Model*

The reactance can also be described in terms of the propagation constant as follows:

$$X_0 = \frac{240\pi^2 b}{a\gamma\lambda} \tag{5.0.4}$$

where,

$$\gamma = \frac{2\pi}{\lambda}\sqrt{\left(\frac{\lambda}{\lambda_c}\right)^2 - 1} \tag{5.0.5}$$

The Π-equivalent network for a piece of evanescent mode waveguide of length ℓ is given in Fig. 5.2. It should be noted that the element reactance is specified in this figure and not the inductance.

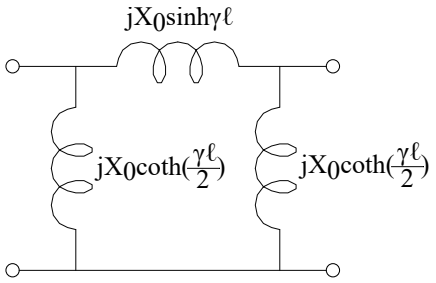

Fig. 5.2: *Evanescent Mode Waveguide* Π*-Equivalent Circuit*

Note that each reactance is a hyperbolic function of γ, with γ proportional to the root of the frequency. As the frequency approaches the cut-off all the reactances display severe non-linear behaviour. In order to form a resonator, two waveguide sections can be joined and a capacitive stub inserted, resulting in Fig. 5.3.

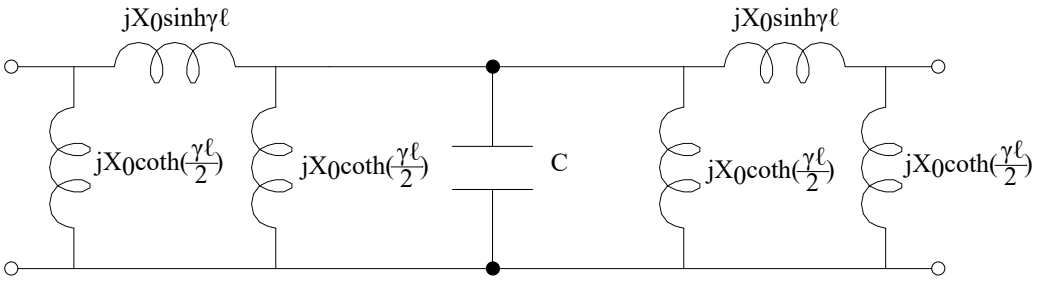

Fig. 5.3: *Two Identical Evanescent Mode Waveguide Sections with a Capacitive Stub*

A bandpass filter response can be created by altering the length of the guide and the shunt capacitance, such that the element values of the evanescent mode filter design equals that of the lumped element filter design in Sec. 3.1. This forms the basic principle of an evanescent mode filter.

5.1 First Order Tunable E-mode Filter

This section includes the theory, design steps, simulations, and measurements for a first order evanescent mode filter with a 10 % bandwidth and a centre frequency tunable from 10 - 11.5 GHz.

5.1.1 Theoretical Design

The design of a first order evanescent mode waveguide filter begins with the circuit in Fig. 5.3 and ends with a general coupled resonator filter circuit as shown in Fig. 3.7.

Impedance inverters can be created by splitting each shunt inductor into two, so that one of the inductors has a value negative that of the series inverter inductor, as shown in Fig. 5.4. The remaining inductor(B_{L1}) has a value of,

$$B_{L1} = X_0 \coth\left(\frac{\gamma\ell}{2}\right) + X_0 \sinh(\gamma\ell) = B_0 \coth(\gamma\ell) \tag{5.1.1}$$

where $B_0 = \frac{1}{X_0}$, the characteristic susceptance of the waveguide section. The central inductors are added to one another and the external inductors are absorbed into the

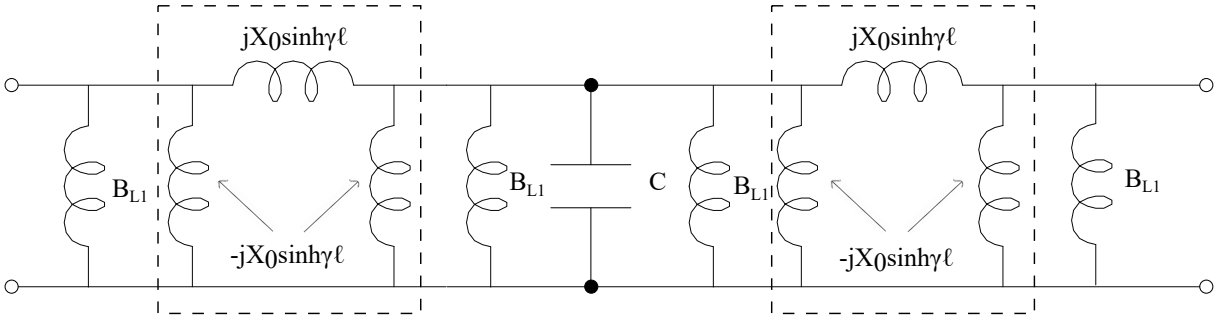

Fig. 5.4: *Creating Admittance Inverters by Splitting the Shunt Inductors*

terminating admittance. The terminating admittance includes the transition into the evanescent mode waveguide. This is explained in a later section. The circuit is scaled for an equivalent terminating admittance of Y_{eq}, which results in Fig. 5.5, where the subscript "e" for the parallel capacitor and inductor indicates "evanescent mode".

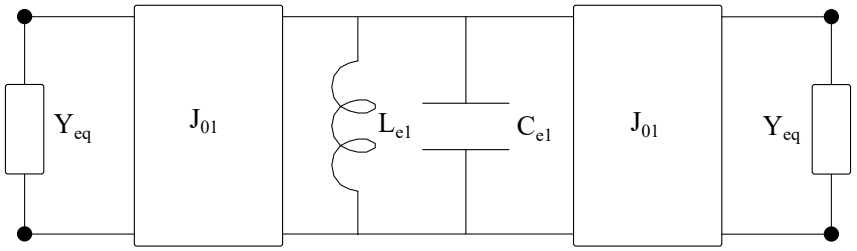

Fig. 5.5: *First Order Evanescent Mode Waveguide Filter Equivalent Circuit*

The element values for this circuit are given by,

$$\frac{1}{\omega_0 L_{e1}} = 2B_{L1}Y_{eq} = 2Y_{eq}B_0 coth(\gamma\ell) \tag{5.1.2}$$

and,

$$J_{01} = \frac{Y_{eq}}{X_0 sinh(\gamma\ell)} \tag{5.1.3}$$

Being of the same form as the circuit in Fig. 3.7, the element values in both circuits can be matched.

5.1.1.1 Matching the Circuit Element Values

An important factor to take into account when matching the element values of the two circuits, is the steeper reactance slope of the equivalent inductor in the evanescent mode circuit. A correction factor, Δ_{cm}, is added to the evanescent mode inductance to compensate for the difference in reactance slope, and is given by,

$$\Delta_{cm} = \frac{2}{1 + \frac{1}{1-\left(\frac{\lambda_c}{\lambda_0}\right)^2}} \tag{5.1.4}$$

As a reminder, the circuit element values for the first order coupled resonator filter design in Sec. 3.1, is as follows:

$$J_{01s} = Y_A\sqrt{\frac{G_0 C_1}{g_0 g_1}}$$
$$J_{12s} = Y_A\sqrt{\frac{G_2 C_1}{g_2 g_1}}$$
$$C_{s1} = Y_A\frac{C_1}{\omega_0\Delta}$$
$$L_{s1} = \frac{\Delta}{Y_A\omega_0 C_1}$$

where Y_A is the terminating admittance of the bandpass coupled resonator filter, and g_0, g_1, and g_2 are the low-pass prototype values. The low-pass capacitance selected by the designer is C_1. Therefore, matching the resonator's inductances from both the coupled resonator design and the evanescent mode circuit, results in,

$$\frac{1}{\Delta_{cm}\omega_0 L_{e1}} = \frac{2Y_{eq}B_0\coth(\gamma\ell)}{\Delta_{cm}} = \frac{Y_A C_1}{\Delta} \tag{5.1.5}$$

Matching the inverter values gives,

$$\frac{Y_{eq}}{X_0\sinh(\gamma\ell)} = Y_A\sqrt{\frac{G_0 C_1}{g_0 g_1}} \tag{5.1.6}$$

Setting Y_{eq} equal to Y_A results in two equations and two unknowns, C_1 and ℓ, which can easily be solved. It is therefore evident that the capacitance and waveguide length are strongly dependent on one another for a specific response.

5.1.1.2 Terminating the Evanescent Mode Waveguide Circuit

In practice, a waveguide which can propagate the TE_{10} mode at the desired operating frequency is required to feed the evanescent mode waveguide. For frequencies of 8-12 GHz a transition from an X-band guide to an evanescent mode waveguide, such as a K-band waveguide, is required. In Fig. 5.6 it is clear that the transition requires steps in both the electric and magnetic field planes.

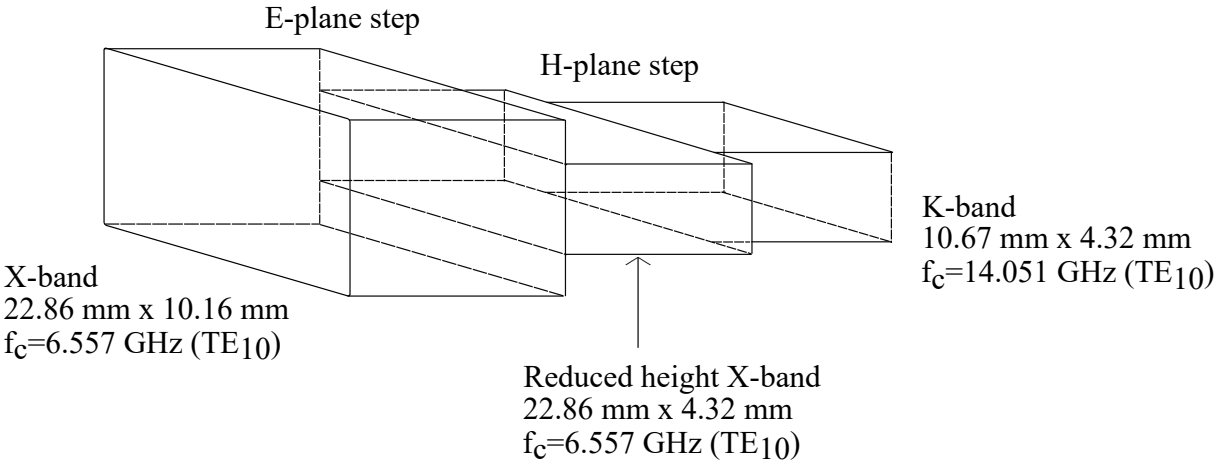

Fig. 5.6: *X-band to K-band Transition*

The reduced height X-band waveguide still has the same cut-off frequency for the TE_{10} mode as the standard X-band waveguide, and the step in height can be accurately modelled by a simple transformer with a turns ratio equal to the root of the ratio of the characteristic impedances of the guides. Therefore, only the H-plane step is discussed further. The equivalent model for an H-plane step is shown in Fig. 5.7.

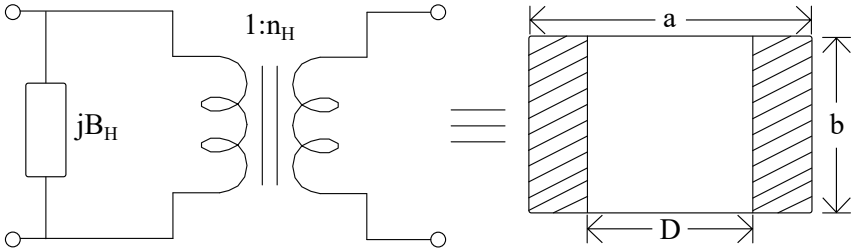

Fig. 5.7: *H-plane Step Equivalent Circuit*

The turns ratio and shunt susceptance are given in [54] as follows:

$$n_H \approx \sqrt{\frac{a}{D}} \frac{1 - \frac{D}{a}^2}{\frac{a}{\pi}\cos(\frac{\pi D}{2a})} \tag{5.1.7}$$

and

$$B_H \approx -\frac{\pi}{a\omega\mu}\cot^2\left(\frac{\pi D}{2a}\right) \tag{5.1.8}$$

The terminating admittance is shown in Fig. 5.8 and is equal to

$$Y_{eq} = \frac{1}{n_H^2}(Y_{0xr} + jB_H) + jB_{L1} \tag{5.1.9}$$

where Y_{0xr} is the characteristic admittance for the TE_{10} mode of the reduced height X-band waveguide.

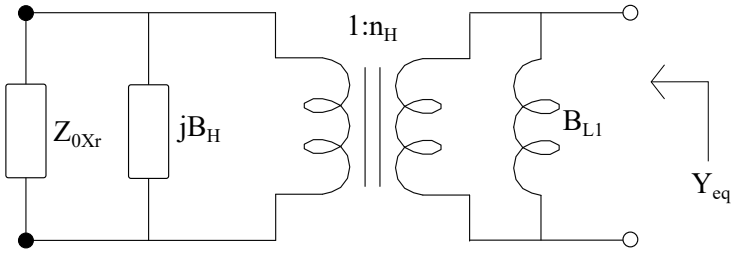

Fig. 5.8: *Equivalent Terminating Admittance*

5.1.2 Simulating the Design

The circuit parameters are calculated and the circuit in Fig. 5.9 is simulated and optimized using AWR Microwave Office. The component values are as follows:

$$
\begin{aligned}
\ell &= 6.98 \text{ mm} \\
Cc1 &= 0.2085 \text{ pF} \\
Z0x &= Z0_{Xr} = j\frac{\eta b_K}{a\sqrt{(\frac{\lambda}{\lambda_{cx}})^2 - 1}} \\
Lp &= \frac{X_0 \tanh(\gamma\ell)}{\omega} * 10^9 \text{ nH} \\
L1 &= \frac{2X_0}{\omega_0 \coth(\gamma\ell)} * 10^9 \text{ nH} \\
Li1 &= \frac{X_0 \sinh(\gamma\ell)}{\omega} * 10^9 \text{ nH}
\end{aligned}
\tag{5.1.10}
$$

where b_K is the height of the K-band guide, a is the width of the X-band guide, D is the width of the K-band guide, and λ_{cx} is the cut-off wavelength of the X-band guide.

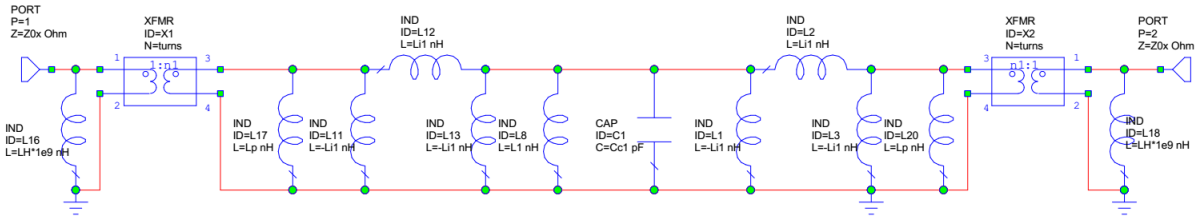

Fig. 5.9: *AWR Model of First Order Evanescent Mode Waveguide Filter*

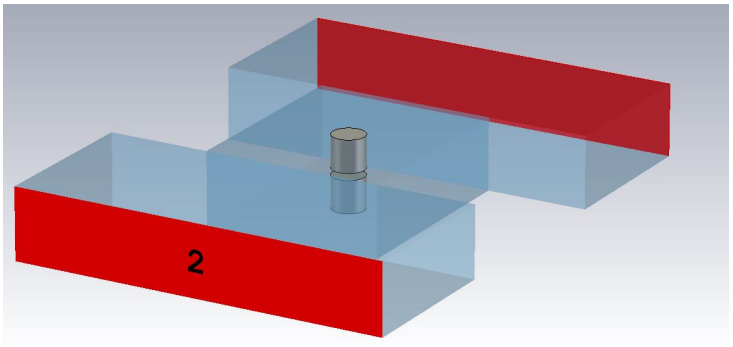

Fig. 5.10: *CST Model for First Order Evanescent Mode Waveguide Filter*

For a basic 3-dimensional realisation of the filter, CST Microwave Studio is used. The 3-D model consists of two tuning screw stubs separated by a gap and so creating a capacitive perturbation, as shown in Fig. 5.10. The waveguide line section lengths are slightly shortened to 5.875 mm in CST in order to compensate for the perturbation. The difference in the line lengths when compared to the AWR calculated lengths is exactly equal to the radius of the capacitive stub which is 1.1 mm. The gap between the two tuning screws is 0.472 mm. A parallel plate capacitor with a radius of 1.1 mm and a gap of 0.472 mm has an approximate capacitance of $C = \frac{\epsilon A}{d} = 0.071$ pF. Therefore, the additional 0.2014 pF is a result of the perturbing posts. A comparison between the AWR and CST simulated responses is presented in Fig. 5.11.

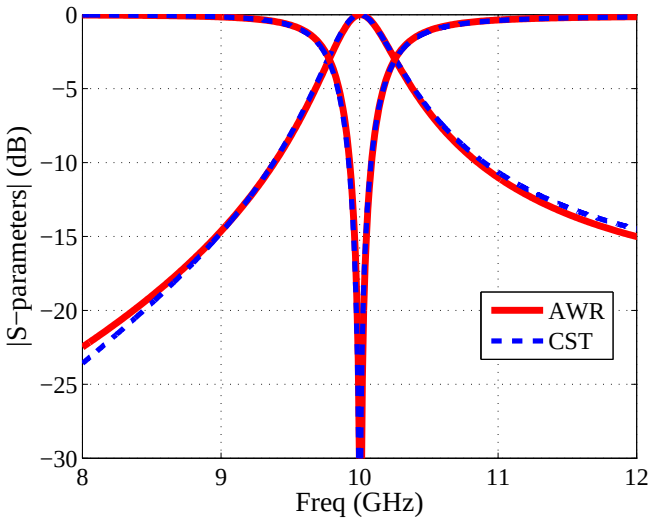

Fig. 5.11: *AWR vs CST Simulated Results for First Order Evanescent Mode Waveguide Filter*

It is evident from Fig. 5.11 that the circuit model is a very accurate representation of the physical waveguide structure. In order to create a tunable filter, tuning components as discussed in Ch. 2 are incorporated into the design. Based on the capacitance required in the simulations, the SMV2019-203 varactor by Isolink is chosen. The equivalent model for this varactor contains a series resistor and capacitor. The expected values for the resistance and capacitance, as specified in [16], is given in Table 5.1, where C is the capacitance for a specified reverse bias voltage and R the resistance. The physical dimensions of the varactor are displayed in Fig. 5.12.

Table 5.1 Specified Model Element Values for the SMV2019 Varactor

Parameter	Value
C_{0V}	2.25 pF
C_{20V}	0.16 pF
R_{0V}	5.5 Ω
R_{20V}	2.2 Ω

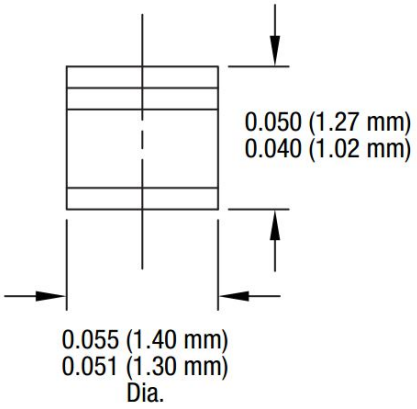

Fig. 5.12: *Isolink SMV2019 Varactor Physical Dimensions [16]*

5.1.3 3-D Topology Design

There are various ways to mount a varactor in a waveguide cavity. Here, a two part mount study is performed for the incorporation of the SMV2019-203 varactors into the evanescent mode waveguide structure. The first part considers structurally different mounting topologies and determines those most suited in terms of required capacitance. The second part determines which of four structurally similar mounts is the most suited for maximised

tunability. A similar study was done by Sickel in [14], where a PIN diode was used and tunability was not a requirement.

5.1.3.1 Mount Study I:

In the first order design calculations and 2-D simulations, it was shown that the whole post-structure together with the parallel plate capacitor had to create an equivalent capacitance of 0.2085 pF. The aim of this study is to determine which among 6 prospective mount topologies, represented in Figs. 5.13a to 5.13f, will accept a realisable capacitance value, similar to that of the chosen Isolink varactor, in order to realise the 0.2085 pF capacitance. The images in Figs. 5.13a to 5.13f are taken from CST as seen looking into the waveguide from port 1.

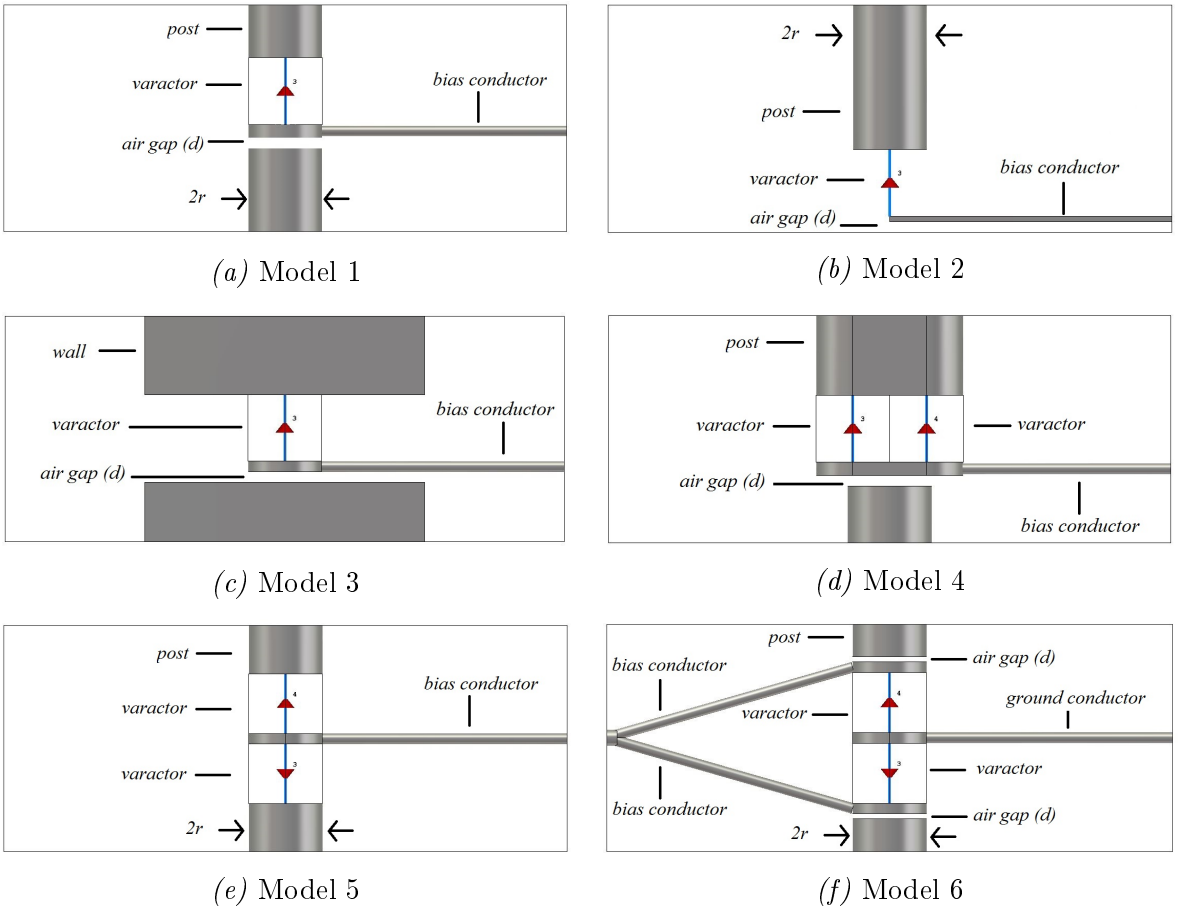

(a) Model 1 *(b)* Model 2

(c) Model 3 *(d)* Model 4

(e) Model 5 *(f)* Model 6

Fig. 5.13: *Mount Study I: Simulated Mount Structures*

Each topology consists of a common conductor that provides the biasing voltage to the diodes. If the conductor is thin enough, it will not disturb the field distribution since it is placed orthogonal to the electric field, its entrance point is located at an electric field minimum, and the magnetic field coupling to the conductor should cancel to zero. Models 1, 2, 3, 4, and 6 have additional air gaps which create a capacitive effect such as seen with a parallel plate capacitor. According to [54], if the perturbation in the E-plane created by the post structure is wide enough, it contributes both capacitive and inductive properties, such as for example in model 3. This is due to the perturbation existing in areas of both

large electric and magnetic fields. In each case, the varactor model is simply a capacitor to ground inserted at the ports, indicated by the blue lines with the red arrows.

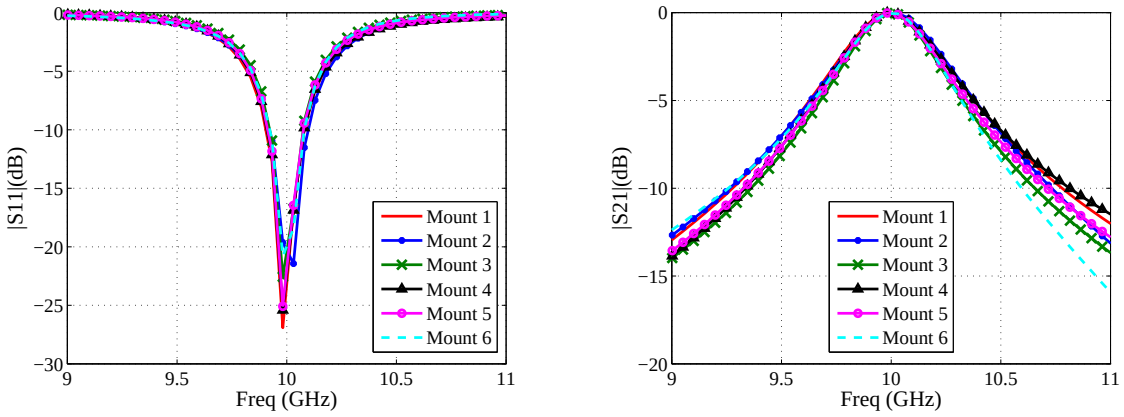

Fig. 5.14: *Optimized Filter Response for Each Mount*

For each topology the optimal length, air gap (if applicable) and added capacitance is optimised for the desired response. The optimised filter responses are shown in Fig. 5.14, with the mount parameters in Table 5.2.

Table 5.2 Mount Study I: Parameters

Mount Number	Air Gap (d) (mm)	Waveguide Section Length (mm)	Required Varactor Capacitance (pF)
1	0.2	4.5	0.167
2	0.1	4.5	0.036
3	0.7	4.5	0.224
4	0.2	5.0	0.084
5	None	4.65	0.090
6	0.1	3.8	0.168

It is clear that models 1, 3 and 6 all allow for capacitance values that are realisable with the SMV2019-203 varactor diode while still maintaining a realistic waveguide length for manufacturing. Mount 3 has the disadvantage of being a set structure, meaning that it would be difficult to compensate for manufacturing errors. All the mounts apart from mounts 5 and 6 are asymmetrical, which could result in higher order modes being excited.

The next consideration is the tunability of each model. Since models 1 and 3 each only provide room for the mounting of a single component, the tunability of model 6 will be more sensitive to the changes in biasing voltage. Given that varactors have a limited range in capacitance, 0.16 - 2.25 pF for the SMV2019, sensitivity will enable wider centre frequency tunability. Therefore, model 6 is used in Mount Study II.

5.1.3.2 Mount Study II:

The aim of this study is to determine which among 3 variations of Model 6 from the previous mount study has the greatest tuning range and maintains the bandwidth the best when altering the varactor capacitance from 0.21 to 0.3 pF.

All the mounts in this study have the same waveguide sections and the mount is located at the same position within the guide. The air gap between the varactor and tuning screw, referred to as d, is the only parameter that is tuned in order to obtain a centre frequency of 10 GHz when each component's capacitance is 0.21 pF.

Mount 6a consists of a central ground plate (width= 2 mm and height= 0.2 mm) and two horizontally orientated biasing wires as can be seen in Fig. 5.15a. Mount 6b's biasing wires exit through the same point and therefore has a diagonal orientation, while the ground is now in the form of a substrate (Rogers RTDuroid 4003C). A lossless substrate was used to improve simulation time. Mount 6b is shown in Fig. 5.15b. Lastly, Mount 6c, presented in Fig. 5.15c is a combination of Mount 6a and 6b since it consists of a solid ground plate and diagonal biasing wires.

The mounts presented in this study differ from Mount 6 in the previous study by having a rectangular ground plate instead of a pad with a cylindrical attachment. The reasons for this change is that a solid support is necessary for mounting the components. With a lesser support in the centre, the weight of the diodes and vibration of the structure could cause the ground structure to bend and possibly short out the diodes depending on the severity of the bend.

It is clear that only very small differences result from the changes in the feeding lines. Table 5.3 provides a summary of the results displayed in Fig. 5.15. The table shows that Mount 6a has the largest percentage change in frequency as well as bandwidth. The least change in bandwidth is shown Mount 6c which has the second largest change in centre frequency. Mount 6b has the smallest change in frequency but the second best maintenance of relative bandwidth.

Table 5.3 Mount Study II: Summary of Results

Mount Label	d (mm)	$\%\Delta f_0$	$\%\Delta$ RBW
6a	0.100	5.35 %	24.9 %
6b	0.117	4.96 %	21.2 %
6c	0.128	5.21 %	19.89 %

To ensure that the component is utilised to its maximum capability, it is important that the smallest capacitance in the mounting structure is that of the component itself. The post creates a capacitance in series with the tuning component. With capacitors in series, the total capacitance is always smaller than the smallest capacitance and therefore the total capacitance is always the most sensitive to changes in the smallest capacitance. Thus, the smaller the post capacitance becomes, the smaller the tuning range will be.

Mount 6a has an air gap of 0.100 mm, mount 6b has 0.117 mm, and mount 6c has 0.128 mm separating the tuning screw from the component. One would expect mount 6b to have the second best tuning range due to it having the second largest air gap; however, the substrate creates another capacitance between its two conductive plates that limits the tunability. As expected mount 6a has the highest tunability and the smallest air gap, but the positioning of the biasing wires adds sensitivity to the bandwidth.

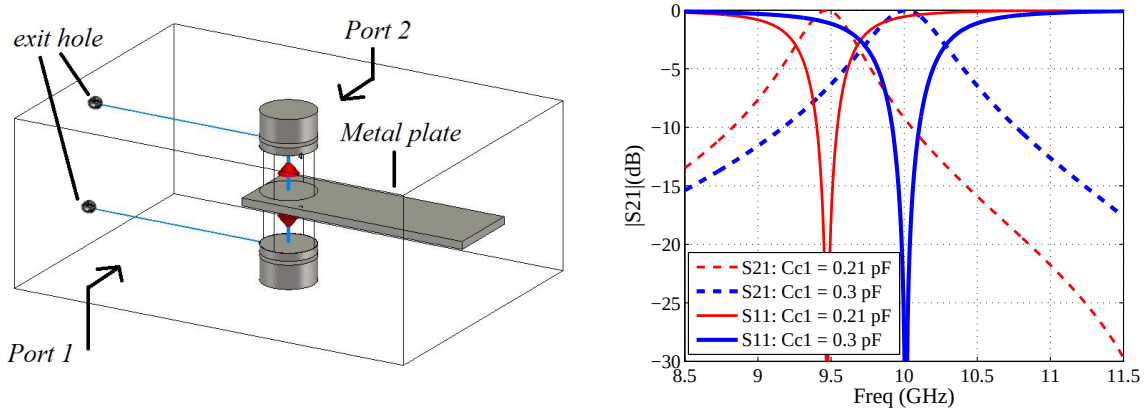

(a) Mount 6a

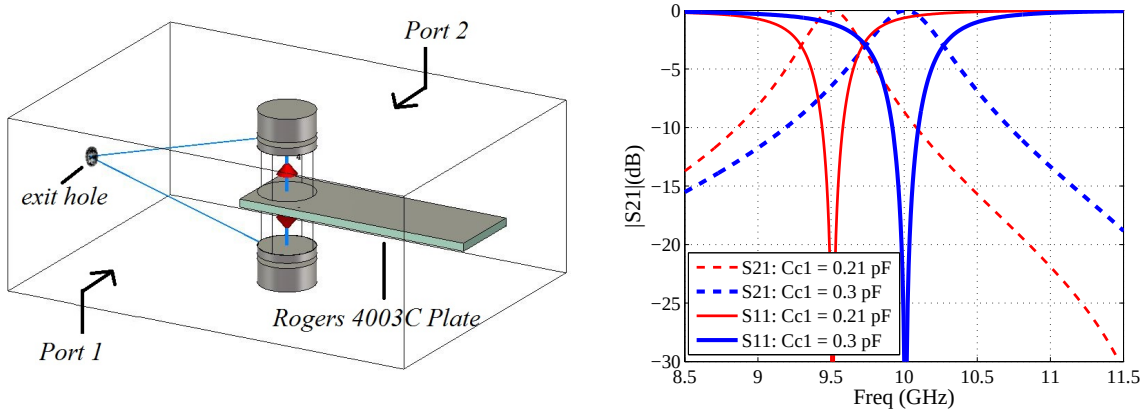

(b) Mount 6b

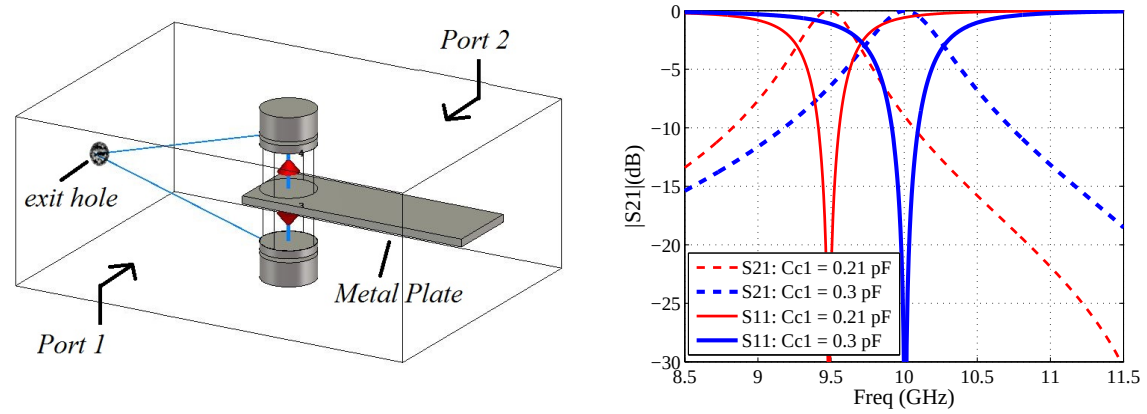

(c) Mount 6c

Fig. 5.15: *Mount Study II: Simulated Mount and Tunability Response*

Taking into consideration that the goals are to maintain relative bandwidth and maximise the tuning range, Mount 6c is the most suitable structure and is therefore selected for the first order filter design.

It should also be noted at this stage that the mounts allow for post-production tuning, as discussed by Sickel [14]. This is an important advantage not available in stripline filters. In the waveguide, the replacement of the top and bottom posts by cylindrical tuners creates such an option in an extremely simple fashion. This should be recognised

as a significant advantage of the filter structure.

5.1.4 Construction and Measurement

For the first order filter an existing aluminium waveguide section is used [14]. The varactor mounting structure is incorporated into the existing section to realise a filter at 10 GHz. The dimensions of the simulated filter are matched to that of the existing waveguide structure and shown in Fig. 5.16. In simulation, the DC biasing wires exit through a small cylindrical cavity on the side of the waveguide. However, the cavity is slightly larger and not cylindrical in the existing waveguide section. Conductive tape is used to minimize the size of the exit hole, as seen in Fig. 5.17. The filter is connected to an impedance tapered X-band waveguide section, previously manufactured at Stellenbosch University, which steps between the different heights of the X-band guides (4.32 mm to 10.16 mm in three sections). A coaxial to X-band waveguide transition is used to enable transmission to and from the 50 Ω coaxial cables connected to the measuring instrument. The different parts of the setup can be seen in Fig. 5.28.

The filter is measured from 6.6 GHz to 14 GHz, in 0.01 GHz increments, using a Keysight PNA-X. Electronic calibration is used for calibrating up to the ends of the coaxial cables. Further calibration is performed post measurement using the TRL calibration technique described in Appendix A and a set of custom-made WR90 calibration standards, readily available at Stellenbosch University. Post calibration, the measurements include only the circuit in Fig. 5.17.

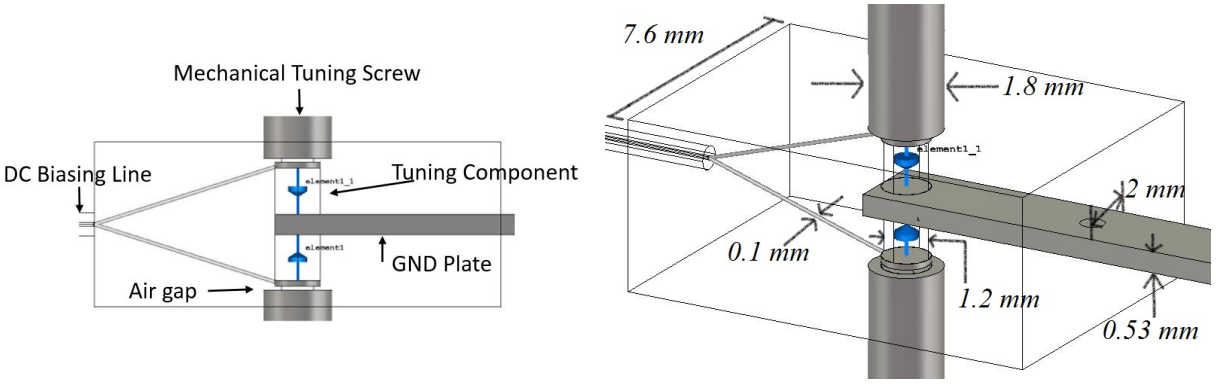

Fig. 5.16: *CST Simulated Model of the Manufactured First Order Filter*

The two-port S-parameter response is shown in Figs. 5.18 through 5.21.

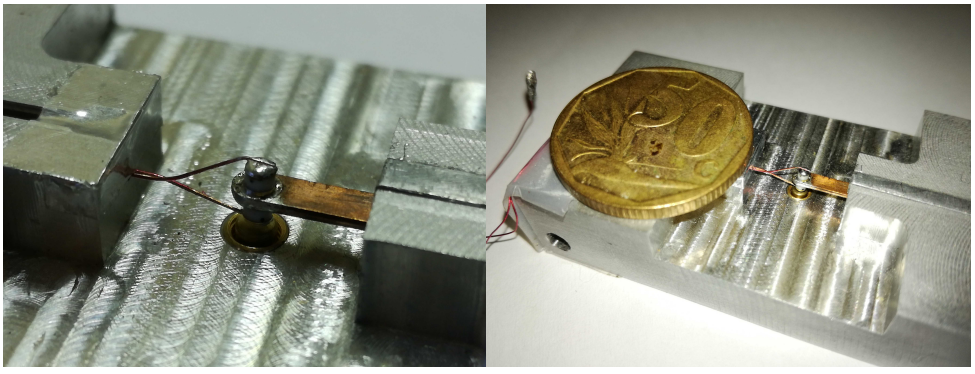

Fig. 5.17: *Manufactured Tunable First Order Filter*

It is important to note that the size of the air gaps between the diodes and tuning screws are dependent on manual tuning accuracy.

5.1.5 Comparing AWR, CST and the Measured Results

Both the AWR and CST models are adjusted slightly to compensate for manufacturing tolerances. The measured results for the minimum and maximum biasing voltage states are plotted together with the AWR and CST simulated results in Fig. 5.18 to 5.21.

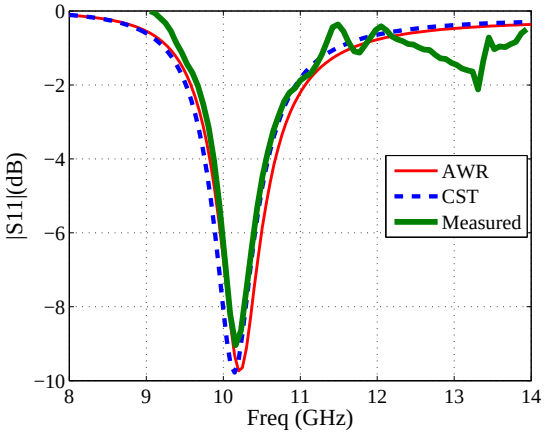

Fig. 5.18: *Simulated vs Measured Input Reflection Coefficient for 0V biasing*

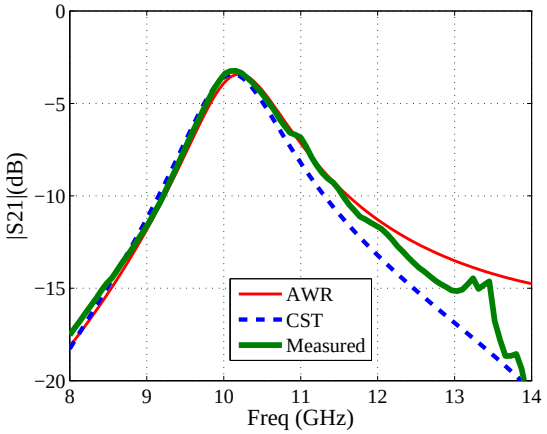

Fig. 5.19: *Simulated vs Measured Transmission Coefficient for 0V biasing*

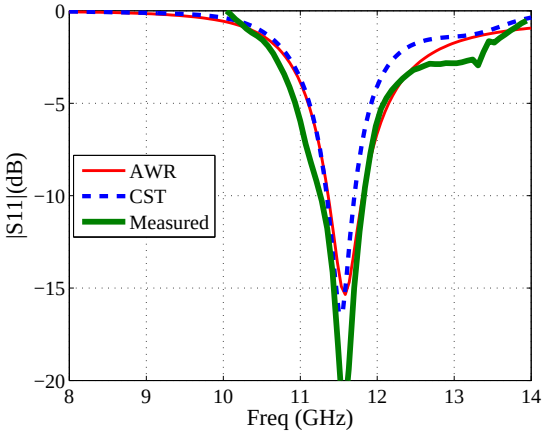

Fig. 5.20: *Simulated vs Measured Input Reflection Coefficient for 20V biasing*

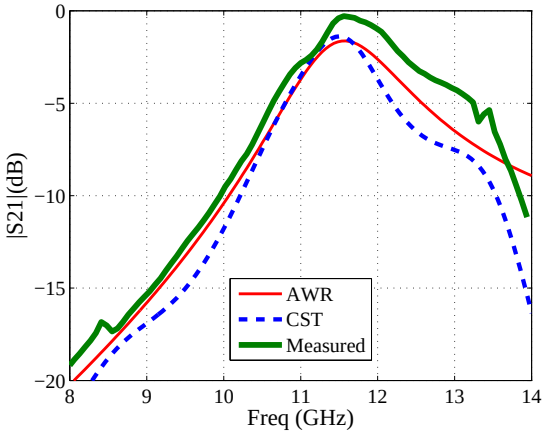

Fig. 5.21: *Simulated vs Measured Transmission Coefficient for 20V biasing*

The slight differences between the measurements and the simulations can be mostly attributed to the cut-off of the TE_{20} mode at 13.12 GHz, not included in the simulation.

Apart from the higher frequency differences, the measured filter shows good correspondence with the simulated designs. The manufactured filter achieved a centre frequency tunability of 1.4 GHz. As the capacitance is decreased, the series resistance is also decreased. Therefore, the insertion loss is greater for the 0 V response where the capacitance and resistance are higher. The change in bandwidth is due to the frequency non-linearity

of the coupling. A summary of the first order filter's measured perfomance is given in Table 5.4.

Table 5.4 Summary of First Order Measured Response

Biasing Voltage	f_0	3-dB ABW	3- dB RBW	Max $S21$	S21 at $1.15f_0$
V	GHz	GHz	%	dB	dB
0	10.1	1.0	9.9	-3.0	-10.0
20	11.5	1.4	12.2	-0.5	-4.0

5.2 Third Order Tunable E-mode Filter

The first order tunable evanescent mode filter provides a good proof of concept which can further be tested in the design of a third order evanescent mode filter.

5.2.1 Theoretical Design and simulation

The design of a third order evanescent mode filter builds on the same fundamental theory as the first order evanescent mode filter design, but the circuit is more complex due to the waveguide sections being of different lengths. The goal is to realise a filter tunable from 10 GHz to 11.5 GHz, with a maximum bandwidth of 10 %.

The circuit model shown in Fig. 5.22 shows that the waveguide lengths for the first and third resonator are the same (ℓ_1), but the second section has a different length (ℓ_2).

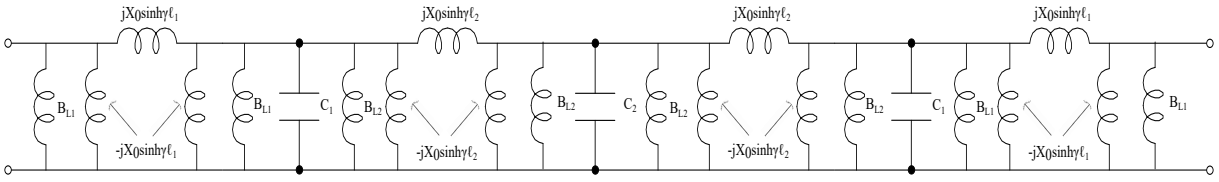

Fig. 5.22: *Detailed Circuit Model for the 3rd Order Evanescent Mode Waveguie Filter*

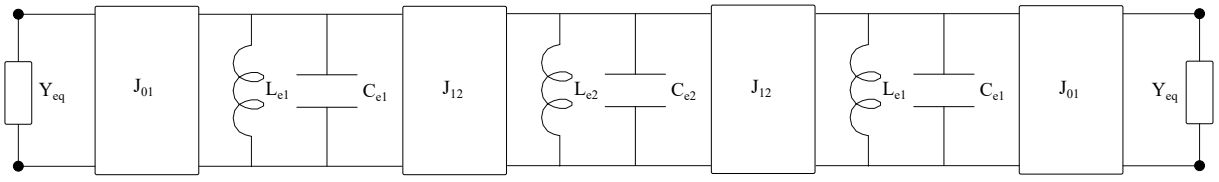

Fig. 5.23: *Third Order Evanescent Mode Waveguide Filter Equivalent Circuit*

As with the first order circuit, the first and last inductor in the circuit shown in Fig. 5.22 are absorbed into the terminating admittance. The Π-inverter sections are replaced by the admittance inverter equivalent and the parallel inductors are combined. The resulting equivalent model for the third order filter is given in Fig. 5.23 and the element values are given by,

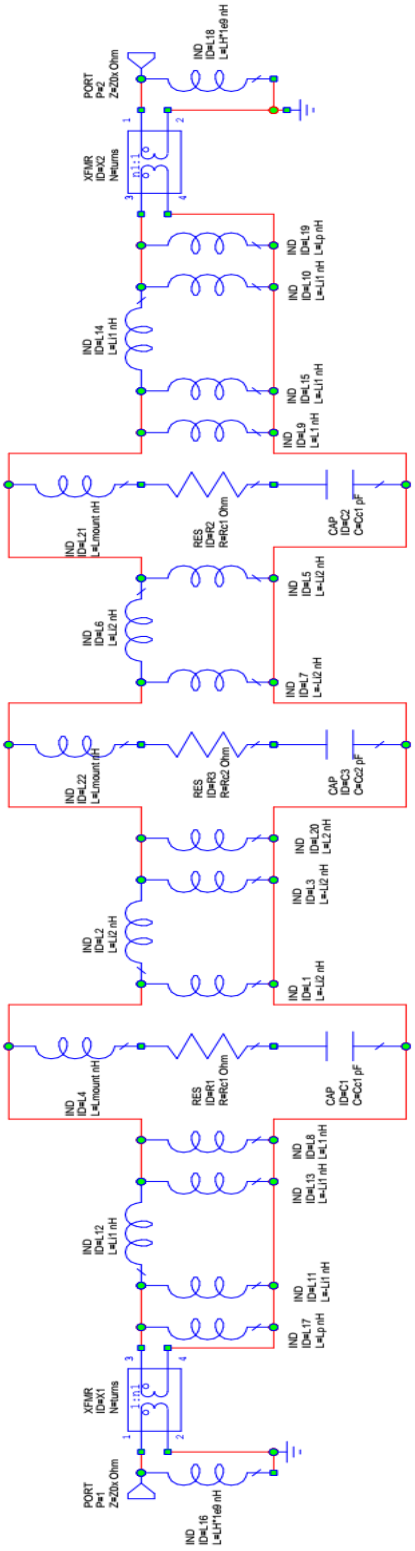

Fig. 5.24: *AWR Model for 3rd Order E-mode Waveguide Tunable Filter*

$$B_{Le1} = B_0 Y_{eq}(\coth(\gamma\ell_2) + \coth(\gamma\ell_1)) = \frac{\Delta_{cm} Y_A C_1}{\Delta} \tag{5.2.1}$$

$$B_{Le2} = 2Y_{eq} B_0(\coth(\gamma\ell_2)) = \frac{\Delta_{cm} Y_A C_2}{\Delta} \tag{5.2.2}$$

$$J_{01} = \frac{Y_{eq}}{X_0 \sinh(\gamma \ell_1)} = Y_A \sqrt{\frac{G_0 C_1}{g_0 g_1}} \tag{5.2.3}$$

$$J_{12} = \frac{Y_{eq}}{X_0 \sinh(\gamma \ell_2)} = Y_A \sqrt{\frac{C_1 C_2}{g_1 g_2}} \tag{5.2.4}$$

where ℓ_1 and ℓ_2 are the lengths of the waveguide sections and C_1 and C_2 are the low-pass prototype capacitances. Once again, it is possible to set Y_A equal to Y_{eq} in order to simplify the calculations.

A numerical solution is required for the lengths and capacitances of the third order evanescent mode filter design due to the hyperbolic trigonometric functions. However, since the capacitance values of the available varactor is known, the numeric problem is simplified and can be taken into account in the AWR simulations.

The AWR equivalent circuit for the third order evanescent mode waveguide filter is shown in Fig. 5.24. It features the equivalent model for transitioning from a reduced height X-band waveguide to a K-band waveguide at both ports. The entire mounting structure is modelled as an equivalent RLC network.

5.2.2 3-D Topology Design

Based on the successful results of the first order filter measurements, the same mount topology is chosen for the third order design. The central mount is rotated, with reference to the first and third, in an attempt to prevent unwanted higher order modes from being excited. The resulting structure is shown in Fig. 5.25. Once again the equivalent varactor model, consisting of a tunable series resistor and capacitor, is added in the circuit simulator in CST, as shown in Fig. 5.26.

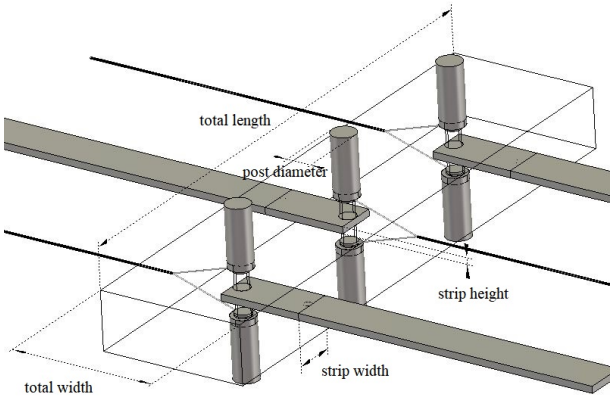

Fig. 5.25: *CST Model for 3rd Order E-mode Waveguide Tunable Filter*

5.2.3 Construction and Measurement

The structure in Fig. 5.27 is manufactured at Stellenbosch University. The metal container is constructed from aluminium, the metal strip is made from brass and the biasing wires have an insulating coat which is only removed at the contact areas. The exiting

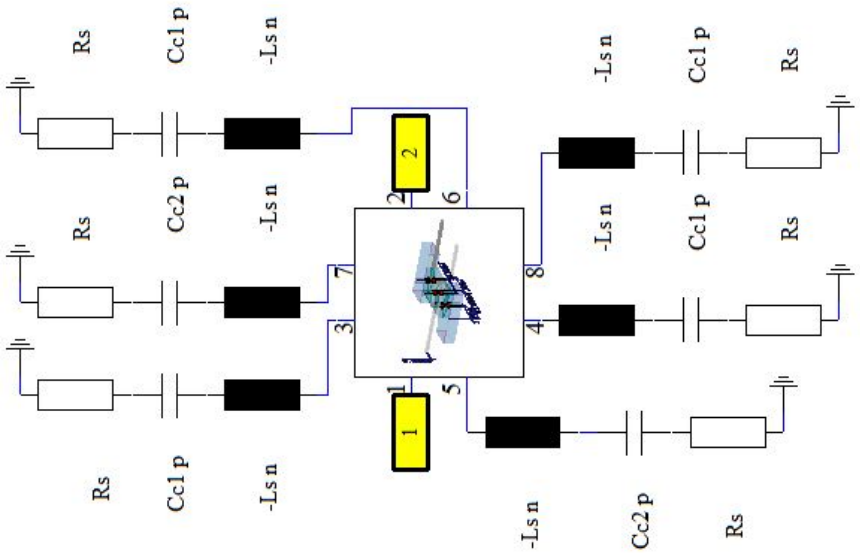

Fig. 5.26: *CST Circuit Model for 3rd Order E-mode Waveguide Tunable Filter*

slots for the biasing wires and ground plates are covered using conductive tape to prevent external coupling as best possible. Table 5.5 shows a summary of the design and manufactured parameters.

Table 5.5 Designed vs Manufactured Dimensions

Parameter	Designed (mm)	Manufactured (mm)
total length	23.0	22.8
total width	10.7	10.1
len1	1.5	1.4
len2	10.0	10.0

The measurement setup and calibration is performed using the same measuring equipment and calibration standards as in the first order case except that one additional biasing supply line is required. The measurement setup is shown in Fig. 5.28 where each transition stage is labelled.

The air gaps are set for the 0 V biasing case where the varactor capacitance and resistance is the greatest. Thereafter, the tuning screws are kept stationary as the biasing voltages for the varactors are altered. Fig. 5.29 depicts the filter response when the reverse bias voltage is tuned in increments of 10 V. The voltage for the first and third resonators is supplied by a single voltage source while the second resonator has a separate supply. The two supplies can be seen in Fig. 5.28. It is therefore possible to bias the resonators separately in order to get the best tuned response.

As with the first order response, the third order response also shows the TE_{20} mode cut-off at 13.12 GHz. From Fig. 5.29 it is clear that the bandwidth of the filter increases as the biasing voltage is increased, and so also the frequency is increased. Note that an increase in voltage results in a decreased diode capacitance. The figure also shows that the loss increases significantly with the increase in capacitance, which can be attributed

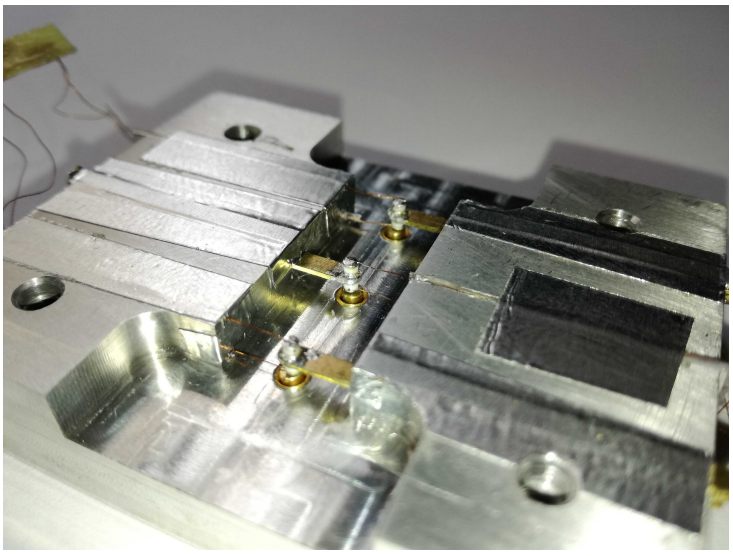

Fig. 5.27: *Manufactured 3rd Order E-mode Waveguide*

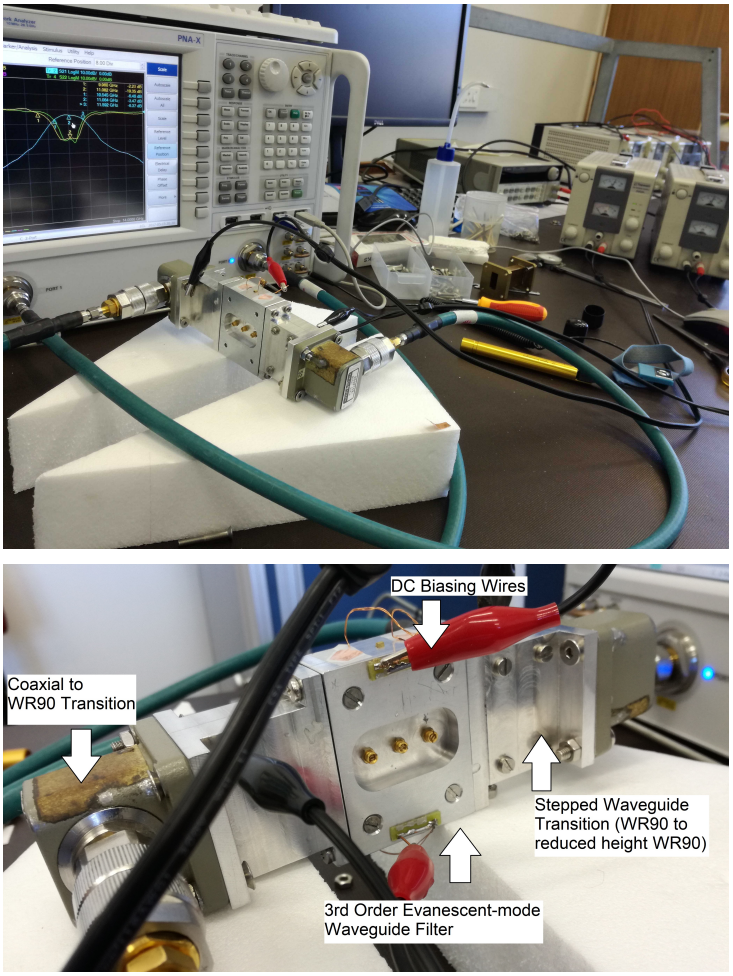

Fig. 5.28: *Measurement Setup for 3rd Order tunable filter*

to the increase in the series resistance of the varactors as per Fig. 2.2b. A summary of the measured results is given in Table 5.6.

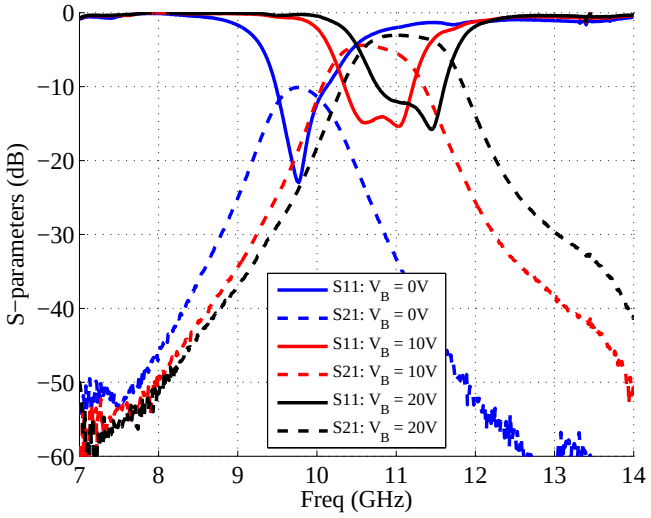

Fig. 5.29: *Measured Response of Tunable 3rd Order E-mode Waveguide*

Table 5.6 A Summary of the E-mode Waveguide Measurements

V_B	f_0	3-dB RBW	3-dB ABW	Max IL
(V)	(GHz)	(%)	(MHz)	(dB)
0	9.8	7.06	691	10.1
10	10.75	10.20	1097	4.0
20	11.1	10.55	1168	3.0

5.2.4 Comparing Simulated and the Measured Results

The measurements are compared to the simulated results in Figs. 5.30 and 5.31. Note that the values in the simulated circuits, presented in Figs. 5.24 and 5.25, are altered to compensate for the manufacturing tolerances.

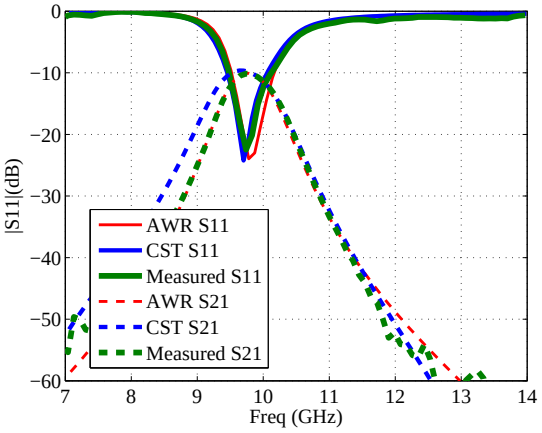

Fig. 5.30: *Simulated vs Measured S-parameters for 0V biasing*

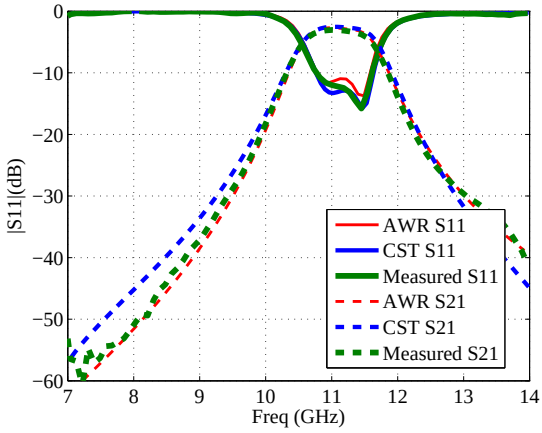

Fig. 5.31: *Simulated vs Measured S-parameters for 20V biasing*

Good agreement is achieved for both models. It is clear that the manufactured third order filter can be accurately modelled in both AWR and CST. The good agreement with AWR means that a rather complex structure can be simulated in a circuit simulation,

which saves both time and computational resources. The figures also prove that the entire mounting structure, consisting of two tuning screws, a central ground plate, two biasing wires and two SMV2019 varactor diodes, can be modelled using only a series RLC combination. The inductance required in the series RLC model in AWR is a fixed value for all the biasing states and can therefore be attributed to inductance added by fixed structures, i.e. the tuning screws, the biasing wires and the ground plate. For the full wave simulation, the resistance was altered from 10 Ω to 3 Ω and the capacitance from 0.61 pF to 0.18 pF as the biasing voltage is increased from 0 V to 20 V, which are realistic values when referring to the data sheet of the component.

5.3 Conclusion

This chapter provides a novel structure for narrow-band tunable evanescent mode waveguide filters. Though the structure was previously used in a waveguide switch [56], this is the first implementation in a tunable filter. The discussion presented in this chapter shows that the proposed filter can be modelled by using a circuit simulation or a 3-D full wave simulation. A filter centre frequency tunable over 1 GHz is achieved using this structure. A significant advantage of the waveguide filter is that post-production tuning is available through manual tuners. The drawbacks of this structure is that the bandwidth is extremely sensitive to the change in frequency due to the hyperbolic function dependency of the coupling and resonator inductance. It will be difficult however to compensate for the change in coupling, since it is inherent to the evanescent mode waveguide structure. Further research can be done on compensating for the change in bandwidth.

Chapter 6

Thermal Properties and Power Handling: Planar Versus Waveguide

Though affordable, small, easily obtained and incorporated, varactors are not often used in high power environments due to their non-linear characteristics and power dissipation limitations. This chapter considers the power limits of each of the filters due to the varactors. A simulation-based study on the power dissipation in each varactor is presented in Sec. 6.1, the heat sink capabilities of each mounting structures is discussed in Sec. 6.2, and a simulation-based study on the non-linearity due to the varactors is given in Sec. 6.3.

6.1 Power Dissipation Study

The power dissipation study involves optimal tuning of each filter at a set of centre frequencies, and determining the percentage of power that is dissipated in each varactor. As in chapters 4 and 5, an S-parameters model is extracted from the EM simulation and used in the 2-D circuit simulation in CST, with varactor models connected to the discrete ports. The filter simulation model which most accurately represents the measured results for each filter is used. A one watt AC source is added to the input port (port 1) of the EM model and the output port (port 2) is terminated with the impedance of the EM model port at the resonant frequency. The AC simulation is performed for the maximum and minimum tuning ranges of each filter. Probes are used to monitor the voltage and current at each port in the circuit, enabling the calculation of the active power supplied, received and dissipated. The following equation is used for the calculation:

$$P = \frac{1}{2}\Re\{VI^*\} \tag{6.1.1}$$

where the asterisk refers to the conjugate form of the vector.

6.1.1 Planar Filter

The full-wave EM simulated suspended substrate structure from Ch. 4, with discrete ports and SMA connectors, is shown in Fig. 6.1, while the AC analysis circuit set-up is shown in Fig. 6.2. It should be noted that probes 1 through 10 in the 2-D circuit are connected to discrete ports 3 through 12 from the EM model, respectively. Probes 1 and 2 are therefore both connected to the first resonator, probes 3 and 4 to the second etc.

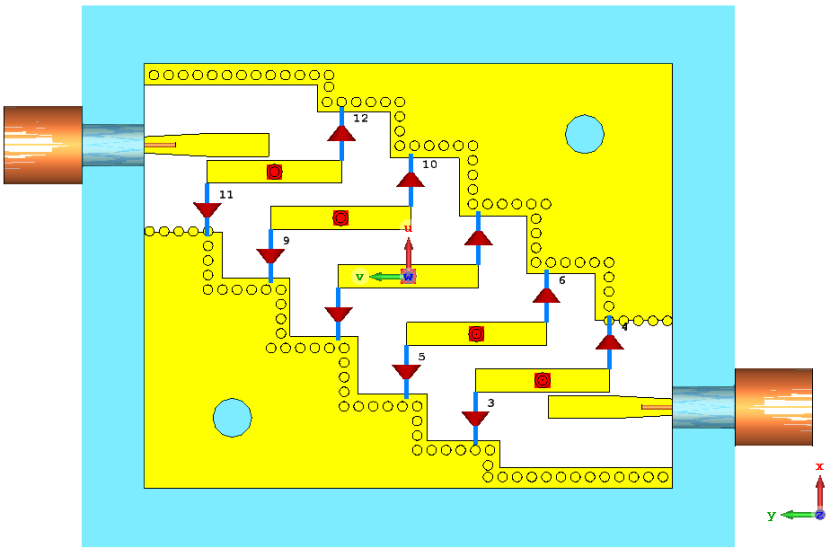

Fig. 6.1: *Tunable Planar Filter EM Model*

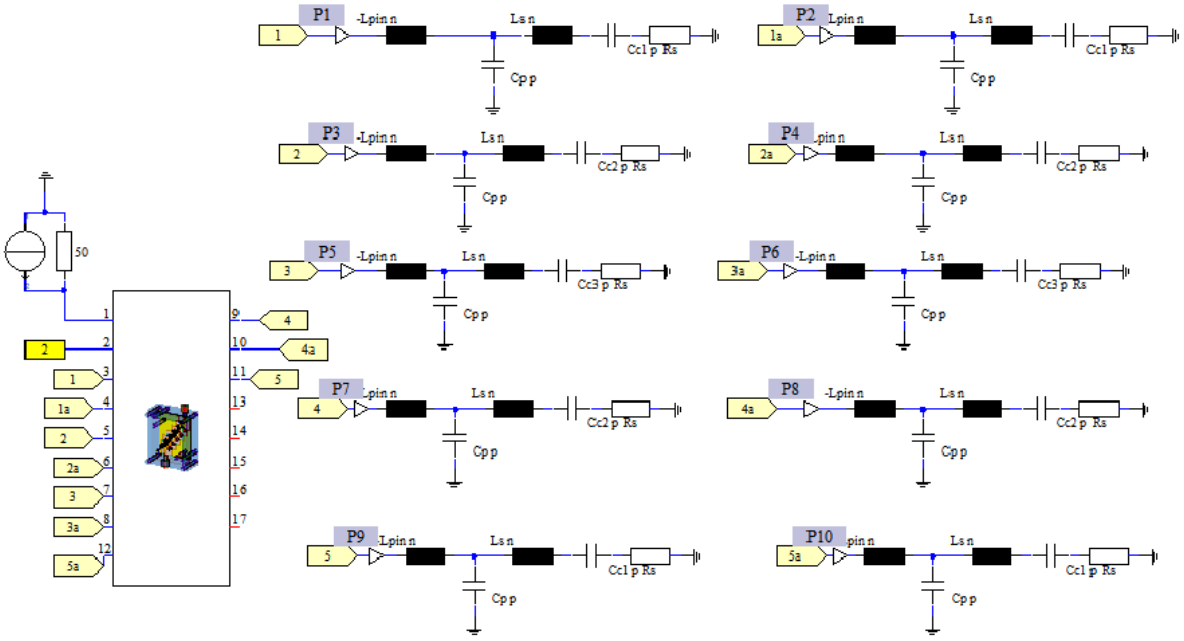

Fig. 6.2: *Planar Filter Power Simulation Circuit Set-up*

An AC current of 400 mA parallel to a 50 Ω resistance is connected to port 1 and provides 1 W available power at the input. Port 2 of the EM circuit is terminated with a 50 Ω resistance and monitored by probe 11.

The input and output power for the lowest frequency band are shown in Fig. 6.3. The filter centre frequency is 11.75 GHz and the maximum transmission coefficient observed

in the measurements for this band is −6 dB, which corresponds to an output power of 270 mW for the given 1 W input in the simulation. This is confirmed in the figure.

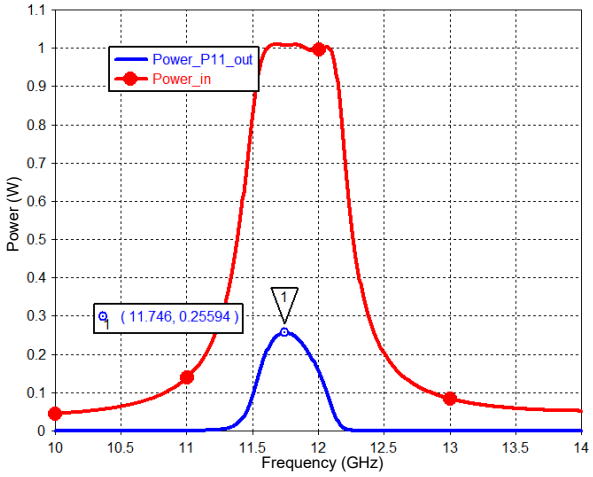

Fig. 6.3: *Active Input and Output Power for Planar Filter at* 11.75 *GHz*

The magnitude of the voltages and currents observed at each discrete port probe are shown in Fig. 6.4. The largest voltages are observed at the first and second resonator and occurs at the upper frequency band edge. The largest current is also observed at resonator 1 and 2. However, the current peaks are seen at the lower frequency band edge. Since the voltages and currents at the two ports of each resonator are very similar, the expected symmetrical properties between the two edges of each resonator is clearly shown.

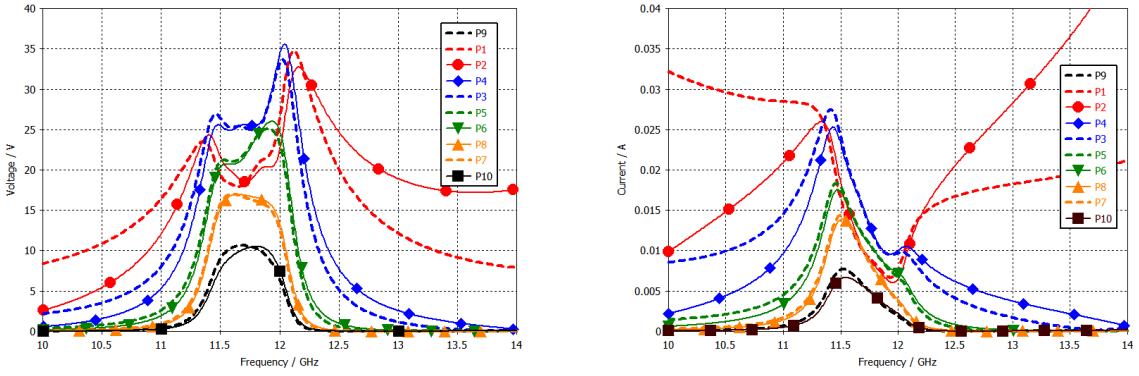

Fig. 6.4: *Magnitude of Varactor Model Voltages and Currents for Planar Filter at* 11.75 *GHz*

The largest difference observed between two probes on a single resonator occurs out-of-band for the very first resonator (P1 and P2) seen by the AC signal. At the out-of-band frequencies, energy is not expected to couple from one resonator to the next, however, from the probe data it is clear that some energy couples to the first and second resonator. Probe P2 is physically closer to the signal source than probe P1 and shows a higher voltage and current than probe P1 for frequencies above f_0, but a lower voltage and current for frequencies below f_0. This can be attributed to the input coupling and the effective length

of the resonator. Since the input coupling and the coupling between resonators are not at a single point as is modelled in the ideal case, asymmetry is expected.

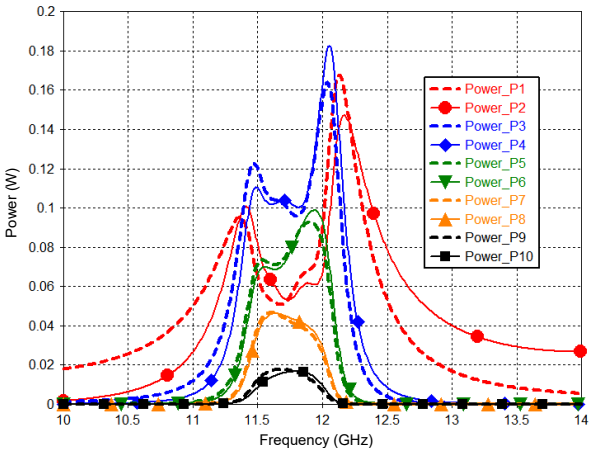

Fig. 6.5: *Varactor Power Requirements for Planar Filter at* 11.75 *GHz*

The power at each probe is shown in Fig. 6.5. The maximum power dissipated in a varactor model is 182 mW and occurs at probe 4, connected to the second resonator seen from the input. It is clear that the largest power dissipation occurs at the band edges of the passband. Therefore, the rounded shoulders of the passband can largely be attributed to the power dissipation in the varactors. The varactor power handling capability should therefore be at least 18 % of the input power.

To determine if the power dissipation is the same for other frequency bands, the planar filter is tuned to its upper frequency band ($f_0 = 12.15$ GHz) and the same AC simulation in performed. The input and output power for this band is shown in Fig. 6.6. The output power is 22 % of the input power which corresponds well with the measured results. The currents and voltages at the varactor probes are shown in Fig. 6.8. Once again good agreement between the two probes of each resonator is obtained, with the exception of the out of band probe measurements for the first resonator.

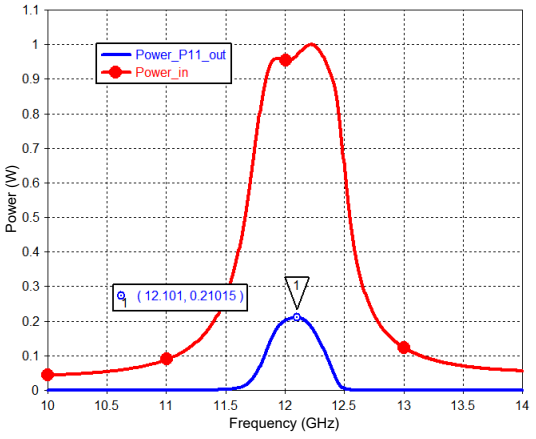

Fig. 6.6: *Active Input and Output Power for Planar Filter at* 12.15 *GHz*

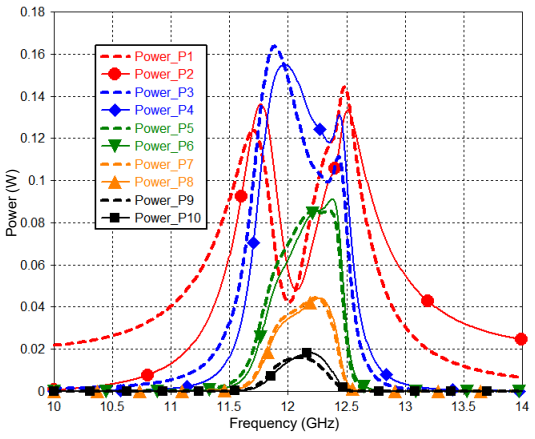

Fig. 6.7: *Varactor Power Requirements for Planar Filter at* 12.15 *GHz*

In comparison to the 11.75 GHz band, the voltages are lower and the currents higher, resulting in a very similar overall power dissipation plot as shown in Fig. 6.7. For the upper frequency band the maximum active power dissipation of 170 mW occurs at 12.4 GHz.

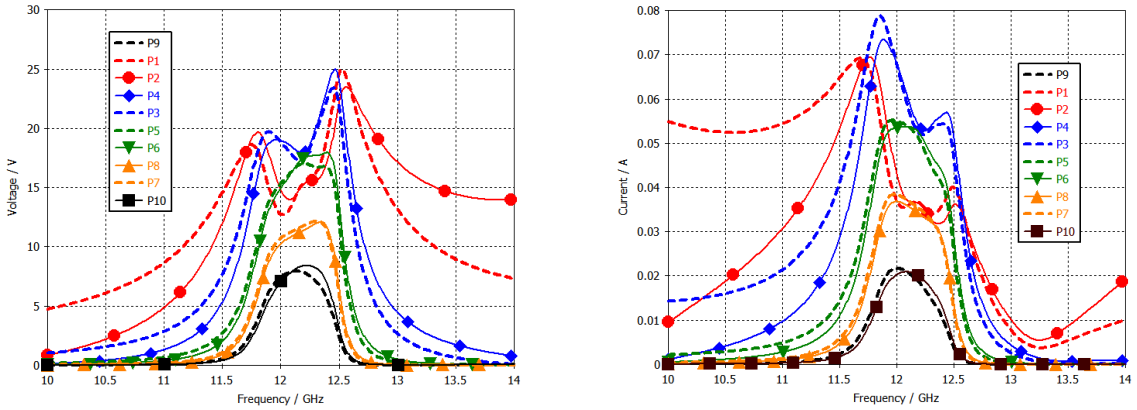

Fig. 6.8: *Magnitude of Varactor Model Voltages and Currents for Planar Filter at 12.15 GHz*

In order to compare the varactor power requirements of both filters, the same analysis is performed on the evanescent mode waveguide filter.

6.1.2 Waveguide Filter

The full-wave simulated evanescent mode waveguide structure for Ch. 5, with reduced height X-band transitions and discrete ports, is shown in Fig. 6.9, while the AC simulation circuit set-up is shown in Fig. 6.10.

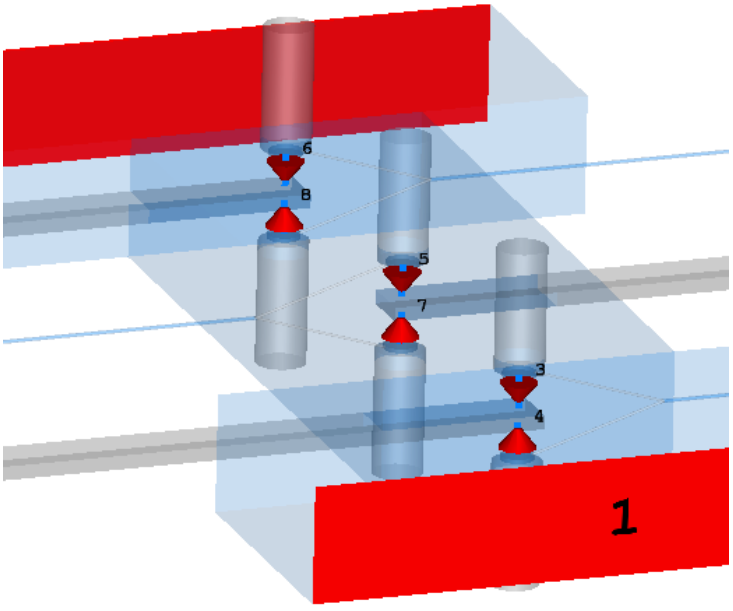

Fig. 6.9: *Tunable Waveguide Filter EM Model*

For this circuit, probes 1 through 6 in the circuit simulation are connected to discrete ports 3, 4, 5, 7, 6 and 8 in the EM model, respectively. This order is a result of translating the ports in CST. Probes 1 and 2 are both connected to the first resonator mount seen from port 1, probes 3 and 4 to the second and probes 5 and 6 to the third.

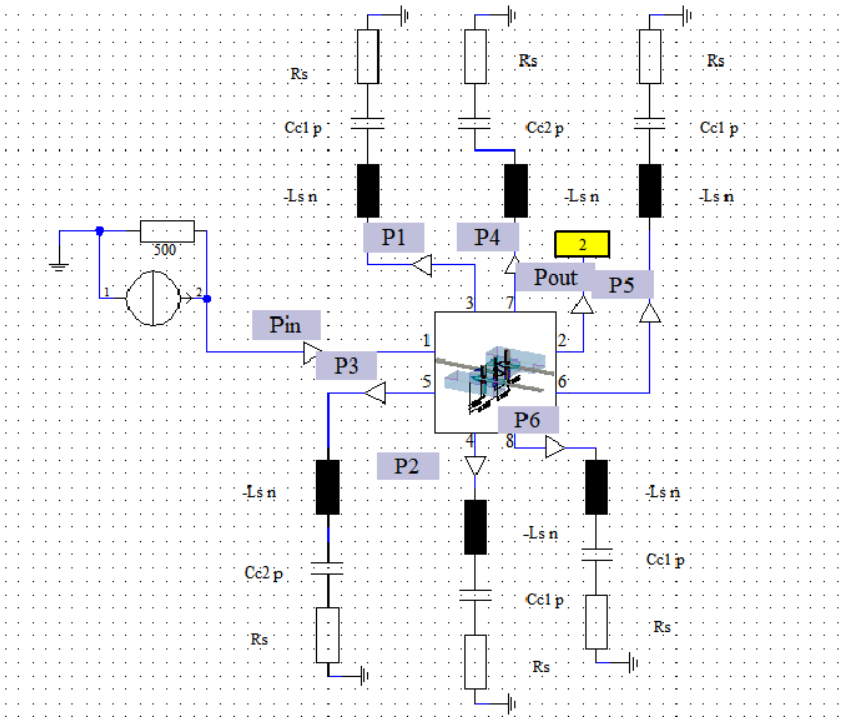

Fig. 6.10: *Simulation Set-up for Waveguide Filter Power Dissipation Study*

An AC current of 128 mA parallel to a 500 Ω resistance supplies 1 W to port 1 of the EM circuit. The output of the EM model, port 2, is terminated with a 500 Ω resistance, which is the impedance of the reduced height X-band waveguide at 9.9 GHz. The power at the input and output of the EM model are shown in Fig. 6.11. The maximum transmission coefficient observed in the measurements for this band is −10 dB, which corresponds to an output power of 100 mW for the given 1 W input in the simulation. This is confirmed in the figure.

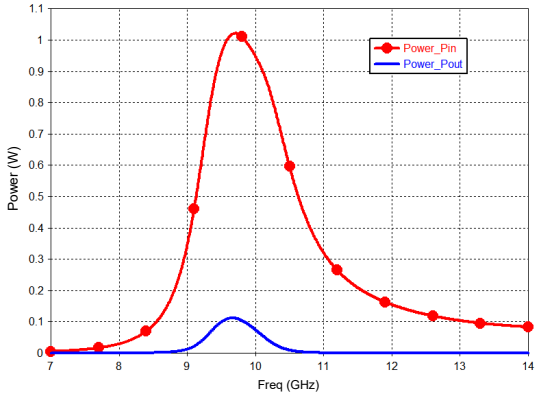

Fig. 6.11: *Active Input and Output Power for Waveguide Filter at 9.9 GHz*

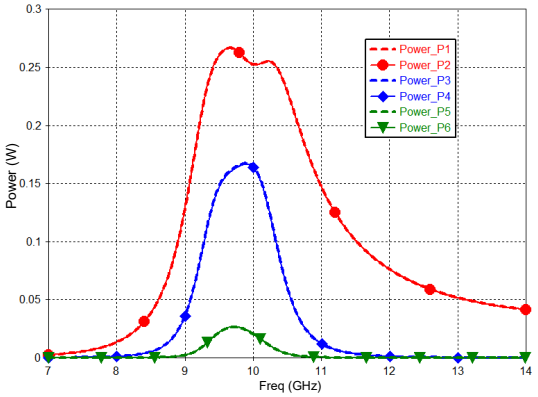

Fig. 6.12: *Varactor Power Requirements for Waveguide Filter at 9.9 GHz*

The magnitude of the voltage and current observed at each discrete port is shown in Fig. 6.13. The maximum voltage, 13.5 V, for this band is located at the centre frequency and observed by the probes on the second resonator. The maximum current, 225 mA, is observed at the first resonator for the band edge frequencies. Unlike the planar results, the voltages and currents observed at the two ports of each resonator are exactly the same for the waveguide structure. The two ports of each resonator are at very similar locations for this structure, therefore a travelling wave "sees" the two ports of each resonator at the same time. Since the varactors are positioned back to back, the precise agreement of the measurements shows that a symmetry exists about the metal ground plate.

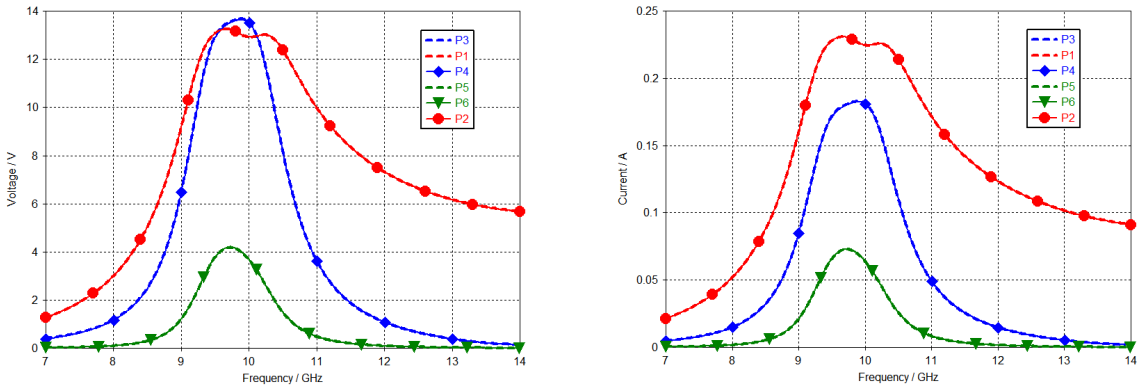

Fig. 6.13: *Magnitude of Varactor Model Voltages and Currents for Waveguide Filter at 9.9 GHz*

The calculated powers are shown in Fig. 6.12. The maximum power dissipation, 265 mW, is observed at probes P1 and P2 on the first resonator. It is clear that the maximum power dissipation occurs at the band edges of the passband. Therefore, the rounded shoulders of the passband can largely be attributed to the power dissipation in the varactors. The varactors should thus be capable of handling 27 % of the input power for the lower frequency band.

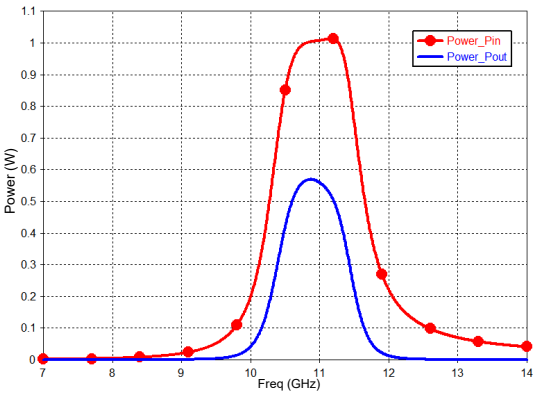

Fig. 6.14: *Active Input and Output Power for Waveguide Filter at 11.1 GHz*

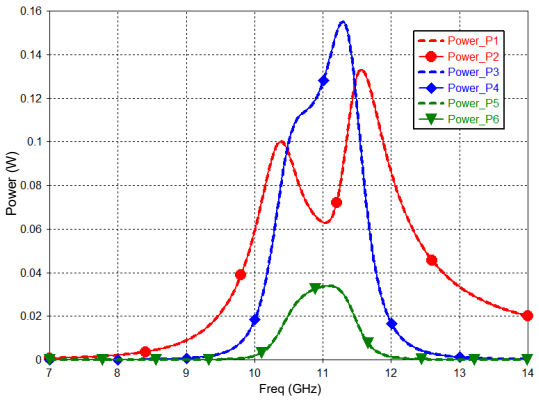

Fig. 6.15: *Varactor Power Requirements for Waveguide Filter at 11.1 GHz*

In order to determine if a similar power handling capability is required in the upper frequency band, the waveguide filter is tuned to its upper centre frequency of 11.1 GHz

and the same AC analysis is performed. The filter input and output power is shown in Fig. 6.14. The power seen at the output is 58 % of the input power for this band. Once again good agreement is obtained between the two probes of each resonator as seen in Fig. 6.16.

In comparison to the 9.9 GHz band, the maximum voltage magnitude is 21 V more and the maximum current magnitude increased with 50 mA, resulting in a power dissipation plot as shown in Fig. 6.15. For this frequency band the maximum power dissipation is 155 mW and occurs at 11.2 GHz. The varactors should thus be capable of handling 16 % of the input power for the upper frequency band.

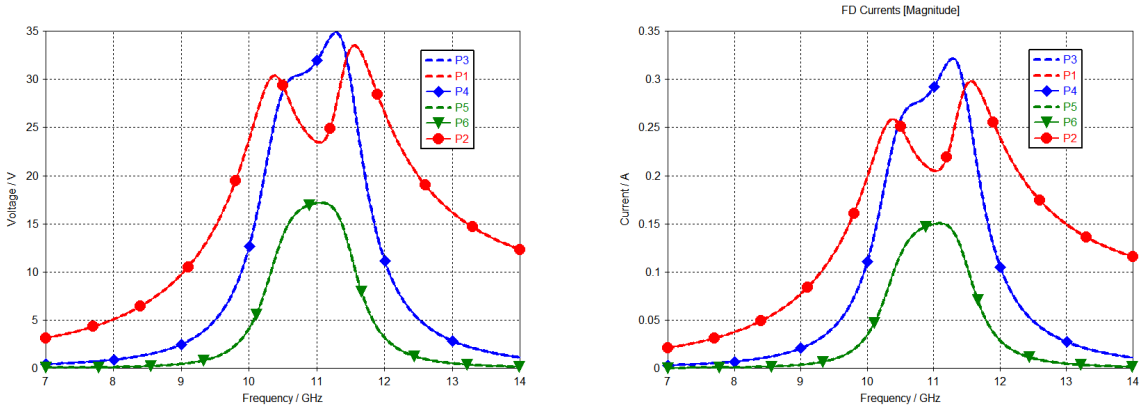

Fig. 6.16: *Magnitude of Varactor Model Voltages and Currents for Waveguide Filter at 11.1 GHz*

It is clear that the varactor power requirements for the waveguide filter are determined by the lower frequency band, while the planar filter's varactor requirements are more or less the same for the entire tuning range. This is due to the difference in varactor type and tuning range.

From the power plots it is possible to determine the total power dissipation due to the varactors of each filter and conclude what power is dissipated in the structure itself. The following equation is used for each structure, and the results are presented in Table 6.1.

$$P_{in} = P_{out} + P_{dvar} + P_{dstruct} \tag{6.1.2}$$

where P_{dvar} and $P_{dstruct}$ are the power dissipations in the varactors and the structure, respectively.

Table 6.1 Power Dissipated in the Structure

Structure	Frequency (GHz)	P_{out} (W)	P_{dvar} (W)	$P_{dstruct}$ (W)
Planar	11.75	0.26	0.61	0.13
Planar	12.15	0.22	0.65	0.13
Waveguide	9.90	0.10	0.88	0.01
Waveguide	11.10	0.54	0.45	0.01

From the table above it is clear that the varactor power dissipation is the overriding factor for the total loss of power in each filter and that the dissipation due to each structure is constant across the tuning range. The planar structure itself contributes to

13 % of the dissipated power while the waveguide structure only contributes to 1 %. Since the varactors are the most sensitive components in each filter, the structures themselves should be used as a heat sink to increase the power capabilities of the filter.

6.2 Thermal Properties of Each Structure

The heat sinking ability of a structure can improve the overall power handling capabilities of the filter by protecting the sensitive tuning components. The following equation is often used to determine the dissipated power in a diode:

$$P_D = \frac{T_J - T_A}{R_{\theta_{total}}} \tag{6.2.1}$$

where $R_{\theta_{total}}$ represents the combined thermal resistance in ^{o}C/W, T_J represents the maximum temperature of the diode junction and T_A the ambient temperature (25 ^{o}C).

The specified absolute maximum ratings in the data sheet is for a diode suspended in air. Therefore, any heat sinking ability the mount might have can increase the absolute maximum power. The specification for both the SMV1405 and SMV2019 is 250 mW maximum power dissipation.

Since the varactors are added to the filter in the 2-D simulation the thermal capabilities are not simulated. Therefore, to quantify the effect of the filter structure on the maximum power dissipation of the varactors, the total thermal resistance should be considered. The combined thermal resistance is a sum of the thermal resistance from the diode junction to its case, from the diode case to the mount (heat sink) and from the heat sink to ambient,

$$R_{\theta_{total}} = R_{\theta_{JC}} + R_{\theta_{CH}} + R_{\theta_{HA}} \tag{6.2.2}$$

where $R_{\theta_{JC}}$ refers to the thermal resistance from junction to case (packaging), $R_{\theta_{CH}}$ from case to heat sink and $R_{\theta_{HA}}$ from heat sink to ambient.

The thermal resistance from case to the heat sink can be calculated by taking into account the cross-sectional area of the heat sink (A in metres-squared) perpendicular to the direction of heat flow, the length of the medium (x in metres) parallel to the heat flow, and the thermal conductivity of the heat sink (k in watts per Kelvin-metre), as shown in the equation below.

$$R_{\theta_{CH}} = \frac{x}{A \times k} \tag{6.2.3}$$

Assuming that the thermal resistance from the heat sink to air is insignificantly small, and that the same component is used for both the planar and waveguide filter designs, a comparison can be drawn for the thermal resistance from case to heat sink for the planar and waveguide structures.

For the planar filter, a varactor is mounted at one end to the 18 μm by 7.19 mm by 1.18 mm copper resonator, and at the other end to the copper ground plate which is also 18 μm thick. Similar to current, heat follows the path of least resistance. Therefore, the ground plate rather than the resonator will function as a heat sink in the case of the planar filter.

The length from the start of the ground plate to the stepped wall is considered as the length of the heat sink (x_{PL}) and is equal to 1 mm. The cross-sectional area of the ground plate is given by

$$A_{PL} = 3.6mm \times 18\mu m = 6.48 \times 10^{-8} m^2 \tag{6.2.4}$$

The ratio of the length to the cross-sectional area of the heat sink is then,

$$r_{PL} = \frac{x_{PL}}{A_{PL}} = 15432 \text{ per metre} \tag{6.2.5}$$

For the waveguide filter a varactor is mounted on a 0.5 mm by 2 mm by 5.8 mm metal plate at one end and soldered to a 1.4 mm thick wire at the other end. The heat sink in this case is therefore the metal plate. The cross-sectional area of the metal plate is calculated as,

$$A_{WG} = 0.002 \times 0.0005 = 1 \times 10^{-6} m^2 \tag{6.2.6}$$

The length of the metal plate is approximately 5.8 mm. Therefore, the ratio of the length to the cross-sectional area af the metal plate is

$$r_{WG} = \frac{x_{WG}}{A_{WG}} = 5800 \text{ per metre} \tag{6.2.7}$$

Under the assumptions that $R_{theta_{JC}}$ is the same for the planar and waveguide filters and that the thermal conductivity for the metals in both designs are equal, the ratio $r_{PL} : r_{WG}$ determines the theoretical difference in thermal dissipation and is given by:

$$\frac{r_{PL}}{r_{WG}} = \frac{2.7}{1} \tag{6.2.8}$$

Therefore, the waveguide structure's thermal resistance is to a first approximation, 2.7 times smaller than that of the planar filter when based on the dimensions of the heat sink alone. The thermal investigation is limited to the calculations above due to time constraints.

6.3 Non-linear Varactor Behaviour and the Effects on the Filter Operating Range

Apart from power dissipation and heat sinking capabilities, it is also important to consider the effect of the non-linearity of the varactor diodes on the filter non-linearity.

The non-linear voltage to current relationship of varactor diodes can limit the filter's output power and create spurious in-band signals, due to harmonic generation and inter-modulation. Given that RF signals may cause the potential across a diode to exceed the reverse breakdown or junction voltage, the non-linearity of the filter may be increased by the non-linearity of the diodes. Therefore, the non-linearity of a tunable filter is a function of both the RF signal power and the biasing voltage.

This is one of the reasons varactors are rarely used for high power applications. Unlike PIN diodes, varactors operate close to both their reverse breakdown and junction voltages, limiting the amount of power that can be dissipated in the varactor before harmonic signal levels become problematic. This section discusses the SMV1405 and SMV2019 diode non-linearity and the effects thereof on each filters' power and tuning capabilities.

6.3.1 SMV1405 and SMV2019 non-linearity

A brief study is done on the non-linearity of the SMV1405 and SMV2019 varactor diodes used in the planar and waveguide filters. Some of the critical parameters for the non-linear characteristics of a varactor is depicted in Fig. 6.17. The parameter values for the SMV1405 and SMV2019 are given in Table 6.2,

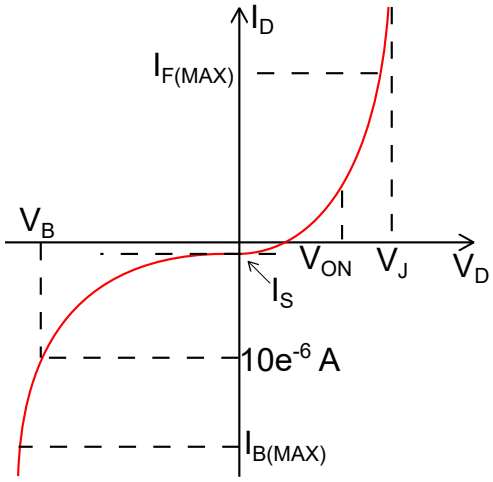

Fig. 6.17: Varactor I-V Relationship

Table 6.2 SMV1405 and SMV2019 Diode Characteristics

Parameter	SMV1405	SMV2019
V_B	30 V	22 V
$I_{B(max)}$	1 mA	0.01 mA
I_S	1e-14 A	1e-14 A
V_J	0.7 V	3.5 V
$I_{F(max)}$	20 mA	100 mA
V_{on}	0.7 V	0.7 V
C_{j0}	2.37 pF V	2.3 pF
M	0.5	1.4

where V_B is the reverse breakdown voltage (typically measured at 10 μA), $I_{B(max)}$ the maximum breakdown current, I_S the reverse saturation (or leakage) current, V_J the junction potential, $I_{F(max)}$ the maximum forward current, V_{on} the ON voltage for a silicon diode, C_{j0} is the diode capacitance at 0 V biasing voltage and M is the grading coefficients.

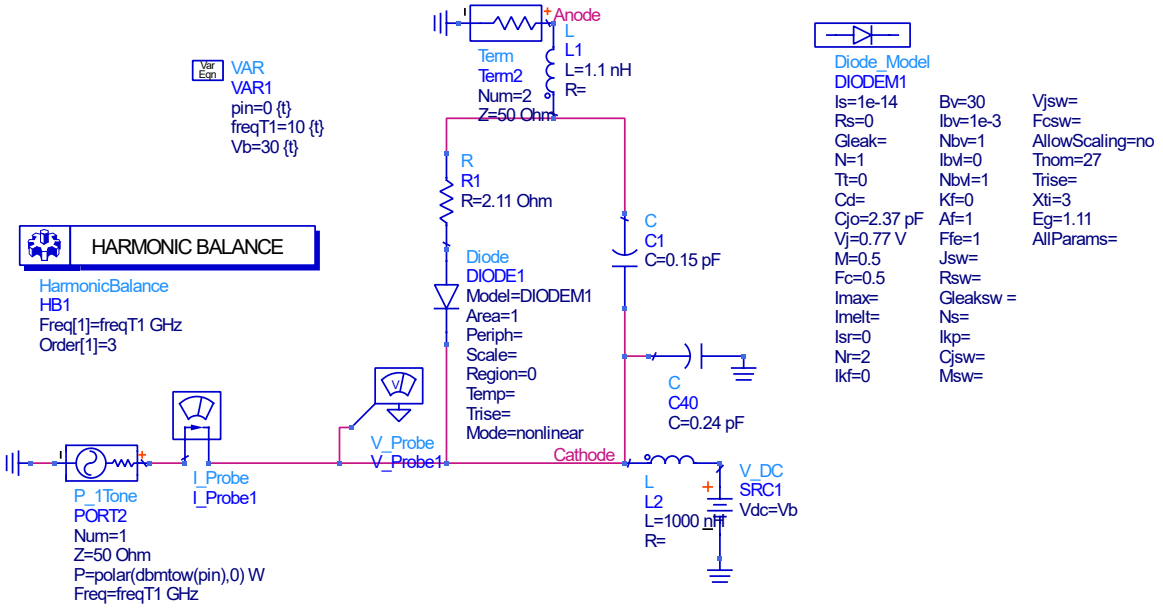

Fig. 6.18: SMV1405 Harmonic Balance Simulation Set-up

A non-linear spice model for each diode is used and its behaviour observed during a harmonic balance simulation in ADS. The simulation involves sweeping the input power of a single tone at an arbitrarily chosen frequency of 10 GHz. The simulation setup for the SMV1405 is shown in Fig. 6.18, while the SMV2019 setup is shown in Fig. 6.19.

The variable *pin* is the input power and the frequency of tone one, or the fundamental frequency is described by $freqT1$. The biasing voltage is equal to Vb. It should be noted that the SMV1405 varactor model includes the package capacitance and inductance, while these components are not required to model the SMV2019.

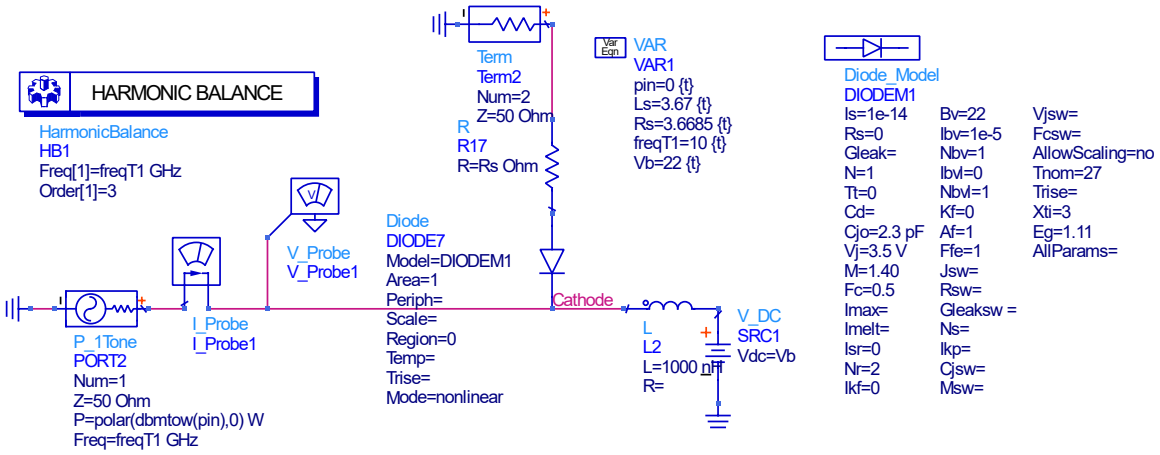

Fig. 6.19: *SMV2019 Harmonic Balance Simulation Set-up*

The fundamental tone, second and third harmonic signal spectrum, as seen at the cathode of the varactor model, for the minimum and maximum biasing voltages of the SMV1405 and SMV2019 varactors, are depicted in Fig. 6.20. For clear interpretation, it is necessary to review the function of each SPICE diode model.

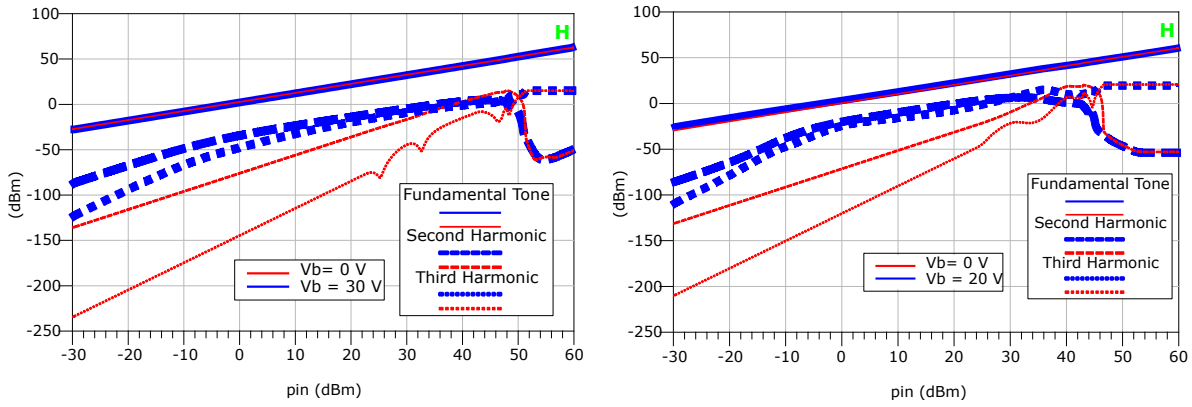

(a) SMV1405 *(b)* SMV2019

Fig. 6.20: *The Non-linear Characteristics of the SMV1405 and SMV2019 Varactors*

The capacitance of a diode is related to the applied voltage (V_D) as follows,

$$C(V_D) = \frac{C_{j0}}{\left(1 - \frac{V_D}{V_J}\right)^M} \tag{6.3.1}$$

For the forward biasing case, where V_D is positive, the V_D/V_J term tends towards zero. Therefore, V_J is the asymptote of the capacitance versus voltage plot in the ON region. The parameter V_J plays a significant role in the non-linearity of the diode in the ON region. However, the exponential coefficient M has the largest influence and determines the rate at which the capacitance tends to infinity.

For the reverse biasing case, the term V_D/V_J becomes negative and so causes the denominator in the capacitance equation to increase. Thus the total diode capacitance tends towards zero. The grading coefficient M once again plays a large role in the OFF state, but here it determines the exponential rate at which the capacitance tends to zero. Therefore, M is the controlling term which largely determines the non-linearity of a diode.

The I-V relationship, given by $I = Z * V$, can be expanded to include the capacitance definition as follows:

$$I(V_D) = j\omega \frac{C_{j0}}{\left(1 - \frac{V_D}{V_J}\right)^M} * V_D \tag{6.3.2}$$

Since the current cannot be infinite, another important factor in both the ON and OFF regions of the diode, is the maximum current rating. The diode models have an explosion current parameter, $Imax$ which is 1 A for the case of both diode models. In the simulation, a warning occurs when the maximum explosion current is exceeded. Thus, if the input power is too large, the diode breaks and this point is reflected in the results.

Since the SMV1405 varactor has a lower grading coefficient and junction potential in comparison to the SMV2019, its I-V relationship is less non-linear than that of the SMV2019 in the OFF and ON region. It is important to consider the maximum forward current in the ON region, since the current cannot become indefinitely large while the diode still remains working.

Referring back to Fig. 6.20, the third harmonic of both components shows rippling behaviour above 25 dBm input power. However, the SMV2019 has less ripples and these ripples begin for a slightly higher input power. The ripples are due to the maximum forward current being exceeded, showing a limit for operation.

In the maximum reverse biasing case for input powers less than -10 dBm, the SMV2019's second and third harmonics have steeper slopes than that of the SMV1405. This difference can largely be attributed to the different grading coefficients (M) which is 9 times larger for the SMV2019.

As discussed previously, it is important to consider the entire structure concerning power limitations and non-linearity. Therefore, the non-linearity of each filter is reviewed in the next section.

6.3.2 Non-linear Filter Properties

In order to determine the power and tuning limitations of each filter due to the varactor non-linearity, harmonic balance (HB) simulations are performed for various tuning stages. The S-parameters for the planar and waveguide filters are used as the base component in each simulation. A single tone signal at f_0, whose power is swept from -30 to 60 dBm, is applied to the input port of each filter (port 1), while the signal spectrum at the output port (port 2) is observed. The varactor models previously used for the filter simulations are replaced with their respective non-linear Spice models. The simulation is performed for the maximum, minimum and centre frequency bands of each filter and only the first three harmonics are considered.

6.3.2.1 Planar Filter

The harmonic balance simulation setup for the suspended substrate filter is shown in Fig. 6.21. The S-parameters for the 17 port planar filter CST EM model is used as the

base component in the simulation. Ports 13 through 17 represent the top of each biasing pin which exits the housing. These ports remain unconnected for this simulation and the biasing voltages are directly applied to each varactor diode model as shown in Fig. 6.21. To ensure that the DC voltage sources are decoupled from the AC signal, a 100 nH inductance is placed in series with each voltage supply.

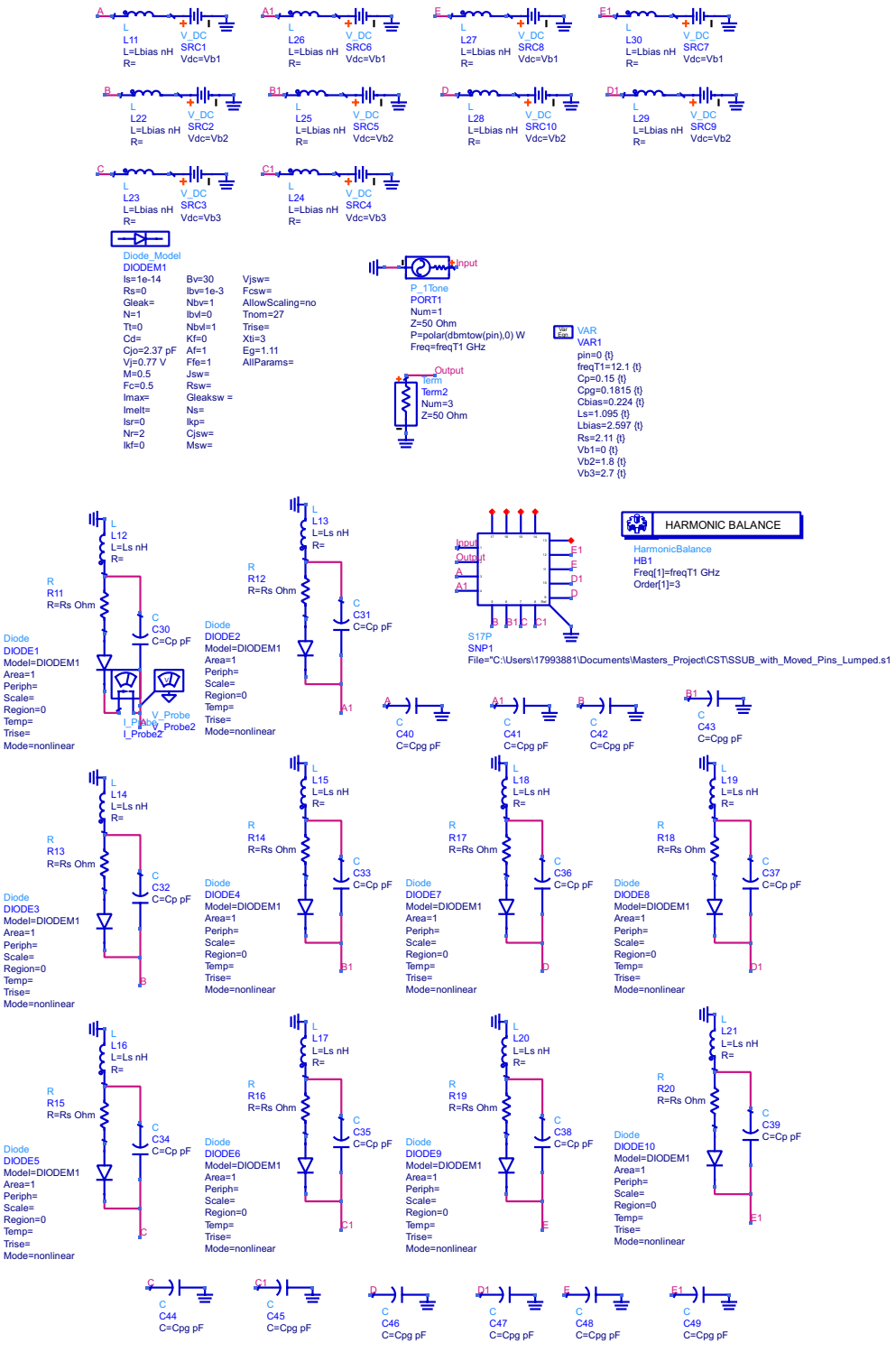

Fig. 6.21: *Planar Filter Harmonic Balance Simulation Setup*

A harmonic balance simulation is performed for three tuning states, labelled State 1, 2 and 3. The circuit parameters for each tuning state is shown in Table 6.3. Since the non-linearity of the filter will have the greatest effect in the filter band, the filter is tuned for the corresponding frequency band using the current Spice models. It should be noted that the filter was tuned for its minimum, maximum and centre frequency band with the current Spice model.

Table 6.3 Planar Filter HB Study Parameters

Response Label	Freq Tone 1 (GHz)	V_{b1} (V)	V_{b2} (V)	V_{b3} (V)	R_s (Ω)
State 1	11.75	0	1.8	2.7	2.11
State 2	11.88	11.1	10.2	6.9	2.60
State 3	12.4	21.6	21.3	29.4	3.38

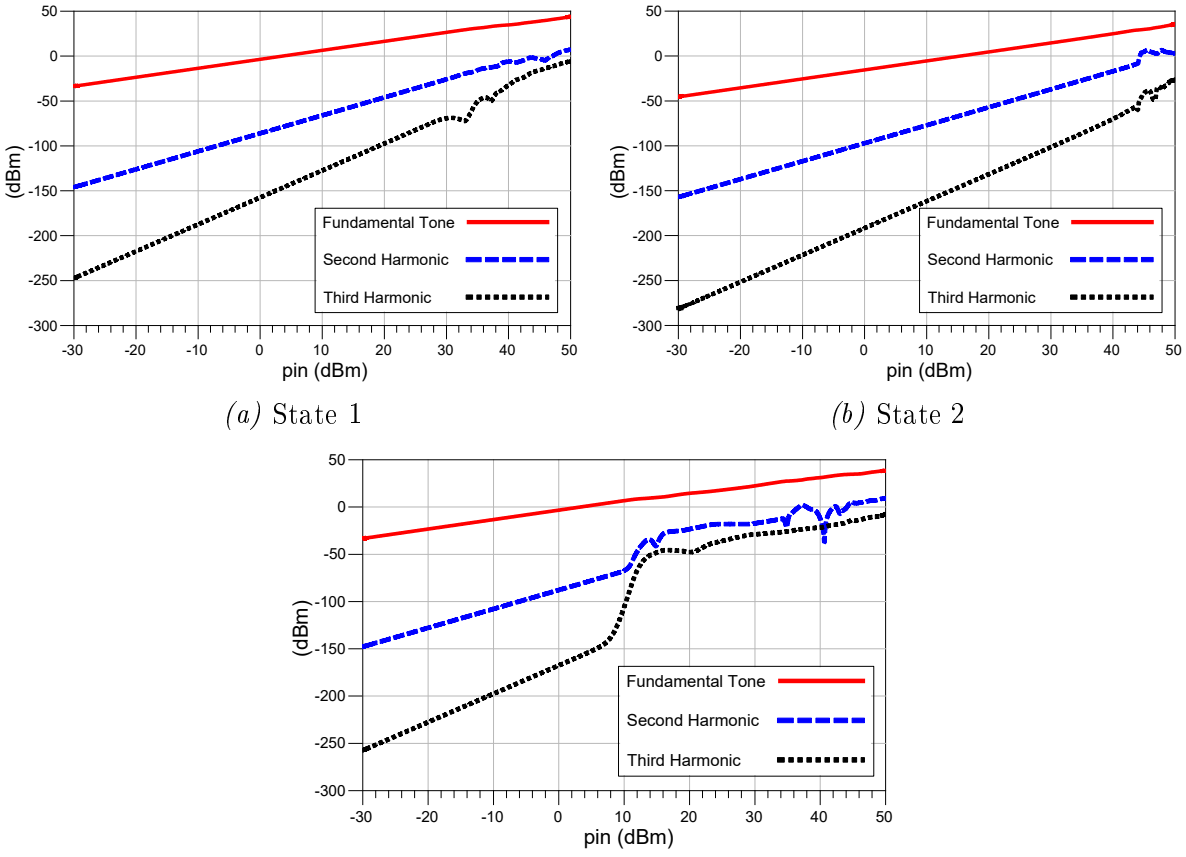

(a) State 1

(b) State 2

(c) State 3

Fig. 6.22: *Planar Filter Harmonic Balance Simulation Results for Various Tuning Stages*

A single tone power supply with a fundamental frequency (Freq Tone 1) specified in the table and a power of *pin* (swept from −30 to 60 dBm) is connected to the input port of the filter. The signal spectrum of the fundamental tone, second and third harmonics for each tuning state is shown in Fig. 6.22.

Figure 6.22c shows that the filter's maximum breakdown current is reached when the input power is approximately 8 dBm. In comparison to the SMV1405 by itself, the filter allows an additional 20 dBm at the input, since only a small percentage of the power is allocated to each diode. In Fig. 6.22a the forward current limit is exceeded when the input power is 30 dBm, visible in the third harmonic. Here only a slight increase in input power is allowed in comparison to the stand-alone diode. It is clear that avalanche has a greater effect on the harmonics than that of forward bias saturation in the case of the planar filter. This is due to the amount of power associated with each varactor and the voltage level of that varactor for the tuned band. This is discussed in detail in Sec. 6.3.2.3. The most linear response is therefore obtained in the region of 10 V biasing voltage. It is evident from the State 3 plot that the maximum reverse biasing voltage limit should be decreased for input powers above 8 dBm.

6.3.2.2 Waveguide Filter

The harmonic balance simulation setup for the evanescent mode waveguide filter is shown in Fig. 6.23. The 8 port S-parameters of the CST simulated waveguide filter structure is imported into ADS and used as the base for the simulation. The SMV2019 varactor Spice models are connected to the open ports (3 through 8) and the biasing voltages are applied directly to each model as shown in Fig. 6.23. As with the planar filter, a large inductance is placed in series with each voltage supply to ensure that the DC voltage sources are decoupled from the AC signal.

The harmonic balance simulation is performed for three tuning states, labelled State 1, 2 and 3. The circuit parameters for each simulation is shown in Table 6.4. It should be noted that the filter was tuned for its minimum, maximum and centre frequency band with the current Spice model.

Table 6.4 Waveguide Filter HB Study Parameters

Biasing Voltage	Freq Tone 1 (GHz)	V_{b1} (V)	V_{b2} (V)	R_s (Ω)
State 1	9.7	0	6	10
State 2	10.65	10	10	5
State 3	11.4	21	18.5	3.7

Once again, a single tone power supply with a fundamental frequency (Freq Tone 1) specified in the table and a power of *pin* (swept from −30 to 60 dBm) is connected to the input port of the filter. The signal spectrum of the fundamental, second and third harmonic for each tuning state is shown in Fig. 6.24.

The filter breakdown point and the forward saturation region is visible in State 3 and State 1 respectively. It is clear that, as in the planar filter case, the avalanche has a greater effect on the non-linearity of the SMV2019 varactor than that of saturation. Since the junction voltage of the diode is specified as 3.5 V, the RF signal still has to add 3.5 V when the diode is biased with 0 V biasing voltage. The most linear response is therefore obtained in the region of 10 V biasing voltage. It is evident from the State 3 plot that the maximum reverse biasing voltage limit should be decreased for input powers above 2 dBm.

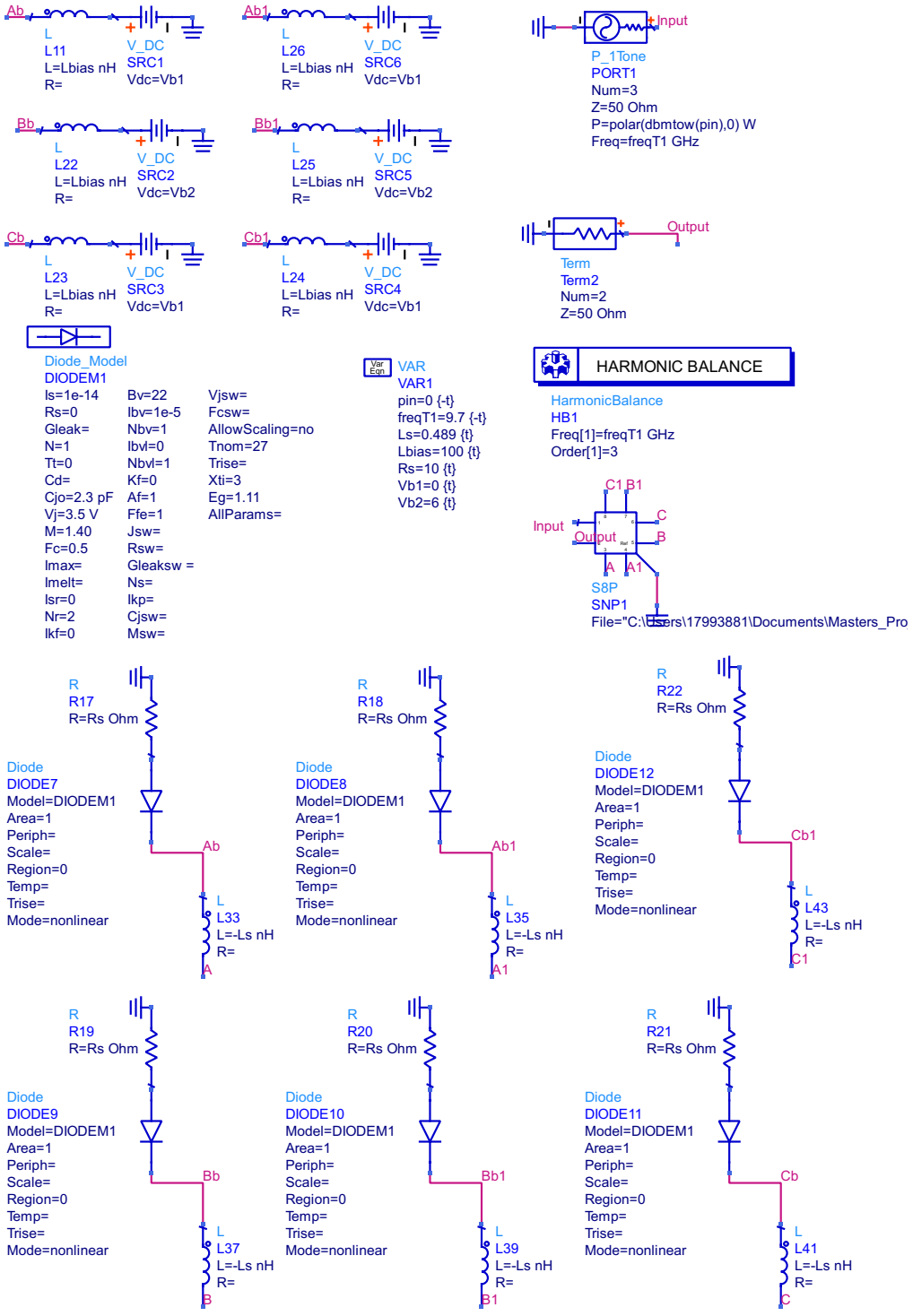

Fig. 6.23: *Waveguide Filter Harmonic Balance Simulation Setup*

6.3.2.3 Comparison between the Planar and Waveguide Non-linearity results

The non-linearity for each tuning case is dependent on the varactor junction potential and grading coefficient, the voltage level applied to each resonator, the percentage power dissipated in the varactors of each resonator and the input power.

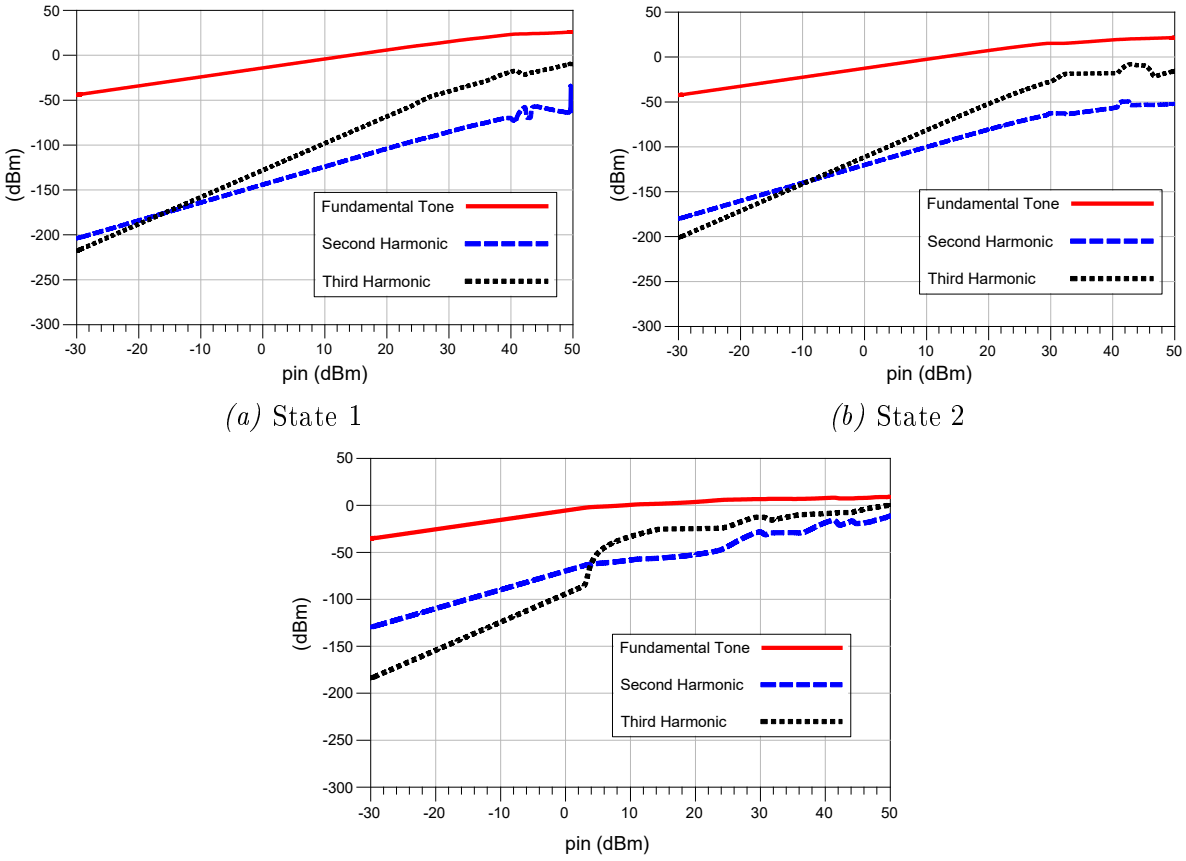

(a) State 1 *(b)* State 2

(c) State 3

Fig. 6.24: *Waveguide Filter Harmonic Balance Simulation Results for Various Tuning Stages*

Referring back to the power dissipation plots from Sec. 6.1, the first resonator from the input contributed to the highest varactor power dissipation in both the planar and waveguide filters. While for the planar filter the power dissipation remained more or less constant regardless of the tuning band, the waveguide filter had a large fluctuation.

The highest power dissipation observed in the varactors of the first waveguide resonator occurred at the lowest tuned frequency, State 3 response. For State 1 of each filter, the first resonator in the planar structure dissipated 15 % less power at the centre of the band than that of the waveguide structure. This means that the forward biasing breaking point for the waveguide filter for this band is expected to occur much faster than that of the planar structure.

For the highest tuned frequency band, the planar and waveguide filter's first resonators had approximately the same power dissipation. If this was the only factor to consider, these filters would have very similar non-linearity for State 3.

The different voltage levels of the varactors in each tuning case plays a large role, since it determines how much RF voltage needs to be added to push the varactor into breakdown. For the planar filter's State 3 response, the maximum reverse bias is only applied to the third resonator, while for the waveguide's State 3 response it is applied to the first. Since the third resonator has considerably less power dissipation than the first and second resonators as seen in Sec. 6.1, the waveguide filter should break before the planar filter for the same input power.

From the harmonic balance simulation for both filters it is clear that the waveguide

filter is less non-linear for the low input powers and low frequencies, but more non-linear for the high frequencies and high input powers. Apart from the grading coefficient, the waveguide filter is also more non-linear in the high frequency due to the voltage level at the first resonator, and more non-linear at the low frequencies due to the power dissipation in the varactors.

Lastly it is important to remember that the simulations performed in this section do not take into account the non-linearity of the filter structure itself. Therefore, the planar and waveguide harmonic balance simulations assume a linear filter structure with non-linear components. In reality, each structure would also have an input power limit associated with the heating of the material.

6.4 Conclusion

In this chapter a comparison between the planar and waveguide filters is drawn in terms of the power dissipation in the varactors, the thermal resistance of each varactor mount and the non-linearity of the filter due to the varactor non-linearity.

The power dissipation study involved tuning all filters to their maximum and minimum measured centre frequencies and determining the percentage power dissipated in each varactor. The results show that the planar filter has more or less constant power dissipation in the tuning range, while the waveguide filter's maximum dissipation is at the lowest tuned centre frequency. The waveguide filter structure was shown to have better symmetry out of band between the two ports of a resonator than that of the planar filter. The study also showed that the planar filter structure contributes approximately 13 times more to dissipated power than that of the waveguide structure.

The thermal property study discussed the heat sinking properties of each structure. The total thermal resistance is a combination of the diode junction to case thermal resistance as well as the case to heat sink and the heat sink to ambient thermal resistances. Under the assumption that the thermal resistance between the heat sink and ambient is negligible and that the diode junction to case thermal resistance is the same for both diodes, the difference in the thermal resistance between the planar and waveguide structures is dependent on the thermal resistance from case to heat sink. The result shows that the planar structures case to heat sink thermal resistance is 2.7 times that of the waveguide structure if the heat sink's conductivity is the same.

Lastly this chapter includes a study on the non-linearity of each filter due to the non-linearity of the varactors. The non-linearity for each tuning case is dependent on the varactor junction potential and grading coefficient, the voltage level applied to each resonator, the percentage power dissipated in the varactors of each resonator and the input power. Apart from the grading coefficient, the waveguide filter is also more non-linear in the high frequency due to the voltage level at the first resonator, and it breaks faster at the low frequencies due to the power dissipation in the varactors.

Considering all the factors above, the planar filter's entire tuning range can be used for input powers up to 8 dBm while the waveguide filter can be used to 2 dBm. If the waveguide filter is only used up to its 10 V tuning point, input powers of over 20 dBm may be possible while still providing approximately 1 GHz of centre frequency tuning.

Chapter 7

Conclusion

The work contained in this dissertation includes the full design cycle of two tunable filters with completely different structures, one planar and one waveguide, designed from the same basic principles. Both are designed for X-band tunable narrow-band Chebychev bandpass responses with good out-of-band attenuation, centre frequency tunability, a miniaturised structure and good power handling capabilities. Two new filter structures for tunable filters at X-band are presented in this dissertation:

- a varactor-tuned suspended substrate filter with spatially decoupled vertical biasing pins, and
- a waveguide-mounted varactor-tuned evanescent mode waveguide filter

Planar Filter

A biasing solution is provided for coupled $\lambda/2$ resonators, such as in a staircase topology. The biasing structure consists of vertical pins, placed at a point of zero RF voltage and orientated in such a way that the total coupled magnetic field cancels to zero. The pins are of such a length that they have inductive properties, while the exit hole in the roof of the enclosure forms a capacitance with the wire. Therefore, the need for any additional biasing circuitry is omitted.

The biasing solution is applied to a 5^{th} order varactor-tuned staircase filter implemented on suspended substrate. The manufactured filter includes stepped side walls to suppress higher order modes inside of the enclosure. The filter achieved a centre frequency tunability of $11.75-12.15$ GHz with an absolute bandwidth of $420-510$ MHz ($3.58-4.23$ % relative 3-dB bandwidth). The insertion loss was less than 6 dB across the entire tuning range.

In comparison to the filters presented in Ch. 2, the suspended substrate varactor-tuned filter achieved competitive centre frequency tunability for narrow-band filters. Though the insertion loss was larger on average, consideration should be given to the operating frequency and the tuning components used. Implementing low-loss tuning components such as MEMS, may significantly improve the insertion loss of the suspended substrate design, but there are trade-offs with cost, component availability and large required biasing voltages.

Waveguide Filter

The evanescent mode tunable waveguide filter design presented in Ch. 5 consists of an in waveguide-mounted back-to-back varactor structure which builds on the PIN-diode

waveguide switch from [14] and the theory by Craven and Mok in [54].

The structure consists of a central ground plate, a varactor mounted on top and below the plate, biasing wires, and two mechanical tuning screws. The topology is symmetrical about the vertical centre of the waveguide cavity. The tuning screws create a rough tuning capability while the varactors enable fine tuning. The electrical tunability is highly dependent on the size of the air gaps between the varactors and the tuning screws. For a larger air gap, a smaller tuning range is realisable and vice versa.

The evanescent mode tuning structure was implemented in a 3^{rd} order narrow band filter. The total size of the evanescent mode filter section is 22.8 mm x 10.1 mm. The filter measurements achieved a centre frequency tunability of $9.8 - 11.1$ GHz, a 3-dB relative bandwidth of $7.06 - 10.55$ % and a maximum insertion loss of $3 - 10.1$ dB. The increase in insertion loss was found to be a product of the hyperabrupt varactor series resistance in Ch. 6. Therefore, the filter may be improved by selecting a tuning component with a more stable and lower series resistance.

In comparison to the filters presented in Ch. 2, the varactor-tuned evanescent mode waveguide filter achieved a larger tuning range than most but at a cost of larger insertion loss in the lower tuning range. In terms of size the evanescent mode waveguide filter reached the expectations of being smaller than its waveguide counterparts, but larger than the SIW structures. However, the presented in-waveguide mounted varactor-tuned evanescent mode filter has the advantage of post-production tuning, and no external circuitry apart from the biasing wires.

Although one of the main advantages of waveguide structures over planar structures is that high quality factors may be realised, this advantage is not evident when considering the performance of the designs presented in this dissertation. The lowered quality factor in the waveguide shows that the varactor power dissipation has detrimental effects on the passband, especially in the lower tuning range, and is the overriding factor for the decrease in performance. In order to exploit the waveguide structure's high Q advantage, varactors with low series resistance for the entire tuning range should be utilised. Unfortunately such varactors are not yet available for X-band frequencies.

Thermal Properties, Power Handling and Non-Linearity

From Ch.6, it is clear that the varactors are responsible for the rounded shoulders in the filter response as well as the insertion loss performance of the filter. The non-linearity of each filter due to the varactors were shown to be dependent on the varactor junction potential, grading coefficient, the applied DC voltage, the power dissipated in each resonator, and the RF signal power. Though it is not possible to compare the planar and waveguide structures directly on all fronts, the thermal resistance calculations suggest that the waveguide structure provides a better heat sink for the varactors, and thus can contribute more towards high power handling than that of the planar structure.

In terms of the non-linearity simulations for each filter, the waveguide filter was less non-linear for input powers below 0 dBm. The non-linearity of the planar and waveguide filters at their lowest tuned centre frequency, limits the maximum input power to 8 dBm for the planar filter and 2 dBm for the waveguide filter. However, consideration should be given to the tuning range, the power dissipation, applied biasing voltage and non-linearity of each varactor. By reducing the tuning range of the waveguide filter to a maximum applied biasing voltage of 10 V, the input power limitation due to the non-linearity of the varactors may be increased to 20 dBm, while still maintaining around 1

GHz tuning range. Similarly the non-linearity of the planar filter for higher powers may be improved by limiting the tuning range.

Suggestions for Future Work

The two filters presented in this dissertation provide electronically frequency tunable, cost effective, miniaturised solutions, with simplified biasing methods and competitive performances for their individual classes of filter. Future extensions of these designs could include the following:

- Bandwidth and frequency tunable suspended substrate filters through the implementation of additional coupling control elements.

- Improved filter performance in both the planar and waveguide filters through the implementation of alternative tuning components such as MEMS varactors.

- Improved power handling capabilities in both the planar and waveguide filters through the implementation of alternative tuning components such as varactors with lower series resistance or high power MEMS varactors.

- Implementation of the spatially decoupled biasing method on microstrip and stripline structures.

Appendix A

TRL Calibration

Thru-Reflect-Line or TRL calibration technique is a method for calibrating the dual six-port network analyser as described in [57]. The TRL technique can also be used as a post-measurement supplementary calibration. Though many systems nowadays have electronic calibration and custom calibration kits for different types of measurements, the calibration kits are quite expensive and do not always take into account the transitions required for the measurement. For example, to determine the scattering parameters of a single component, such as the SMV1405 varactor used in the planar design, the component often needs to be mounted onto a substrate with transitions to SMA connectors prior to measurement. The measurement thus includes the component's properties, the substrate mount properties, and the SMA connector properties. Thus, one of the main advantages of post-measurement TRL calibration is that any measurement plane can be defined and the desired properties extracted. This chapter follows the work presented in [57] and describes how it is applied for this project.

A.1 Theory

This section covers post-measurement calibration for characterising the two-port parameters of a device-under-test (DUT). The calibration technique requires three standards (thru, reflect, line), and a DUT measurement. The post-measurement TRL calibration can be used to aid in the classification a DUT, where it might not be possible to manually calibrate up to the desired measurement plane.

The detector planes are defined where the physical calibration and measurement occurs. For a post-measurement TRL calibration, three two-port measurements (thru, reflect, line), as well as a two-port measurement of the DUT, are required. In [57], the thru, reflect and line measurements make up three fictitious two-port systems. Each fictitious two-port system also include two error boxes A and B, as shown in Fig. A.1.

The reflect standard consists of a non-ideal reflect measurement, the line standard consist of an extended or delay measurement, and the thru standard consists of a connection between the two ports. The line length should not be resonant at the measured frequency. One of the primary differences between the TRL technique and the thru-short-delay (TSD) method is that the reflection coefficient of the load is unknown for the TRL calibration.

The measurement planes are separated from the physical detector planes by two error boxes, one on each side as shown in Fig. A.1. The error box properties are extracted by

using the thru, line and reflect two-port measurements. The ability to take into account certain errors post measurement is the basis for TRL calibration.

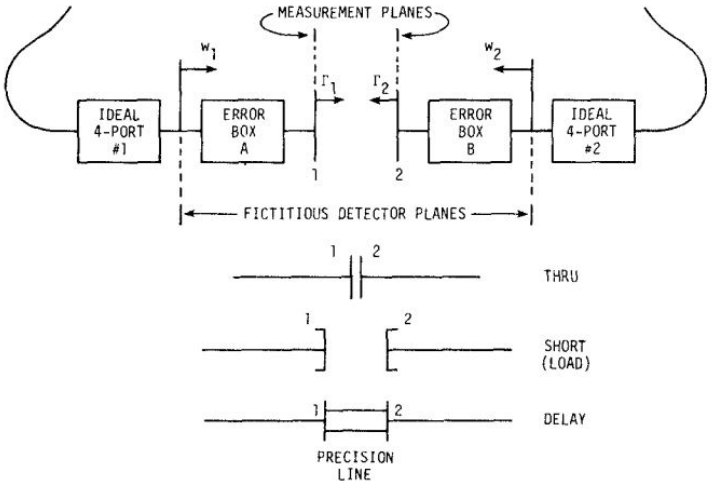

Fig. A.1: *TRL Calibration: Detector plane to Measurement plane [57]*

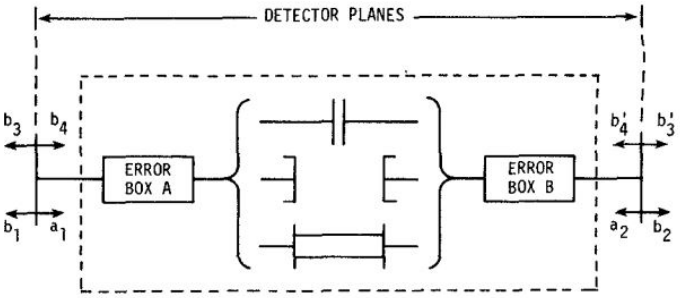

Fig. A.2: *Defining Error Boxes for TRL Calibration [57]*

Given the two-port S-parameters of the thru, reflect, and line standards, the scattering parameters for three fictitious two-ports can be obtained, as shown in Fig. A.2. In a two-port system, the S-parameters are related to the emergent wave amplitudes (b_1 and b_2) and the incident waves (a_1 and a_2), by the following equations,

$$\begin{aligned} b_1 &= S_{11}a_1 + S_{12}a_2 \\ b_2 &= S_{21}a_1 + S_{22}a_2 \end{aligned} \tag{A.1.1}$$

The reflection coefficients are introduced as follows,

$$\begin{aligned} w_1 &= b_1/a_1 \\ w_2 &= b_2/a_2 \end{aligned} \tag{A.1.2}$$

Introducing the variable Δ, equation A.1.1 can be manipulated into the following form:

$$\begin{bmatrix} b_1 \\ a_1 \end{bmatrix} = \frac{1}{S_{21}} \begin{bmatrix} -\Delta & S_{11} \\ -S22 & 1 \end{bmatrix} \begin{bmatrix} a_2 \\ b_2 \end{bmatrix} = R \begin{bmatrix} a_2 \\ b_2 \end{bmatrix} \tag{A.1.3}$$

for,

$$\Delta = S_{11}S_{22} - S_{12}S_{21} \tag{A.1.4}$$

where R is known as the wave cascading matrix. For a system of two or more two-port networks, R simply becomes the product of each individual wave cascading matrix. The thru and line measurements have the following R matrices when taking the error boxes into account:

$$R_{thru} = R_A R_B \tag{A.1.5}$$

$$R_{delay} = R_A R_{Line} R_B \tag{A.1.6}$$

The reflect measurement can be used directly to provide the reflection coefficients at the detector planes,

$$w_1 = S_{11_{reflect}} \tag{A.1.7}$$

$$w_2 = S_{22_{reflect}} \tag{A.1.8}$$

Combining equations A.1.5 and A.1.6 to eliminate R_B, results in

$$R_A R_{delay} = R_A R_{Line} R_{thru} \tag{A.1.9}$$

Defining $T = R_{delay}R_{thru}^{-1}$ and substituting into the equation above gives,

$$R_A T = R_A R_{Line} \tag{A.1.10}$$

Assuming the line is ideal and no reflection is added, R_{Line} can be described as follows:

$$R_{Line} = \begin{bmatrix} e^{-\gamma l} & 0 \\ 0 & e^{\gamma l} \end{bmatrix} \tag{A.1.11}$$

Defining R_A and T with elements $r_{A_{ij}}$ and tij respectively, provides the following matrix equation

$$\begin{bmatrix} t_{11} & t_{12} \\ t_{21} & t_{22} \end{bmatrix} \begin{bmatrix} r_{A_{11}} & r_{A_{12}} \\ r_{A_{21}} & r_{A_{22}} \end{bmatrix} = \begin{bmatrix} r_{A_{11}} & r_{A_{12}} \\ r_{A_{21}} & r_{A_{22}} \end{bmatrix} \begin{bmatrix} e^{-\gamma l} & 0 \\ 0 & e^{\gamma l} \end{bmatrix} \tag{A.1.12}$$

Expanding both sides gives the following set of equations:

$$t_{11}r_{A_{11}} + t_{12}r_{A_{21}} = r_{A_{11}}e^{-\gamma l} \tag{A.1.13}$$

$$t_{21}r_{A_{11}} + t_{22}r_{A_{21}} = r_{A_{21}}e^{-\gamma l} \tag{A.1.14}$$

$$t_{11}r_{A_{12}} + t_{12}r_{A_{22}} = r_{A_{12}}e^{-\gamma l} \tag{A.1.15}$$

$$t_{21}r_{A_{12}} + t_{22}r_{A_{22}} = r_{A_{22}}e^{-\gamma l} \tag{A.1.16}$$

Relating equations A.1.13 to A.1.14 and A.1.15 to A.1.16 results in two quadratic equations with the same coefficients but different variables as shown below.

$$\begin{aligned} t_{21}(\frac{r_{A_{11}}}{r_{A_{21}}})^2 + (t_{22} - t_{11})(\frac{r_{A_{11}}}{r_{A_{21}}}) - t_{12} = 0 \\ t_{21}(\frac{r_{A_{12}}}{r_{A_{22}}})^2 + (t_{22} - t_{11})(\frac{r_{A_{12}}}{r_{A_{22}}}) - t_{12} = 0 \end{aligned} \tag{A.1.17}$$

There are two possible roots. Following the discussion in [57], it is found that the roots $r_{A_{11}}/r_{A_{21}}$ and $r_{A_{12}}/r_{A_{22}}$ are easily distinguishable and that the root with the smallest absolute value is always assigned to $r_{A_{12}}/r_{A_{22}}$.

Through combining the equations A.1.16 and A.1.14, an equation for the line characteristic is obtained:

$$e^{2\gamma l} = \frac{t_{21}(\frac{r_{A_{12}}}{r_{A_{22}}}) + t_{22}}{t_{21}(\frac{r_{A_{21}}}{r_{A_{11}}}) + t_{11}} \tag{A.1.18}$$

By taking the determinant of eq. A.1.10, the following results

$$t_{11}t_{22} - t_{21}t_{12} = 1 \tag{A.1.19}$$

Introducing the variables a, b and c as $r_{A_{11}}/r_{A_{22}}$, $r_{A_{12}}/r_{A_{22}}$ and $r_{A_{21}}/r_{A_{22}}$ respectively, the two roots of the quadratic equation become b and c/a.

Redefining R_{thru} and R_B as follows,

$$R_{thru} = \rho_{22}\begin{bmatrix}\alpha & \beta\\ \gamma & 1\end{bmatrix} \tag{A.1.20}$$

$$R_B = g\begin{bmatrix}d & e\\ f & 1\end{bmatrix} \tag{A.1.21}$$

equation A.1.5 becomes,

$$r_{A_{22}}\begin{bmatrix}a & b\\ c & 1\end{bmatrix}\rho_{22}\begin{bmatrix}\alpha & \beta\\ \gamma & 1\end{bmatrix} = g\begin{bmatrix}d & e\\ f & 1\end{bmatrix} \tag{A.1.22}$$

Solving for the elements in R_{thru}, yields

$$\gamma = \frac{f - dc/a}{1 - ec/a} \tag{A.1.23}$$

$$\beta/\alpha = \frac{e - b}{d - bf} \tag{A.1.24}$$

$$a\alpha = \frac{d - bf}{1 - ec/a} \tag{A.1.25}$$

From the measured thru standard, the R_{thru} matrix elements are known,

$$\begin{aligned} g &= \frac{1}{S_{21_{thru}}}\\ d &= -(S_{11_{thru}}S_{22_{thru}} - S_{21_{thru}}S_{12_{thru}})\\ e &= S_{11_{thru}}\\ f &= -S_{22_{thru}} \end{aligned} \tag{A.1.26}$$

In order to split the ratio c/a, the reflection coefficient at the first detector plane is revisited. Since,

$$w_1 = \frac{a\Gamma_{load} + b}{c\Gamma_{load} + 1} \tag{A.1.27}$$

the variable a can be defined as

$$a = \frac{w_1 - b}{\Gamma_{load}(1 - w_1 c/a)} \tag{A.1.28}$$

A similar equation can be obtained for α using the reflection coefficient at the second detector plane,

$$\alpha = \frac{w_2 + \gamma}{\Gamma_{load}(1 + w_2 \beta/\alpha)} \tag{A.1.29}$$

By using the equations above for a and α, the unknown Γ_{load} can be eliminated,

$$a/\alpha = (\frac{w_1 - b}{1 - w_1 c/a})(\frac{1 + w_2 \beta/\alpha}{w_2 + \gamma}) \tag{A.1.30}$$

Since the ratio of c/a is known from the quadratic solution, multiplying by the equation describing $a\alpha$, provides a solution for a and α:

$$a = \sqrt{\frac{(w_1 - b)(1 + w_2 \beta/\alpha)(d - bf)}{(w_2 + \gamma)(1 - w_1 c/a)(1 - ec/a)}} \tag{A.1.31}$$

$$\alpha = \frac{d - bf}{a(1 - ec/a)} \tag{A.1.32}$$

Finally, both R_A, R_B can now be taken into account to obtain the calibrated R-matrix for the device.

$$R_m = R_A R_{cal} R_B \tag{A.1.33}$$

$$R_{cal} = \frac{1}{\rho_{22} r_{22}(\alpha - \gamma\beta)(a - bc)} \begin{bmatrix} 1 & -b \\ -c & a \end{bmatrix} \begin{bmatrix} R_{m11} & R_{m12} \\ R_{m21} & R_{m22} \end{bmatrix} \begin{bmatrix} 1 & -\beta \\ -\gamma & \alpha \end{bmatrix} \tag{A.1.34}$$

From R_{cal} equation A.1.3 may be used to define the scattering parameters as follows:

$$\begin{aligned} S_{21cal} &= \frac{1}{R_{22cal}} \\ S_{22cal} &= -S_{21cal} R_{21cal} \\ S_{11cal} &= S_{21cal} R_{12cal} \\ S_{12cal} &= \frac{S_{11cal} S_{22cal}}{S_{21cal}} - R_{11cal} \end{aligned} \tag{A.1.35}$$

Therefore, it is shown that by using the TRL calibration method the scattering parameters of a device under test can successfully be extracted.

A.2 Manufactured TRL standards for the SMV1405 varactor

The TRL standards are designed and simulated in CST, and consist of four microstrip substrates. The milled standards are shown in Fig. A.3.

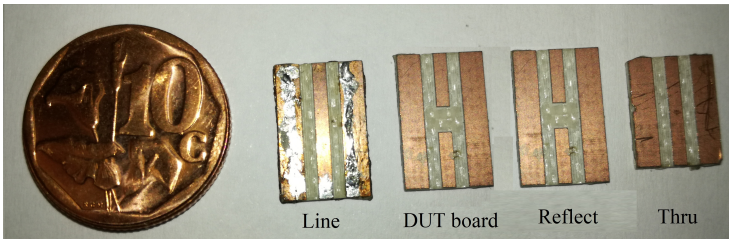

Fig. A.3: *Manufactured TRL standards Prior Enclosure*

An SMA connector is attached to the microstrip lines and an enclosure placed around to prevent any unwanted and varying interference and coupling. The SMV1405 is mounted on the DUT board shown in Fig. A.3. The spacing between the microstrip lines on the DUT board are the same as the length of the varactor.

The measured versus simulated responses for each standard are shown in Fig. A.4.

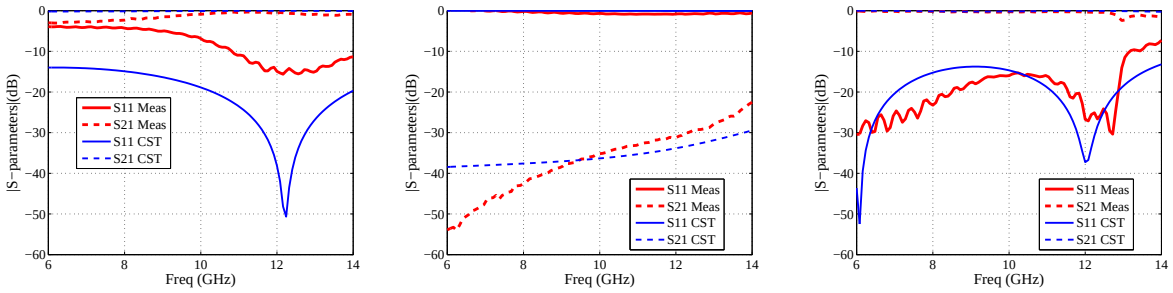

(a) Thru *(b)* Open *(c)* Line

Fig. A.4: *Simulated vs Measured TRL Standards*

Bibliography

[1] G. L. Matthaei, L. Young, and E. M. T. Jones, *Microwave Filters, Impedance-matching Networks, and Coupling Structures.* McGraw-Hill Book Company Inc., 1964.

[2] A. S. Hussaini, R. Abd-Alhameed, and J. Rodriguez, "Tunable RF filters: Survey and beyond," in *2011 18th IEEE International Conference on Electronics, Circuits, and Systems*, Dec 2011, pp. 512–515.

[3] A. C. Guyette, "Intrinsically Switched Varactor-Tuned Filters and Filter Banks," *IEEE Transactions on Microwave Theory and Techniques*, vol. 60, no. 4, pp. 1044–1056, April 2012.

[4] A. C. Baynham and M. R. B. Dunsmore, "High Power Electronically Tunable Microwave Filters," in *1971 2nd European Microwave Conference*, vol. 2, Aug 1971, pp. 1–4.

[5] S. Courreges, Z. Zhao, K. Choi, A. Hunt, and J. Papapolymerou, "A quasi-elliptic ferroelectric tunable filter for X-band applications," in *2009 European Microwave Conference (EuMC)*, Sept 2009, pp. 1409–1412.

[6] I. Hunter and J. Rhodes, "Electronically Tunable Microwave Bandpass Filter," *IEEE Transactrions on Microwave Theory and Techniques*, vol. MTT-30, no. 9, September 1982.

[7] L. Lin, C. T. C. Nguyen, R. T. Howe, and A. P. Pisano, "Microelectromechanical filters for signal processing," in *[1992] Proceedings IEEE Micro Electro Mechanical Systems*, Feb 1992, pp. 226–231.

[8] L. P. B. Katehi, G. M. Rebeiz, and C. T. C. Nguyen, "MEMS and Si-micromachined components for low-power, high-frequency communications systems," in *1998 IEEE MTT-S International Microwave Symposium Digest (Cat. No.98CH36192)*, vol. 1, June 1998, pp. 331–333.

[9] A. R. Brown and G. M. Rebeiz, "A varactor-tuned RF filter," *IEEE Transactions on Microwave Theory and Techniques*, vol. 48, no. 7, pp. 1157–1160, Jul 2000.

[10] A. Toorian, K. Diaz, and S. Lee, "The CubeSat Approach to Space Access," in *2008 IEEE Aerospace Conference*, March 2008, pp. 1–14.

[11] R. R. Mansour, F. Huang, S. Fouladi, W. D. Yan, and M. Nasr, "High-Q Tunable Filters," *IEEE Microwave Magazine for the Microwave and Wireless Engineer*, vol. 46, pp. 70–82, July/August 2014.

[12] Y. M. Chen, S. F. Chang, W. Y. Chen, and B. J. Huang, "Packaged Tunable Bandpass Filters Based on Varactor-Loaded Spiral Combline Topology," *IEEE Microwave Magazine for the Microwave and Wireless Engineer*, vol. 12, pp. 123–127, 2012.

[13] E. Botes and P. Meyer, "Spatially decoupled varactor biasing for a tunable staircase filter," *IET Microwaves, Antennas Propagation*, vol. 11, no. 1, pp. 10–16, 2017.

[14] T. Sickel, "Tunable Evanescent Mode X-band Waveguide Switch," Ph.D. dissertation, Stellenbosch University, 2006.

[15] D. Peroulis, E. Naglich, M. Sinani, and M. Hickle, "Tuned to Resonance," *IEEE Microwave Magazine for the Microwave and Wireless Engineer*, vol. 46, pp. 55–69, July/August 2014.

[16] Insolink, Inc., *SMV2019 to SMV2023 Series: Hermetic Ceramic Packaged Silicon Hyperabrupt Junction Varactor*, October 2014, Data Sheet.

[17] Skyworks Solution Inc., *Varactor Diodes*, August 2008, Application Note.

[18] S. Hollos and R. Hollos, "Using Varactors," *Exstrom Laboratories LLC*, 2001.

[19] H. Zareie and G. M. Rebeiz, "High-Power RF MEMS Switched Capacitors Using a Thick Metal Process," *IEEE Transactions on Microwave Theory and Techniques*, vol. 61, no. 1, pp. 455–463, Jan 2013.

[20] A. Ziaei, S. Bansropun, P. Martins, and M. L. Baillif, "Fast high power capacitive RF-MEMS switch for X-Band applications," in *2015 45th European Solid State Device Research Conference (ESSDERC)*, Sept 2015, pp. 153–155.

[21] G. M. Rebeiz and J. B. Muldavin, "RF MEMS switches and switch circuits," *IEEE Microwave Magazine*, vol. 2, no. 4, pp. 59–71, Dec 2001.

[22] N. Mohottige, D. Budimir, and C. Panagamuwa, "Optically Reconfigurable E-plane Waveguide Resonators and Filters," *Proceedings of the 43rd European Microwave Conference*, 2013.

[23] J. Nath, D. Ghosh, J. P. Maria, A. I. Kingon, W. Fathelbab, P. D. Franzon, and M. B. Steer, "An electronically tunable microstrip bandpass filter using thin-film Barium-Strontium-Titanate (BST) varactors," *IEEE Transactions on Microwave Theory and Techniques*, vol. 53, no. 9, pp. 2707–2712, Sept 2005.

[24] A. Abbaspour-Tamijani, L. Dussopt, and G. M. Rebeiz, "Miniature and tunable filters using MEMS capacitors," *IEEE Transactions on Microwave Theory and Techniques*, vol. 51, no. 7, pp. 1878–1885, July 2003.

[25] M. A. El-Tanani and G. M. Rebeiz, "High-Performance 1.5-2.5-GHz RF-MEMS Tunable Filters for Wireless Applications," *IEEE Transactions on Microwave Theory and Techniques*, vol. 58, no. 6, pp. 1629–1637, June 2010.

[26] Y. H. Cho and G. M. Rebeiz, "Two- and Four-Pole Tunable 0.7-1.1-GHz Bandpass-to-Bandstop Filters With Bandwidth Control," *IEEE Transactions on Microwave Theory and Techniques*, vol. 62, no. 3, pp. 457–463, March 2014.

[27] J. Cai, J. X. Chen, X. F. Zhang, Y. J. Yang, and Z. H. Bao, "Electrically varactor-tuned bandpass filter with constant bandwidth and self-adaptive transmission zeros," *IET Microwaves, Antennas Propagation*, vol. 11, no. 11, pp. 1542–1548, 2017.

[28] X. Huang, Q. Feng, L. Zhu, and Q. Xiang, "A constant absolute bandwidth Tunable Filter Using Varactor-Loaded Open-Loop Resonators," *Proc. 2013 Asia-Pacific Microwave Conference*, vol. 61, pp. 872–874, 2013.

[29] Q. Xiang, Q. Feng, X. Huang, and D. Jia, "Electrically Tunable Microstrip LC Bandpass Filters With Constant Bandwidth," *IEEE Transactions on Microwave Theory and Techniques*, vol. 61, pp. 1124–1130, March 2013.

[30] J. S. Sun, N. Kaneda, Y. Baeyens, T. Itoh, and Y.-K. Chen, "Multilayer Planar Tunable Filter With Very Wide Tuning Bandwidth," *IEEE Transactions on Microwave Theory and Techniques*, vol. 59, pp. 2864–2871, November 2011.

[31] S. Sirci, J. D. Martinez, M. Taroncher, and V. E. Boria, "Varactor-Loaded Continuously Tunable SIW Resonator for Reconfigurable Filter Design," *Proc. 41st European Microwave Conference, Manchester, UK*, pp. 436–439, 10-13 October 2011.

[32] M. W. Young, S. Yong, and T. Bernhard, "A Miniaturized Frequency Reconfigurable Antenna With Single Bias, Dual Varactor Tuning," *IEEE Transactions on Antennas and Propagation*, vol. 63, pp. 946–951, 2015.

[33] I. Flammia, B. Khani, S. Arafat, and A. Stohr, "60 GHz grounded-coplanar-waveguide-to-substrate-integrated-waveguide transition for RoF transmitters," *Electronics Letters*, vol. 50, pp. 34–35, 2 January 2014.

[34] S. J. Park, I. Reines, C. Patel, and G. M. Rebeiz, "High-Q RF-MEMS 4-6-GHz Tunable Evanescent-Mode Cavity Filter," *IEEE Transactions on Microwave Theory and Techniques*, vol. 58, no. 2, pp. 381–389, Feb 2010.

[35] A. L. Amadjikpe, D. J. Chung, S. Courreges, P. Eudeline, A. Ziaei, and J. Papapolymerou, "Two-pole digitally tunable evanescent-mode waveguide narrow-band filter with radio frequency micro-electromechanical systems switches," *IET Microwaves, Antennas Propagation*, vol. 5, no. 4, pp. 393–401, March 2011.

[36] S. Fouladi, F. Huang, W. D. Yan, and R. R. Mansour, "High-Q Narrowband Tunable Combline Bandpass Filters Using MEMS Capacitor Banks and Piezomotors," *IEEE Transactions on Microwave Theory and Techniques*, vol. 61, no. 1, pp. 393–402, Jan 2013.

[37] J. H. Dang, R. C. Gough, A. M. Morishita, A. T. Ohta, and W. A. Shiroma, "A tunable x-band substrate integrated waveguide cavity filter using reconfigurable liquid-metal perturbing posts," in *2015 IEEE MTT-S International Microwave Symposium*, May 2015, pp. 1–4.

[38] B. A. Belayev and K. V. Lemberg and A. M. Serzhantov, "An X-band magnetically tunable bandpass filter based on novel waveguide cavity resonator," in *2016 Asia-Pacific Microwave Conference (APMC)*, Dec 2016, pp. 1–4.

[39] D. M. Pozar, *Microwave Engineering Third Edition*, editor, Ed. John Wiley and Sons,Inc, 2005.

[40] E. Botes and P. Meyer, "Tunability of commonly used coupled-line bandpass filter topologies," in *2015 Conference on Microwave Techniques (COMITE)*, April 2015, pp. 1–4.

[41] J.-S. Hong and M. J. Lancaster, *Microstrip Filters for RF/Microwave Applications*. John Wiley and Sons,Inc, 2001.

[42] S. Caspi and J. Adelman, "Design of combline and interdigital filters with tapped-line input," *IEEE Transactions on Microwave Theory and Techniques*, vol. 36, no. 4, pp. 759–763, Apr 1988.

[43] M. Sanchez-Renedo, R. Gomez-Garcia, J. I. Alonso, and C. Briso-Rodriguez, "Tunable Combline Filter With Continuous Control of Center Frequency and Bandwidth," *IEEE Transactions on Microwave Theory and Techniques*, vol. 53, January 2005.

[44] H.-U. Moon, S.-U. Choi, Y.-H. Cho, and S.-W. Yun, "Size-reduced tunable hairpin bandpass filter using aperture coupling with enhanced selectivity and constant bandwidth," in *2008 IEEE MTT-S International Microwave Symposium Digest*, June 2008, pp. 747–750.

[45] K. Y. Chan, S. Fouladi, R. Ramer, and R. R. Mansour, "RF MEMS Switchable Interdigital Bandpass Filter," *IEEE Microwave and Wireless Components Letters*, vol. 22, no. 1, pp. 44–46, Jan 2012.

[46] R. K. Hoffmann, *Handbook of Microwave Integrated Circuits*. Artech House, 1987.

[47] D. Kajfez, "Q factor measurements, analog and digital."

[48] S. Maas, P. Meyer, and P. W. van der Walt, "Measurement of loss mechanisms in microwave coaxial resonator filters," *Proc. 2013 AFRICON*, pp. 1–3, 9-12 September 2014.

[49] Skyworks Solution Inc., *SMV1405-SMV1413 Series: Silicon Abrupt Junction Varactor, Packaged and Bondable Chips*, May 2011, Data Sheet.

[50] J. B. Ness, "A unified approach to the design, measurement, and tuning of coupled-resonator filters," *IEEE Transactions on Microwave Theory and Techniques*, vol. 46, no. 4, pp. 343–351, Apr 1998.

[51] F. S. Su, Y. M. Chen, and S. F. Chang, "Packaged Tunable Combline Bandpass Filters," *IEEE Microwave Magazine for the Microwave and Wireless Engineer*, vol. 16, pp. 93–98, 2015.

[52] O. Buslov, V. Keys, A. B. Kozyrev, A. Y. Shimko, N. M. Alford, and P. K. Petrov, "Band-pass tunable filter based on planar dielectric resonators," *Microwave & Telecommunication Technology, CriMiCo 2008*, pp. 513–514, 8-12 September 2008.

[53] F. Lin and M. Rais-Zadeh, "A Tunable 0.6 GHz - 1.7 GHz Bandpass Filter With a Constant Bandwidth Using Switchable Varactor-Tuned Resonators," *Proc. International Microwave Symposium*, pp. 1–4, 17-22 May 2015.

[54] G. F. Craven and C. K. Mok, "The Design of Evanescent Mode Waveguide Bandpass Filters For a Prescribed Insertion Loss Characteristic," *IEEE Transactrions on Microwave Theory and Techniques*, vol. MTT-19, no. 3, March 1971.

[55] C. A. Balanis, *Advanced Engineering Electromagnetics*. John Wiley and Sons,Inc, 2012.

[56] T. Sickel, P. Meyer, and P. W. van der Walt, "An in situ Tunable Diode Mounting Topology for High-Power X-band Waveguide Switches," *IEEE Transactions on Microwave Theory and Techniques*, vol. 55, no. 2, February 2007.

[57] G. F. Engen and C. A. Hoer, "Thru-Reflect-Line: An Improved Technique for Calibrating the Dual Six-Port Automatic Network Analyzer," *IEEE Transactions on Microwave Theory and Techniques*, vol. 27, no. 12, pp. 987–993, Dec 1979.